MULTI-SCALE TOPOLOGY OPTIMIZATION FOR TRANSIENT HEAT ANALYSIS IN POROUS SOLID MATERIAL CONSIDERING SIZE-DEPENDENT EFFECT

Naruethep Sukulthanasorn

MULTI-SCALE TOPOLOGY OPTIMIZATION FOR TRANSIENT HEAT ANALYSIS IN POROUS SOLID MATERIAL CONSIDERING SIZE-DEPENDENT EFFECT

Naruethep Sukulthanasorn

Supervised by
Prof. Junji Kato

A Dissertation Submitted to Nagoya University
in Partial Fulfillment of the Requirements for
the Degree of Doctor of Engineering

Department of Civil Engineering
Faculty of Engineering, Nagoya University
Nagoya, Japan

2022

Abstract

Topology optimization together with additive manufacturing is now broadly used to design and prototype high-temperature structures. In such a situation, many new challenges are opening up due to their advantages, e.g. free-form design, tailored shapes, and rapid fabrication. This allows for innovative and advanced designs that are complicated but promise high performance. For example, lattice and porous structures have originally good performance to dissipate heat from the structure and this attractive feature is significant in the design procedure.

To tackle these design problems, single-scale design approach may not be efficient for the full capability of this kind of structures. Alternatively, the multi-scale analysis, which includes heat characteristics from the microscopic lattice and porous structures, plays a significant role in the advanced design. In fact, a few studies have investigated multi-scale topology optimization with transient heat conditions.

In the first part, a two-scale topology optimization framework for determining the optimal microstructure in porous material under transient heat conduction and transfer has been developed. The new optimization model, which can consider the surface area directly from microstructure topology as the size-dependent term, is introduced to enhance the heat transfer performance. In more detail, a homogenization method capable of considering the size-dependent microscopic heat transfer effect is adopted to express the microscopic material responses. A well-known material interpolation, referred to as the SIMP approach, and the linear function are used for interpolating intermediate material properties. The minimal transient heat compliance is chosen as an objective function in this optimization problem. For the sensitivity analysis, a coupled-adjoint variable method is adopted to derive transient sensitivity formulation. The analysis shows that the proposed topology optimization model captures not only the transient heat but also the size effect of the microstructure in a transient heat analysis in porous material.

Then, the second part presents the extended framework for the concurrent two-scale topology optimization. Both macro- and microstructures are simultaneously optimized under transient heat conditions for minimization of transient heat compliance. In the numerical results, the optimized macrostructures show good agreement with the benchmark of the relevant works, while the optimized microstructure relates to the design obtained from the first part. In addition, the results also emphasize the

significance of transient and size-dependent effects on both macro-and microstructures, showing a better performance when considering transient and size-dependent effects in the design method of topology optimization.

Regarding the results, the proposed topology optimization framework shows the attractive performance to enhance transient heat dissipation using the size-dependent effect of microstructure in the porous material. Furthermore, as a powerful feature, it is capable to design optimal macro and microstructures together with the multiple design domains that enable extreme performance to be extracted.

Acknowledgements

First, the author would like to express my gratitude and appreciation to the author's supervisor, Professor Junji Kato, for his kind guidance, constructive feedback, and providing a supportive atmosphere to overcome the difficulties along the research journey. This work cannot be completed to the desired outcome without his assistance. Also, the author is thankful to Professor Kenjiro Terada and Associate Professor Mao Kurumatani for their insightful comments on the implementation of the two-scale analysis model. Thankful to Professor Michael Kaliske at TU Dresden, Dr. Koji Nishiguchi, and Dr. Hiroya Hoshiba for the internal review. Their suggestions guide the author to improve the quality of this work.

The author also would like to thank the dissertation committee: Prof. Kazuo Tateishi and Prof. Masatoshi Shimoda, for their time and effort in reviewing the documents. Deepest thanks to the members of the Laboratory who gave a warm welcome and spent time together to conduct the research. Although it is not easy along the way, we also have a lot of good memories together.

Special appreciation to the Japanese government's MEXT scholarship, which offered financial support during the doctoral program at Nagoya University. This assistance allows the author to concentrate on the study.

Last but not least, the author would like to express gratitude to my family for their patience, support, and presence. In addition, the author thanks the Thai friends in Nagoya, who supported and gave me positive energy.

Contents

1 Introduction **1**

1.1 Research background 1

1.2 Topology optimization for heat transfer 2

1.3 Multi-scale topology optimization for heat transfer 3

1.4 Topology optimization for heat transfer with size-dependent effect . . 4

1.5 Research purpose 6

2 The brief review on two-scale transient heat analysis **7**

2.1 Problem statement 7

2.2 Governing equation 9

3 The development of topology optimization framework for designing microstructure **12**

3.1 Optimization framework 12

3.1.1 Material interpolation 12

3.1.2 The proposed scheme for interpolating microscopic heat transfer 13

3.1.3 Macroscopic material parameters 15

3.1.4 Microscopic boundary value problem 15

3.1.5 Setting of optimization problem 17

3.2 Sensitivity analysis 18

3.2.1 Sensitivity of objective function 18

3.2.2 Derivative of homogenized coefficients 22

3.2.3 Verification of analytical sensitivity formulation 23

3.3 Numerical examples 24

3.3.1 Calculation conditions 26

3.3.2 Numerical example 1 27

3.3.3 Numerical example 2 33

3.3.4 Numerical example 3 42

3.4 Summary 50

4 The development of topology optimization framework for designing micro-and macrostructures **51**
4.1 Formulation 51
4.1.1 Definition of two-scale design variables 52
4.1.2 Material interpolation 52
4.1.3 Homogenized material coefficients 53
4.1.4 Objective function 54
4.1.5 Sensitivity analysis 55
4.1.6 Derivative of macro-and micro- material parameters 58
4.2 Numerical Results 59
4.2.1 Example 1: a plate-like structure subject to heat flux at center 60
4.2.2 Example 2: a plate-like structure subject to four heat fluxes . 68
4.3 Summary 73

5 Conclusion **74**

List of Figures

1.1 The application of porous material for heat devices such as heat sink and exchanger from the various works (Bilen et al. 2017; Sertkaya et al. 2018; Feng et al. 2018; Li et al. 2020) 2
1.2 Topology optimization and additive manufacturing for heat devices by Lange et al. 2018 and Subramaniam et al. 2018 5

2.1 Sketch of heat transfer analysis in porous material by the homogenization method 8

3.1 Sketch of material interpolation function for (a) specific heat, material density and heat conduction and (b) heat transfer 13
3.2 The proposed heat transfer model in microstructure for optimization 14
3.3 Periodic boundary condition in a unit cell and three sets of unit vectors 16
3.4 A diagram of optimization scheme adopted in present study 19
3.5 Model for sensitivity verification 24
3.6 Sensitivity of (a) macrostructure A and (b) macrostructure B using the proposed analytical formulation and finite difference method (FDM) 25
3.7 The rectangular macrostructure subjected to three loading conditions with temperature constraint, and its microstructure design 27
3.8 Optimization results under loading case-1 28
3.9 Optimization results under loading case-2 29
3.10 Optimization results under loading case-3 30
3.11 History of objective function value during optimization 31
3.12 History of microstructural volume constraint 32
3.13 Plate-like macrostructure subject to heat flux at center and its microstructure 34
3.14 Optimization results of plate-like structure for the 0.05 s period of time 36
3.15 Optimization results of the plate-like structure for the 0.5 s period of time 37
3.16 History of microstructural volume constraint 38
3.17 Maximum temperature on the plate-like macrostructure for the 0.5 s period of time for the two optimized microstructures 39

3.18 Comparison of objective function values for the case of two optimized microstructures for the 0.05 s and 0.5 s periods of time 39
3.19 Relationship between objective function and (top) heat transfer coefficient, (bottom) size of the microstructure for the 0.05 s period of time 40
3.20 Relationship between the objective function and (top) heat transfer coefficient, (bottom) size of the microstructure for the 0.5 s period of time 41
3.21 A beam-like macrostructure along with boundary condition, and its microstructure design 42
3.22 Optimization results of beam-like structure for the 0.05 s period of time 44
3.23 Optimization results of beam-like structure for the 0.5 s period of time 45
3.24 Maximum temperature on a beam-like macrostructure for the 0.5 s period of time for the two optimized microstructures 46
3.25 Comparison of objective function values for two optimized microstructures for the 0.05 s and 0.5 s periods of time 46
3.26 Three optimized microstructures for the 0.5 s period of time 48
3.27 Three optimized microstructures for the 0.5 s period of time without the heat transfer effect 48
3.28 Comparison of the objective function and the size of the microstructures in cases (i) and (ii) 49

4.1 The interpolation function for heat transfer in the microstructure 53
4.2 The optimization process of proposed concurrent two-scale topology optimization 56
4.3 A plate-like macrostructure under single heat flux and its microstructure . 60
4.4 The optimization results at each target time of plate-like macrostructures under single heat flux 61
4.5 History of objective function values at different target times 62
4.6 History of optimal topologies for macro-and microstructures at $t = 0.5$ s . 63
4.7 History of optimal topologies for macro-and microstructures at $t = 2.0$ s . 64
4.8 The result of optimization with an artificially large microstructure to eliminate the effect of microscopic heat transfer: a symmetric microstructure is obtained 66
4.9 Investigation of microstructure size on optimization results of Figs. 4(d) and (h) 67
4.10 A plate-like macrostructure under four heat fluxes and its microstructure . 68
4.11 The optimization results at each target time of plate-like macrostructures under four heat fluxes 69

4.12 History of objective function values at different target times 70
4.13 History of optimal topologies for macro-and microstructures at $t = 1.0$ s . 71
4.14 History of optimal topologies for macro-and microstructures at $t = 5.0$ s . 71
4.15 The investigation of microscopic volume constraint values of the solid phase 72

List of Tables

3.1 Material properties of fluid (Ω_{I}) and solid phases (Ω_{II}) 25
3.2 Comparison of single and three design microstructures 50

4.1 Material properties 59

Chapter 1

Introduction

1.1 Research background

Porous media have long been applied in the heat management systems in various equipment. Since they are lightweight and have excellent heat transfer qualities, porous media are attractive materials for use in many applications, including heat exchangers, heat sinks, in energy storage and in cooling systems. Their properties have been well-researched over a period extending more than 50 years by Woodside and Messmer 1961, Kaviany 1999, Sopian et al. 1999, Mohamad 2003, Bejan et al. 2004, Clyne et al. 2006, and Singh et al. 2008. For further information, we refer to a comprehensive review of using porous material for heat exchangers and electronic devices by Rashidi et al. 2019, Li et al. 2021, and Jiaqiang et al. 2022, respectively. Some examples of its application are illustrated in Fig.1.1. In the past, the equipment has utilized a simplified layout with roughly approximate material properties in heat management industries. However, over the last decade, an attractive design method, known as topology optimization, has become widely adopted. Topology optimization is a powerful and robust tool for structural design, well-suited for use along with additive manufacturing (AM). New challenges are widely opening up for innovation thanks to such advantages as the flexible design of topology and fabrication in various fields (Khatir et al. 2020; Khatir et al. 2021; Tran-Ngoc et al. 2021). Topology optimization is considered a promising tool with potential to enhance both the performance and appearance of thermal devices made of porous material by fully utilizing its capabilities (Takezawa and Kobashi 2017; Jia et al. 2018; Liu et al. 2018; Das and Sutradhar 2020; Ozguc et al. 2021).

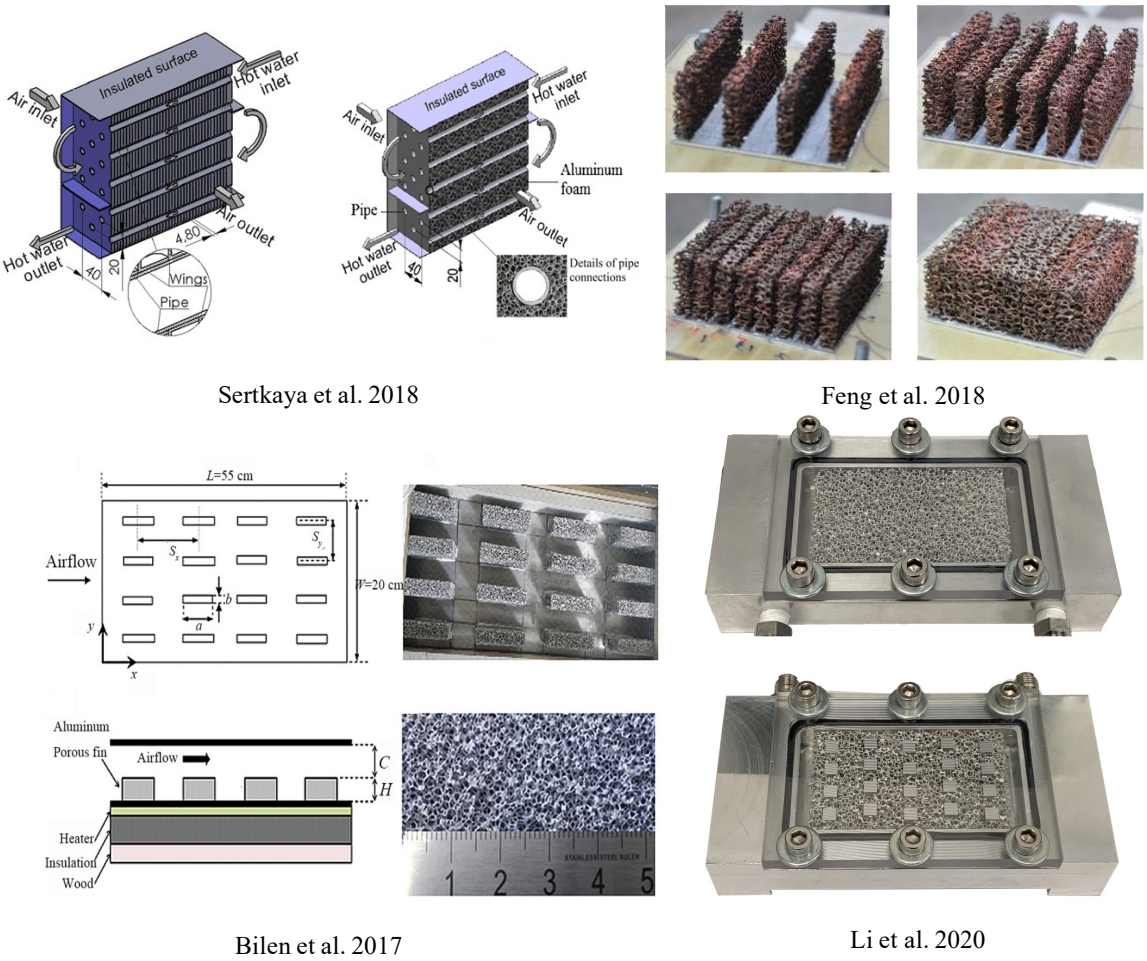

Figure 1.1: The application of porous material for heat devices such as heat sink and exchanger from the various works (Bilen et al. 2017; Sertkaya et al. 2018; Feng et al. 2018; Li et al. 2020)

1.2 Topology optimization for heat transfer

Topology optimization with macroscopic heat analysis problems has been extensively investigated (Gersborg-Hansen et al. 2006; Gao et al. 2008; Li et al. 2004; Zhuang et al. 2007; Dbouk 2017; Lohan et al. 2017; Subramaniam et al. 2018; Fawaz et al. 2022). The focus of most of these studies, however, has been on steady-state problems. In heat transfer problems, it is well-known that the optimal structure strongly depends on the heat-conducting path on the structure (Zhang and Liu 2008; Manuel and Lin 2017; Li et al. 2018). In many real circumstances, the heat-conducting path distributed on the structure is known to be significantly dependent on the function of time. In studies by Zhuang and Xiong (2014, 2015), the adjoint variable method was used in the topology optimization for 2D transient heat transfer to minimize global heat compliance under a temperature constraint. In a study by Long et al. (2018), a multi-material topology optimization framework was introduced employing sequential quadratic programming. Topology

optimization was also adopted to design metadevices under the transient condition of heat flux by Hostos et al. (2019). Their results show a significant performance improvement compared to the steady-state framework. Zhuang et al. (2020) presented topology optimization for transient nonlinear heat conduction problem using level-set method. The dynamic volume constraint and adaptive coefficients of radial basis functions were implemented to update the geometry. Recently, Wu et al. (2019, 2021a) proposed two new objective functions for transient heat conduction: the regional temperature control function (RTCF) and the transient thermal dissipation efficiency (TTDE). The performance of the proposed objective functions is better than that of thermal heat compliance (THC), according to Zhuang and Xiong (2014), due to the different optimal layouts shown at each different time until convergence to steady-state heat conduction. More recently, Hyun and Kim (2021) reported level-set topology optimization along with a thermal eigenvalue analysis for transient heat conduction, and showed that the setting of the target period of time can provide different topologies. These studies confirm the significance of the transient effect and its potential effect on the optimal structure layout of the transient heat problem at the macroscopic level. However, in nature, material is not simply smooth. The heterogeneous nature of materials means that the arrangement and property of the structure at a smaller scale level can significantly control thermal performance. In particular, porous material has a certain surface area that is directly related to its ability to dissipate heat.

1.3 Multi-scale topology optimization for heat transfer

Topology optimization which deals with different scales can be referred to as multi-scale topology optimization. After original works by Suzuki and Kikuchi (1991), Diaaz and and Kikuchi (1992), and Bendsøe and Kikuchi (1998), the homogenization method has been successfully applied to the development of multi-scale topology optimization in a number of studies (Hassani and Hinton 1998; Buehler et al. 2004; Nakshatrala et al. 2013; Sivapuram et al. 2016; Xia and Breitkopf 2017; Fan et al. 2020). In addition, a comprehensive review of multi-scale topology optimization techniques was done by Wu et al. (2021b). The transient heat problem was approached recently by Pizzolato et al. (2019), who proposed a multi-scale topology optimization framework for transient heat conduction using a level-set method at the macroscopic level. At the microstructure level, they proposed a framework for reduction of the geometric complexity and for homogenization to evaluate representative material properties. Recently, Al Ali and Shimoda (2022) investigated a

concurrent multi-scale topology optimization framework for steady-state heat conduction problems with homogenization method. Minimization of heat compliance was chosen to be objective function. Three optimization schemes, i.e., solid isotropic material with penalization, level set, and evolutionary structural optimization, are implemented and compared to study the performance. It reveals that solid isotropic material with penalization performed the best among the others. Here, it should be noted that homogenization can represent a microstructure under certain specific conditions, such as in a periodic unit cell or for the infinitely small ratio of scales between the micro- and macroscopic levels. Therefore, this framework does not typically consider the finite size of the microstructure in the optimization process. However, in practical applications, it is necessary to consider the exact size of the unit cell (Zhang and Sun 2006; Cheng et al. 2018; Cheng et al. 2019; Elkholy and Kempers 2020), especially for fabrication.

1.4 Topology optimization for heat transfer with size-dependent effect

Nowadays, topology optimization and additive manufacturing are widely used to create innovative structures for heat devices (see Fig.1.2, as the examples) due to their efficient design and speedy production advantages. However, since it is necessary to set the specific size for printing the structure, attention has been given to considering the size of the unit cell (Liu and Su 2010; Li and Khandelwal 2015; Gan and Wang 2021; Gan and Wang 2022; Jung et al. 2022; Wang et al. 2022). However, only a few works investigate heat problems. For example, Liu et al. (2021) recently proposed a multi-domain topology optimization for architecture designed structures with the exact size of the unit cell by using the homogenization method. Cheng et al. (2018) presented a variable-density lattice structure topology optimization framework for heat conduction design under the parametric level set functions. In their work, they also conducted the numerical tests to determine the minimum size of lattice structures which can be printed by an additive manufacturing machine. In addition to the manufacturing point of view, the behavior of the material strongly depends on the size of the microstructure, especially for a porous material which has high porosity and a large surface area. These properties are closely related with the heat transfer performance of the material (Lee and Cunnington 2000; Lafdi et al. 2007; Michna et al. 2011; Fugmann et al. 2018). However, from extensive reviews, topology optimization for transient heat transfer in porous material considering the surface area and finite size of the microstructure is still limited and requires further investigation.

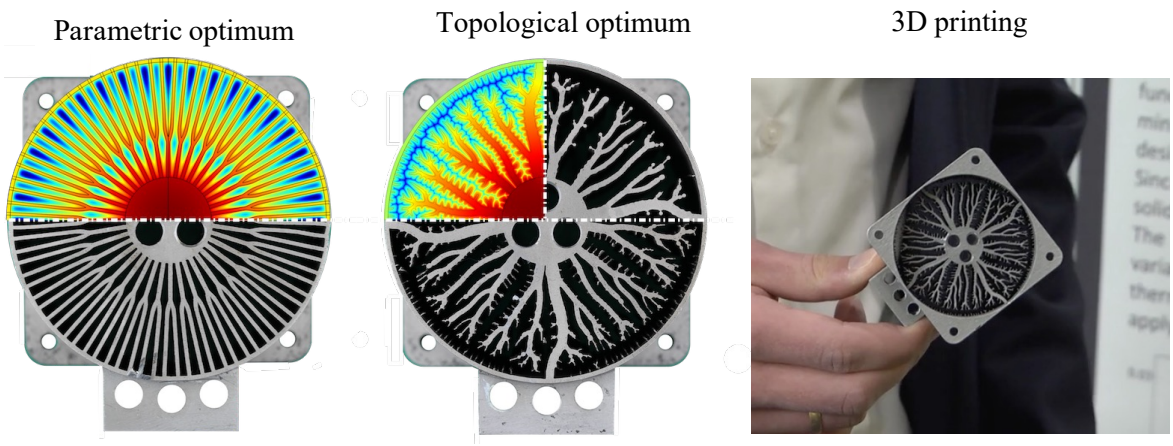

Lange et al. 2018

https://www.comsol.com/blogs/comparing-optimization-methods-for-a-heat-sink-design-for-3d-printing/

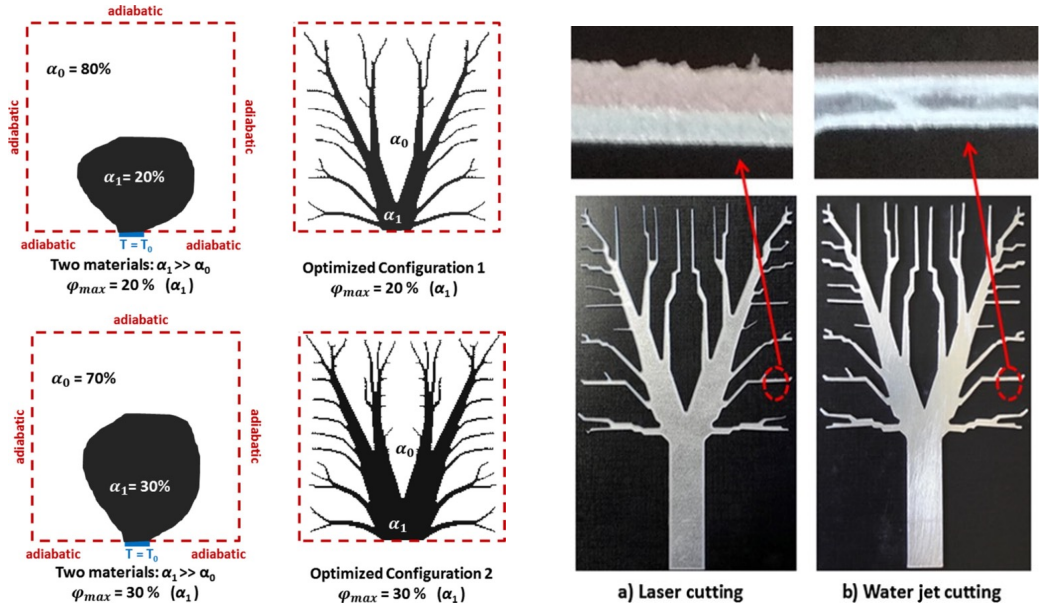

Subramaniam et al. 2018

Figure 1.2: Topology optimization and additive manufacturing for heat devices by Lange et al. 2018 and Subramaniam et al. 2018

1.5 Research purpose

The objective and novelty of the present study is to develop a method considering surface area of porosity in microstructures based on the density-based SIMP approach to reflect a physical thermal behavior between two phases at the micro-level. This concept makes it possible to consider the size effect of microstructures indirectly in an easy way combined with the transient framework.

The study is divided into two parts: firstly, topology optimization for designing microstructure under transient heat analysis subjected to a given macrostructure is developed, and minimizing thermal compliance is established as the objective function along with analytical sensitivity expression. Then, the design framework is extended to be capable of designing both macro-and microstructures. Numerical examples are presented to demonstrate reliability and performance of developed design scheme.

Chapter 2

The brief review on two-scale transient heat analysis

2.1 Problem statement

Consider a three-dimensional porous solid material Ω with a smooth boundary $\partial\Omega$. The boundary conditions are classified into the two types shown in Fig. 2.1: heat flux Q on the Neumann boundary Γ_{Q} and temperature constraint T_0 on the Dirichlet boundary Γ_{T}. At the micro-scale level, porous material consists of periodic microstructures with perfect connectivity. The microstructure itself consists of two materials: one is a high thermal conductivity material (Ω_{I}) and the other is a low thermal conductivity material (Ω_{II}), e.g. solid-void and solid-fluid, respectively. In this study, the following assumptions were made for the distribution of heat in porous material:

- Heat transfer occurs from high to low thermal conductivity materials only.
- The temperature in high thermal conductivity material is higher than that in lower material.
- The macroscopic material parameters of high and low conductivity materials are independently determined by the microstructure of the material following the homogenization theory.
- It is assumed that the boundary conditions (Neumann and Dirichlet) apply to high thermal conductivity material while the adiabatic condition is assumed for low thermal conductivity material.

These concepts were firstly introduced by Terada et al. (2010) to model thermal behavior in porous media with fluid and solid phases. The framework is mathematically developed using a two-scale asymptotic expansion and shows good computational

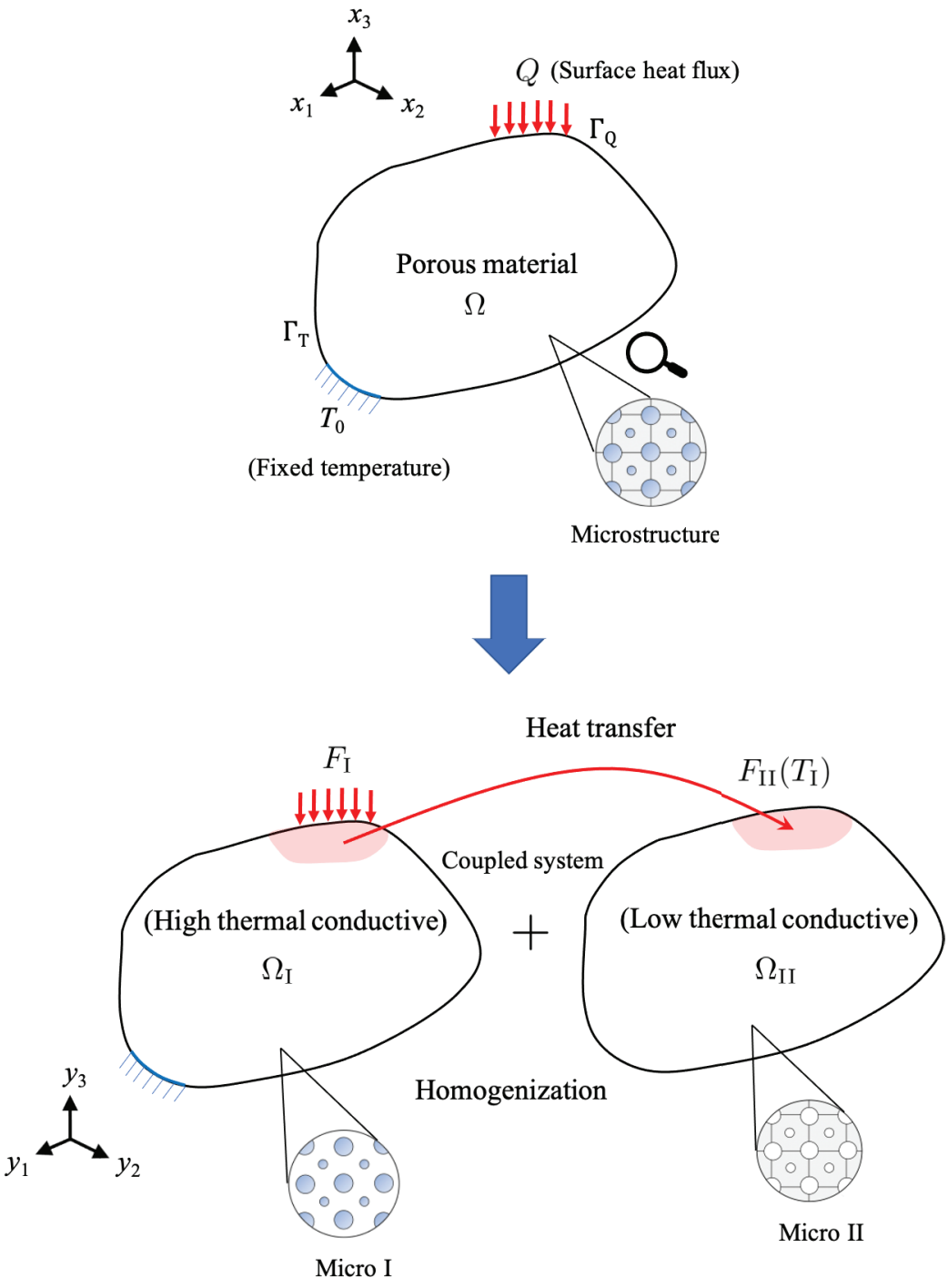

Figure 2.1: Sketch of heat transfer analysis in porous material by the homogenization method

performance and accuracy compared with the benchmark. It should be noted that, although this proposed method lies on some assumptions, it is still applicable in practice, especially when the different temperature of two phases is the large value. For instance, in the case of the solid porous material subjected to high thermal conditions and thus the temperature on solid medium mainly dissipates to the air through the interface of pores.

Regarding the attractive advantages, the present study follows their concept and framework, however, we replace the words "fluid and solid phases" with more general expression "high (Ω_{I}) and low thermal (Ω_{II}) conductivity materials" for flexibility of the proposed framework.

To avoid confusion, we define the heat conduction and heat transfer used in this study as the heat distribution at macro-and micro-scale, respectively.

2.2 Governing equation

According to Terada et al. (2010), the heat transfer parameter relates to material Ω_{II} only. However, in fact, this parameter affects the temperature distribution in both materials Ω_{I} and Ω_{II} (Kaviany 1999; Forooghi et al. 2011; Ouyang et al. 2013). Therefore, to enhance the model without loss of the advantages of computational performance from the original work, the heat transfer term is directly added to the governing equation of the material Ω_{I} while the rest of the governing equation remains unchanged. The two-scale transient governing equation for heat conduction and transfer in porous material can be expressed as follows:

$$C^{\mathrm{H}}\dot{T}(\boldsymbol{x},t) + \nabla \cdot \boldsymbol{q}(\boldsymbol{x},t) + \Psi(\boldsymbol{x},t) = 0 \quad \text{in } \Omega \tag{2.1}$$

with

$$\boldsymbol{q}(\boldsymbol{x},t) = -\boldsymbol{k}_{\mathrm{c}}^{\mathrm{H}} \nabla T(\boldsymbol{x},t) \quad \text{in } \Omega, \tag{2.2}$$

$$\Psi(\boldsymbol{x},t) = \begin{cases} k_{\mathrm{t}}^{\mathrm{H}} T_{\mathrm{I}}(\boldsymbol{x},t) & \text{if } \boldsymbol{x} \in \Omega_{\mathrm{I}} \\ k_{\mathrm{t}}^{\mathrm{H}} \left(T_{\mathrm{II}}(\boldsymbol{x},t) - T_{\mathrm{I}}(\boldsymbol{x},t) \right) & \text{if } \boldsymbol{x} \in \Omega_{\mathrm{II}} \end{cases}. \tag{2.3}$$

Also, the following boundary conditions are imposed:

$$T(\boldsymbol{x},t) = T_0 \quad \text{on } \Gamma_{\mathrm{T}}, \tag{2.4}$$

$$\boldsymbol{q}(\boldsymbol{x},t) \cdot \boldsymbol{n} = Q \quad \text{on } \Gamma_{\mathrm{Q}}, \tag{2.5}$$

and the initial condition:

$$T(\boldsymbol{x}, 0) = T_0 \quad \text{in } \Omega, \tag{2.6}$$

where $T(\boldsymbol{x}, t)$ is the temperature field defined in domain Ω and depends on the position $\boldsymbol{x}$ in macro-scale and time t. $\dot{T}(\boldsymbol{x}, t)$ stands for the time derivative of the temperature field. ∇ refers to the gradient operator, and $\boldsymbol{n}$ is the outward unit normal vector. C^{H}, $\boldsymbol{k}_{\mathrm{c}}^{\mathrm{H}}$ and $k_{\mathrm{t}}^{\mathrm{H}}$ are macroscopic coefficients of the heat capacity, heat conduction and heat transfer, respectively. These macroscopic material parameters are computed from the homogenization analysis and are commonly known as homogenized coefficients. The weak formulation is expressed as

$$\begin{aligned}\int_{\Gamma_{\mathrm{Q}}} \delta T(\boldsymbol{x}) Q \, \mathrm{d}\Gamma = \int_{\Omega} \delta T(\boldsymbol{x}) C^{\mathrm{H}} \dot{T}(\boldsymbol{x}, t) \, \mathrm{d}\Omega + \int_{\Omega} \nabla \delta T(\boldsymbol{x}) \boldsymbol{k}_{\mathrm{c}}^{\mathrm{H}} \nabla T(\boldsymbol{x}, t) \, \mathrm{d}\Omega \\ + \int_{\Omega} \delta T(\boldsymbol{x}) \Psi(\boldsymbol{x}, t) \, \mathrm{d}\Omega,\end{aligned} \tag{2.7}$$

where $\delta T(\boldsymbol{x})$ is the virtual temperature field. To solve for $T(\boldsymbol{x}, t)$, Eq. (2.7) is discretized following the Galerkin finite element method. Finally, the one-way coupling equation system can be established as follows

$$\boldsymbol{C}_{\mathrm{I}} \dot{\boldsymbol{T}}_{\mathrm{I}} + \boldsymbol{K}_{\mathrm{I}} \boldsymbol{T}_{\mathrm{I}} = \boldsymbol{F}_{\mathrm{I}}, \tag{2.8}$$

$$\boldsymbol{C}_{\mathrm{II}} \dot{\boldsymbol{T}}_{\mathrm{II}} + \boldsymbol{K}_{\mathrm{II}} \boldsymbol{T}_{\mathrm{II}} = \boldsymbol{F}_{\mathrm{II}}(\boldsymbol{T}_{\mathrm{I}}), \tag{2.9}$$

where $\boldsymbol{T}_{\mathrm{I}}$ and $\boldsymbol{T}_{\mathrm{II}}$ are the global nodal temperature vectors of materials Ω_{I} and Ω_{II}, respectively. The expressions of $\boldsymbol{C}_{\mathrm{I}}, \boldsymbol{C}_{\mathrm{II}}, \boldsymbol{K}_{\mathrm{I}}$ and $\boldsymbol{K}_{\mathrm{II}}$, and global force vectors $\boldsymbol{F}_{\mathrm{I}}$ and $\boldsymbol{F}_{\mathrm{II}}$, can be written as follows:

$$\boldsymbol{C}_{\mathrm{I}} = \int_{\Omega_{\mathrm{I}}} \boldsymbol{N}^{\mathrm{T}} C_{\mathrm{I}}^{\mathrm{H}} \boldsymbol{N} \, \mathrm{d}\Omega, \tag{2.10}$$

$$\boldsymbol{C}_{\mathrm{II}} = \int_{\Omega_{\mathrm{II}}} \boldsymbol{N}^{\mathrm{T}} C_{\mathrm{II}}^{\mathrm{H}} \boldsymbol{N} \, \mathrm{d}\Omega, \tag{2.11}$$

$$\boldsymbol{K}_{\mathrm{I}} = \int_{\Omega_{\mathrm{I}}} \boldsymbol{B}^{\mathrm{T}} \boldsymbol{k}_{\mathrm{c}}^{\mathrm{H}} \boldsymbol{B} \, \mathrm{d}\Omega + \int_{\Omega_{\mathrm{I}}} \boldsymbol{N}^{\mathrm{T}} k_{\mathrm{t}}^{\mathrm{H}} \boldsymbol{N} \, \mathrm{d}\Omega, \tag{2.12}$$

$$\boldsymbol{K}_{\mathrm{II}} = \int_{\Omega_{\mathrm{II}}} \boldsymbol{B}^{\mathrm{T}} \boldsymbol{k}_{\mathrm{c}}^{\mathrm{H}} \boldsymbol{B} \, \mathrm{d}\Omega + \int_{\Omega_{\mathrm{II}}} \boldsymbol{N}^{\mathrm{T}} k_{\mathrm{t}}^{\mathrm{H}} \boldsymbol{N} \, \mathrm{d}\Omega, \tag{2.13}$$

$$\boldsymbol{F}_{\mathrm{I}} = \int_{\Gamma_{\mathrm{Q}}} \boldsymbol{N}^{\mathrm{T}} Q \, \mathrm{d}\Gamma, \tag{2.14}$$

$$\boldsymbol{F}_{\mathrm{II}} = \int_{\Omega_{\mathrm{I}}} \boldsymbol{N}^{\mathrm{T}} k_{\mathrm{t}}^{\mathrm{H}} \hat{T}_{\mathrm{I}} \, \mathrm{d}\Omega, \tag{2.15}$$

where $\hat{T}_{\mathrm{I}} = \boldsymbol{N}\boldsymbol{T}_{\mathrm{I}}$ and $\boldsymbol{N}$ is the standard shape function together with its derivative matrix $\boldsymbol{B}$. In addition, the temporal discretization technique, called the Crank-Nicolson method, is adopted in this study to solve the time evolution in Eqs. (2.8) and (2.9). Furthermore, to deal with transient analysis, Crank-Nicloson method is adopted for obtaining $\dot{\boldsymbol{T}}$, $\boldsymbol{T}$ and $\boldsymbol{F}$ from the time t_i to t_{i+1} as

$$\dot{\boldsymbol{T}} = \frac{\boldsymbol{T}_{i+1} - \boldsymbol{T}_i}{\triangle t}, \tag{2.16}$$

$$\boldsymbol{T} = \frac{\boldsymbol{T}_{i+1} + \boldsymbol{T}_i}{2\triangle t}, \tag{2.17}$$

$$\boldsymbol{F} = \frac{\boldsymbol{F}_{i+1} + \boldsymbol{F}_i}{2\triangle t}, \tag{2.18}$$

where $\triangle t$ denotes the time step size, $()_{i+1}$ and $()_i$ are the current and previous time steps, respectively. Thus, Eqs.(2.8) and (2.9) can be similarly expressed in the time discretization form as

$$(\frac{1}{\triangle t}\boldsymbol{C} + \frac{1}{2}\boldsymbol{K})\boldsymbol{T}_{i+1} = \frac{1}{2}(\boldsymbol{F}_{i+1} + \boldsymbol{F}_i) + (\frac{1}{\triangle t}\boldsymbol{C} - \frac{1}{2}\boldsymbol{K})\boldsymbol{T}_i. \tag{2.19}$$

Chapter 3

The development of topology optimization framework for designing microstructure

In this chapter, the topology optimization framework for designing microstructure under transient heat transfer is developed based on the analysis model presented in the previous chapter. The objective function and analytical sensitivity expression are presented to achieve the optimal design. Finally, the numerical results are selected to demonstrate the reliability and robustness of the developed design framework.

3.1 Optimization framework

In this section, the design variable and the concept of material interpolation are introduced to deal with the intermediate value during the optimization process. Then, the expression of each macroscopic material parameter is addressed following the homogenization method. Finally, the objective function and constraint are introduced to define the optimization problem.

3.1.1 Material interpolation

Firstly, the microscopic design variable s_i is defined as a volume fraction of a high thermal conductivity material Ω_{I} in a finite element of a unit cell and is assumed to be continuous in $0 \leq s_i \leq 1$. Hence, it represents the high thermal conductivity material Ω_{I} when $s_i = 1$ and the low thermal conductivity material Ω_{II} when $s_i = 0$. The intermediate value represents the mixture of the two materials, which is an artificial material.

Then, the density-based concept, namely SIMP—Solid Isotropic Material with Penalization (Bensøe and Sigmund 2003), is applied to interpolate material proper-

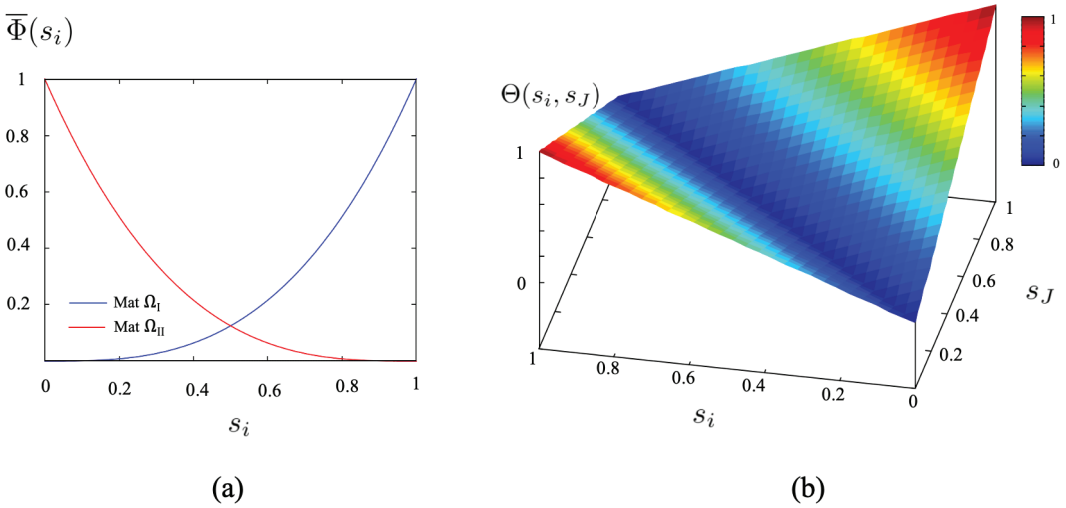

Figure 3.1: Sketch of material interpolation function for (a) specific heat, material density and heat conduction and (b) heat transfer

ties for specific heat c, material density ρ and heat conduction k_c. The formulation can be described based on the power-law as

$$\overline{\Phi} = \begin{cases} \Phi_{\min} + s_i^{\eta}\ \Phi_{\rm I} & \text{for } \Omega_{\rm I} \\ \Phi_{\min} + (1 - s_i)^{\eta}\ \Phi_{\rm II} & \text{for } \Omega_{\rm II} \end{cases}, \tag{3.1}$$

where $\overline{\Phi}$ represents the effective material parameter for specific heat $\overline{c}$, material density $\overline{\rho}$ and heat conduction $\overline{k}_{\rm c}$ as shown in Fig. 3.1(a). $\Phi_{\min}$ is the minimum value of the effective material parameter to avoid singularity during optimization, $\Phi_{\rm I}$ and $\Phi_{\rm II}$ are the material properties of the high thermal conductivity material $\Omega_{\rm I}$ and the low thermal conductivity one $\Omega_{\rm II}$, respectively. η denotes the power factor and $\eta = 3$ is selected in this study. Note that the effective material parameters shown in Eq. (3.1) are separately computed for materials $\Omega_{\rm I}$ and $\Omega_{\rm II}$ which are individually used for homogenization and then for calculating the macroscopic material parameters in Eqs. (2.8) and (2.9).

3.1.2 The proposed scheme for interpolating microscopic heat transfer

Unlike the previous interpolation concept for specific heat c, material density ρ and heat conduction k_c in Eq. (3.1), microscopic heat transfer occurs at the surface between two materials in the microstructure. Thus, with the finite element method, interpolation of the element face connected with other element faces is required for the intermediate value of the design variables. To deal with this, we adopt the

concept of the difference of adjacent design variables to interpolate the effective heat transfer parameter from the surface area of each corresponding element in the microstructure. This concept is inspired by the interpolation scheme for the heat convection term in Bruns (2007). However, in the present study, it is adopted for evaluating the heat transfer parameter from each interface (surface area) in the microstructure. Finally, it can be formulated in the following form:

$$\overline{k}_{\mathrm{t}} = \Theta(s_i, s_J)\ k_{\mathrm{t}}, \tag{3.2}$$

$$\text{with} \quad \Theta(s_i, s_J) = |s_i - s_J|, \tag{3.3}$$

where s_i is the design variable of the considered element, and s_J stands for the design variable of the adjacent element. k_{t} denotes the heat transfer coefficient, and $\overline{k}_{\mathrm{t}}$ is the coefficient of effective heat transfer for each of the surfaces between the materials Ω_{I} and Ω_{II} in the microstructure. As shown in Eqs. (3.2) and (3.3), $\overline{k}_{\mathrm{t}}$ depends on the relative difference function of the design variable $\Theta(s_i, s_J)$ in each neighboring element of the microstructure as demonstrated in Figs. 3.1(b) and 3.2. This means that it is valid if $\Theta(s_i, s_J) \neq 0$. Note here that linear interpolation is

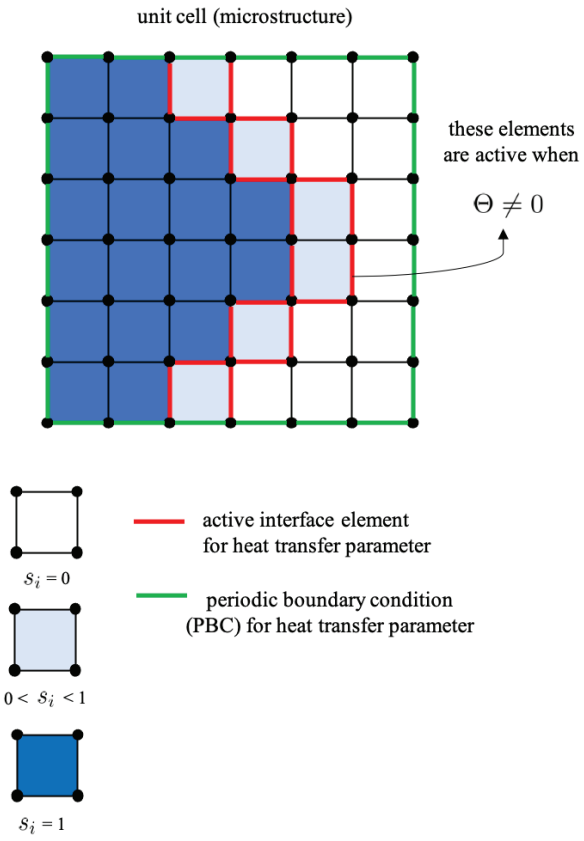

Figure 3.2: The proposed heat transfer model in microstructure for optimization

chosen for the function $\Theta(s_i, s_J)$, based on the result of our preliminary investigation that the penalization underestimates the heat transfer effect significantly.

3.1.3 Macroscopic material parameters

In homogenization theory, the size of the microstructure is assumed to be infinitesimally small (Hassani and Hinton 1998; Terada et al. 2000; Bensoussan et al. 2011): this assumption makes it difficult to consider the size dependency of microstructure on the macroscopic response for realistic design applications. In our proposed framework, however, the homogenization method incorporated with the size-dependent term is addressed to represent the behavior of heat transfer in a porous material. These formulations have been mathematically derived in Terada et al. (2010). Firstly, we denote micro-scale parameters of the unit cell (microstructure) domain, its boundary and spatial position by Y, ∂Y and $\boldsymbol{y}$, respectively. Then, homogenized heat capacity C^{H} and heat conduction $\boldsymbol{k}_{\mathrm{c}}^{\mathrm{H}}$ coefficients can be expressed as

$$C^{\mathrm{H}} = \frac{1}{|Y|} \int_Y \overline{c}\, \overline{\rho}\, \mathrm{d}y, \tag{3.4}$$

$$\boldsymbol{k}_{\mathrm{c}}^{\mathrm{H}} = \frac{1}{|Y|} \int_Y \overline{k}_{\mathrm{c}} (\boldsymbol{I} - \nabla \boldsymbol{\xi})\, \mathrm{d}y, \tag{3.5}$$

where $|Y|$ is the volume of a unit cell. $\boldsymbol{I}$ is the identity matrix, and $\boldsymbol{\xi}$ is the characteristic functions $\{\xi^1, \xi^2, \xi^3\}$ obtained by solving the microscopic boundary value problem presented in the next section.

For the size-dependent term, the homogenized heat transfer coefficient $k_{\mathrm{t}}^{\mathrm{H}}$ is expressed by the surface integral as

$$k_{\mathrm{t}}^{\mathrm{H}} = \frac{1}{|Y|} \int_{\partial Y} \overline{k}_{\mathrm{t}}\, \mathrm{d}S. \tag{3.6}$$

Here, it should be noted that Eq. (3.6) expresses $k_{\mathrm{t}}^{\mathrm{H}}$ in terms of $\overline{k}_{\mathrm{t}}$ and the ratio of total surface area to the volume of the microstructure ($S/|Y|$). Changing the size of the microstructure has a direct effect on this ratio, which is different from the volume average formulations presented in Eqs. (3.4) and (3.5).

3.1.4 Microscopic boundary value problem

In order to determine the homogenized heat conduction coefficient in Eq. (3.5), all the characteristic functions $\{\xi^1, \xi^2, \xi^3\}$ must be obtained. Following the homogenization method, each of the characteristic functions represents the response to one

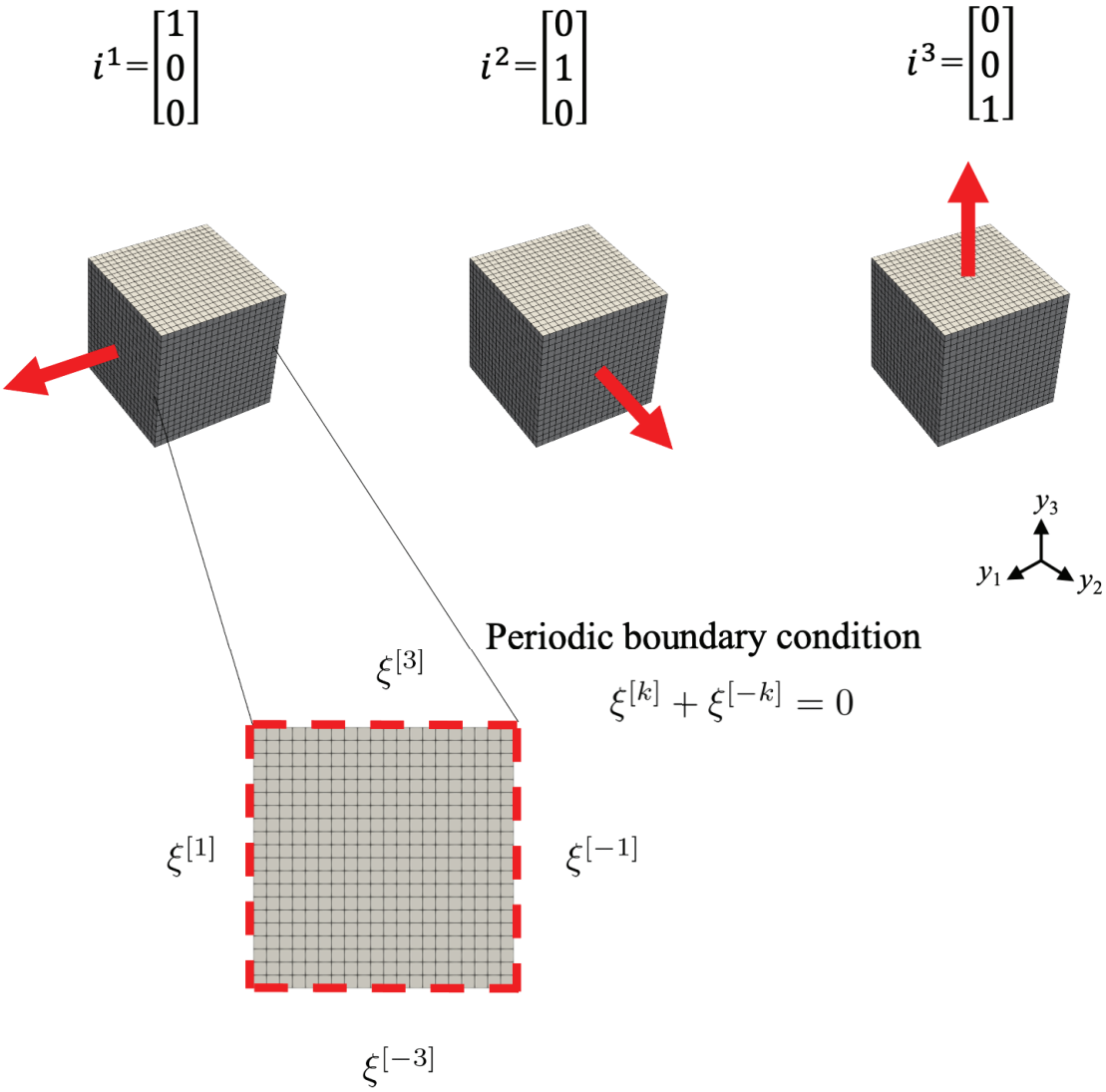

Figure 3.3: Periodic boundary condition in a unit cell and three sets of unit vectors

of the three components of the macroscopic temperature gradient as

$$T^{(\mathrm{mi})} = -\xi^j \frac{\partial T^{(\mathrm{ma})}}{\partial x_j} \quad \text{for} \quad j = 1, 2, 3, \tag{3.7}$$

where $T^{(\mathrm{mi})}$ and $T^{(\mathrm{ma})}$ are the micro-scale and macro-scale temperature fields, respectively. The reader may refer to Terada et al. (2010) and Kato et al. (2018) for further details. As a result, the equations for obtaining the characteristic functions can be expressed as follows:

$$\boldsymbol{H}\boldsymbol{\xi}^j = \boldsymbol{W}, \tag{3.8}$$

$$\boldsymbol{H} = \int_Y \boldsymbol{B}^{\mathrm{T}} \overline{k}_{\mathrm{c}} \boldsymbol{B} \, \mathrm{d}y, \tag{3.9}$$

$$\boldsymbol{W} = \int_{\partial Y} \boldsymbol{B}^{\mathrm{T}} \overline{k}_{\mathrm{c}} \boldsymbol{i}^{j} \, \mathrm{d}y, \tag{3.10}$$

where $\boldsymbol{i}^{j}$ represents the three sets of unit vectors ($j = 1, 2, 3$) corresponding to the macroscopic temperature gradient whose j-th component equals 1 while the remaining components are zero.

In addition, the periodic boundary condition is imposed to microscopic fields on the boundary ∂Y in Eqs. (3.2) and (3.8) for the interpolation function Θ and the characteristic function ξ, respectively. These can be written as

$$\Theta^{[k]} + \Theta^{[-k]} = 0 \quad \text{on } \partial Y, \tag{3.11}$$

$$\xi^{[k]} + \xi^{[-k]} = 0 \quad \text{on } \partial Y, \tag{3.12}$$

where $[\pm k]$ represent the boundary surface positions, with the normal vectors ($k = 1, 2, 3$) parallel to the coordinate axis in the $(+)$ same or $(-)$ opposite directions as shown in Fig.3.3.

3.1.5 Setting of optimization problem

To efficiently control the heat dissipation in a porous material, we aim to design an optimal microstructure which minimizes the remaining heat energy in the considered porous structure. To achieve this, heat compliance is chosen as an objective function. This type of objective function is usually formulated with the inner product of force vector and temperature field of the structure. Similarly, the heat compliance from two materials inside the porous material is considered to represent the heat dissipative performance of the structure; here, the force vector for the high thermal conductivity material Ω_{I} is the external heat flux applied at the boundary of the structure, while the force vector for the low thermal conductivity material Ω_{II} is the heat load which is transferred from the high thermal conductivity material Ω_{I} as an internal heat source.

As a transient problem, the time integration of heat compliance is established for the minimization problem along with the inequality volume constraint and boundary conditions as

$$\begin{aligned}
&\min \quad f(\boldsymbol{s}, t) = \int_0^t \boldsymbol{F}_{\mathrm{I}}^{\mathrm{T}} \boldsymbol{T}_{\mathrm{I}} \, \mathrm{d}t + \int_0^t \boldsymbol{F}_{\mathrm{II}}^{\mathrm{T}} \boldsymbol{T}_{\mathrm{II}} \, \mathrm{d}t, \\
&\text{s.t.} \quad g(\boldsymbol{s}) = \sum_{e=1}^{n_{\mathrm{ele}}} V_e(\boldsymbol{s}) - V_{\max} \leq 0, \\
&T(\boldsymbol{x}, 0) = \dot{T}(\boldsymbol{x}, 0) = T_0,
\end{aligned} \tag{3.13}$$

where $f(\boldsymbol{s}, t)$ stands for the transient objective function, which consists of high and low thermal conductive heat compliances, $g(\boldsymbol{s})$ is the inequality constraint for material volume of microstructure and n_{ele} is the total number of elements in the microstructure. $V_e(\boldsymbol{s})$ refers to the elemental volume of the material Ω_{I}, and $V_{\max}$ is the maximum volume of allowable material Ω_{I} in the microstructure.

In addition, the method of moving asymptotes (MMA) by Svanberg (1987) is adopted in this study to solve the optimization problem along with the analytical sensitivity formulation. As is generally known, MMA is an optimizer that uses gradients to solve a convex subproblem iteratively as part of a global optimization problem. We refer to the original paper for more detail, along with the open source code which is easily accessible in a number of programming languages. The flow of the proposed optimization process is illustrated in Fig. 3.4.

3.2 Sensitivity analysis

In this section, the formulation for analytical transient sensitivity is presented based on the transient adjoint variable method (Tortorelli and Haber 1989; Yoon et al. 2020; Wu et al. 2021a; Yoon 2022) together with the analytical expressions of the derivatives of the homogenized coefficients. Then, the result from the derived sensitivity is compared with that of the finite difference method (FDM) for the purpose of accuracy verification.

3.2.1 Sensitivity of objective function

In this study, we adopt two adjoint variables $\boldsymbol{\lambda}$ and $\boldsymbol{\gamma}$ for the low and high thermal conductivity materials, respectively. Firstly, we provide the following alternative form of objective function:

$$\tilde{f} = f - \underbrace{\int_0^t \boldsymbol{\gamma}^{\mathrm{T}}(\boldsymbol{C}_{\text{I}}\dot{\boldsymbol{T}}_{\text{I}} + \boldsymbol{K}_{\text{I}}\boldsymbol{T}_{\text{I}} - \boldsymbol{F}_{\text{I}})\,\mathrm{d}t}_{R_{\text{I}}}$$

$$- \underbrace{\int_0^t \boldsymbol{\lambda}^{\mathrm{T}}(\mathbf{C}_{\text{II}}\dot{\boldsymbol{T}}_{\text{II}} + \boldsymbol{K}_{\text{II}}\boldsymbol{T}_{\text{II}} - \boldsymbol{F}_{\text{II}})\,\mathrm{d}t}_{R_{\text{II}}}. \tag{3.14}$$

Note that this alternative form $\tilde{f}$ is identical to the original objective function if Eqs. (2.8) and (2.9) are satisfied. For the sake of brevity, we define R_{I} and R_{II} as the second and third terms on the right-hand side of Eq. (3.14). Then, taking the

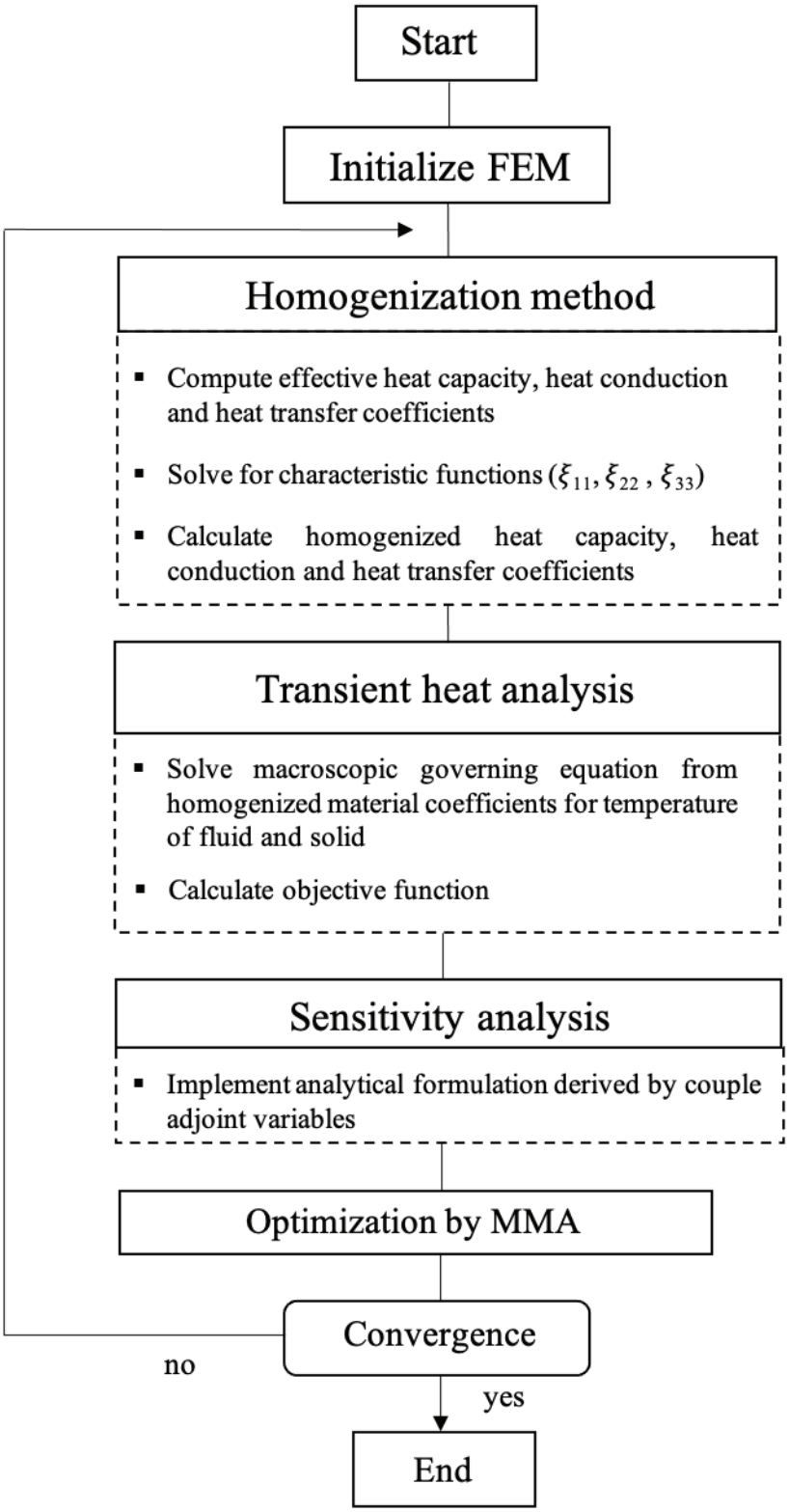

Figure 3.4: A diagram of optimization scheme adopted in present study

derivative with respect to the design variable yields

$$\frac{\partial \tilde{f}}{\partial s_i} = \frac{\partial f}{\partial s_i} - \frac{\partial R_{\mathrm{I}}}{\partial s_i} - \frac{\partial R_{\mathrm{II}}}{\partial s_i}. \tag{3.15}$$

The derivative of the original objective function, the first term on the right-hand side, can be written as

$$\frac{\partial f}{\partial s_i} = \int_0^t \boldsymbol{F}_{\mathrm{I}}^{\mathrm{T}} \frac{\partial \boldsymbol{T}_{\mathrm{I}}}{\partial s_i} \, \mathrm{d}t + \int_0^t (\boldsymbol{F}_{\mathrm{II}}^{\mathrm{T}} \frac{\partial \boldsymbol{T}_{\mathrm{II}}}{\partial s_i} + \frac{\partial \boldsymbol{F}_{\mathrm{II}}^{\mathrm{T}}}{\partial s_i} \boldsymbol{T}_{\mathrm{II}}) \, \mathrm{d}t. \tag{3.16}$$

It is worth noting that $\boldsymbol{F}_{\mathrm{I}}$ is the external heat flux which is independent of the design variable, hence $\partial \boldsymbol{F}_{\mathrm{I}}/\partial s_i$ is zero. On the contrary, $\boldsymbol{F}_{\mathrm{II}}$ depends on the heat transfer from the material Ω_{I} as described in Eq. (2.15). As a result, the implicit term $\partial \boldsymbol{F}_{\mathrm{II}}/\partial s_i$ appears in the last term of Eq. (3.16). Then, $\partial R_{\mathrm{II}}/\partial s_i$ in Eq. (3.15) can be expressed as

$$\begin{aligned} -\frac{\partial R_{\mathrm{II}}}{\partial s_i} = &- \int_0^t (\boldsymbol{\lambda}^{\mathrm{T}} \frac{\partial \mathbf{C}_{\mathrm{II}}}{\partial s_i} \dot{\boldsymbol{T}}_{\mathrm{II}} + \boldsymbol{\lambda}^{\mathrm{T}} \boldsymbol{C}_{\mathrm{II}} \frac{\partial \dot{\boldsymbol{T}}_{\mathrm{II}}}{\partial s_i}) \, \mathrm{d}t \\ &- \int_0^t (\boldsymbol{\lambda}^{\mathrm{T}} \frac{\partial \boldsymbol{K}_{\mathrm{II}}}{\partial s_i} \boldsymbol{T}_{\mathrm{II}} + \boldsymbol{\lambda}^{\mathrm{T}} \boldsymbol{K}_{\mathrm{II}} \frac{\partial \boldsymbol{T}_{\mathrm{II}}}{\partial s_i}) \, \mathrm{d}t + \int_0^t \boldsymbol{\lambda}^{\mathrm{T}} \frac{\partial \boldsymbol{F}_{\mathrm{II}}}{\partial s_i} \, \mathrm{d}t. \end{aligned} \tag{3.17}$$

Here, to eliminate $\dot{\boldsymbol{T}}_{\mathrm{II}}$, we adopt the following operation:

$$-\int_0^t \boldsymbol{\lambda}^{\mathrm{T}} \boldsymbol{C}_{\mathrm{II}} \frac{\partial \dot{\boldsymbol{T}}_{\mathrm{II}}}{\partial s_i} \, \mathrm{d}t = -\left[\boldsymbol{\lambda}^{\mathrm{T}} \boldsymbol{C}_{\mathrm{II}} \frac{\partial \boldsymbol{T}_{\mathrm{II}}}{\partial s_i} \right]_0^t + \int_0^t \dot{\boldsymbol{\lambda}}^{\mathrm{T}} \boldsymbol{C}_{\mathrm{II}} \frac{\partial \boldsymbol{T}_{\mathrm{II}}}{\partial s_i} \, \mathrm{d}t. \tag{3.18}$$

Substituting Eq. (3.18) into Eq. (3.17) along with boundary condition $\partial T_{\mathrm{II}}(\boldsymbol{x}, 0)/\partial s_i = 0$ yields

$$\begin{aligned} -\frac{\partial R_{\mathrm{II}}}{\partial s_i} = &\int_0^t (\dot{\boldsymbol{\lambda}}^{\mathrm{T}} \boldsymbol{C}_{\mathrm{II}} - \boldsymbol{\lambda}^{\mathrm{T}} \boldsymbol{K}_{\mathrm{II}}) \frac{\partial \boldsymbol{T}_{\mathrm{II}}}{\partial s_i} \, \mathrm{d}t + \int_0^t -\boldsymbol{\lambda}^{\mathrm{T}} \left(\frac{\partial \boldsymbol{C}_{\mathrm{II}}}{\partial s_i} \dot{\boldsymbol{T}}_{\mathrm{II}} + \frac{\partial \boldsymbol{K}_{\mathrm{II}}}{\partial s_i} \boldsymbol{T}_{\mathrm{II}} \right) \, \mathrm{d}t \\ &- \boldsymbol{\lambda}^{\mathrm{T}} \boldsymbol{C}_{\mathrm{II}} \left. \frac{\partial \boldsymbol{T}_{\mathrm{II}}}{\partial s_i} \right|_{t=t_{\mathrm{f}}} + \int_0^t \boldsymbol{\lambda}^{\mathrm{T}} \frac{\partial \boldsymbol{F}_{\mathrm{II}}}{\partial s_i} \, \mathrm{d}t. \end{aligned} \tag{3.19}$$

Similarly, we can derive $\partial R_{\mathrm{I}}/\partial s_i$ using the operation defined in Eq. (3.18) and the boundary condition $\partial T_{\mathrm{I}}(\boldsymbol{x}, 0)/\partial s_i = 0$, so that

$$\begin{aligned} -\frac{\partial R_{\mathrm{I}}}{\partial s_i} = &\int_0^t (\dot{\boldsymbol{\gamma}}^{\mathrm{T}} \boldsymbol{C}_{\mathrm{I}} - \boldsymbol{\gamma}^{\mathrm{T}} \boldsymbol{K}_{\mathrm{I}}) \frac{\partial \boldsymbol{T}_{\mathrm{I}}}{\partial s_i} \, \mathrm{d}t + \int_0^t -\boldsymbol{\gamma}^{\mathrm{T}} \left(\frac{\partial \boldsymbol{C}_{\mathrm{I}}}{\partial s_i} \dot{\boldsymbol{T}}_{\mathrm{I}} + \frac{\partial \boldsymbol{K}_{\mathrm{I}}}{\partial s_i} \boldsymbol{T}_{\mathrm{I}} \right) \, \mathrm{d}t \\ &- \boldsymbol{\gamma}^{\mathrm{T}} \boldsymbol{C}_{\mathrm{I}} \left. \frac{\partial \boldsymbol{T}_{\mathrm{I}}}{\partial s_i} \right|_{t=t_{\mathrm{f}}}. \end{aligned} \tag{3.20}$$

Substituting Eqs. (3.16), (3.19) and (3.20) into Eq. (3.15) as

$$\begin{aligned}\frac{\partial \tilde{f}}{\partial s_i} &= \int_0^t \boldsymbol{F}_{\mathrm{I}}^{\mathrm{T}} \frac{\partial \boldsymbol{T}_{\mathrm{I}}}{\partial s_i}\,\mathrm{d}t + \int_0^t (\boldsymbol{F}_{\mathrm{II}}^{\mathrm{T}} \frac{\partial \boldsymbol{T}_{\mathrm{II}}}{\partial s_i} + \frac{\partial \boldsymbol{F}_{\mathrm{II}}^{\mathrm{T}}}{\partial s_i}\boldsymbol{T}_{\mathrm{II}})\,\mathrm{d}t + \int_0^t (\dot{\boldsymbol{\gamma}}^{\mathrm{T}}\boldsymbol{C}_{\mathrm{I}} - \boldsymbol{\gamma}^{\mathrm{T}}\boldsymbol{K}_{\mathrm{I}})\frac{\partial \boldsymbol{T}_{\mathrm{I}}}{\partial s_i}\,\mathrm{d}t \\ &+ \int_0^t -\boldsymbol{\gamma}^T \left(\frac{\partial \boldsymbol{C}_{\mathrm{I}}}{\partial s_i}\dot{\boldsymbol{T}}_{\mathrm{I}} + \frac{\partial \boldsymbol{K}_{\mathrm{I}}}{\partial s_i}\boldsymbol{T}_{\mathrm{I}}\right)\,\mathrm{d}t + \int_0^t (\dot{\boldsymbol{\lambda}}^{\mathrm{T}}\boldsymbol{C}_{\mathrm{II}} - \boldsymbol{\lambda}^{\mathrm{T}}\boldsymbol{K}_{\mathrm{II}})\frac{\partial \boldsymbol{T}_{\mathrm{II}}}{\partial s_i}\,\mathrm{d}t \\ &+ \int_0^t -\boldsymbol{\lambda}^{\mathrm{T}} \left(\frac{\partial \boldsymbol{C}_{\mathrm{II}}}{\partial s_i}\dot{\boldsymbol{T}}_{\mathrm{II}} + \frac{\partial \boldsymbol{K}_{\mathrm{II}}}{\partial s_i}\boldsymbol{T}_{\mathrm{II}}\right)\,\mathrm{d}t + \int_0^t \boldsymbol{\lambda}^{\mathrm{T}}\frac{\partial \boldsymbol{F}_{\mathrm{II}}}{\partial s_i}\,\mathrm{d}t - \boldsymbol{\gamma}^T\boldsymbol{C}_{\mathrm{I}}\left.\frac{\partial \boldsymbol{T}_{\mathrm{I}}}{\partial s_i}\right|_{t=t_{\mathrm{f}}} \\ &- \boldsymbol{\lambda}^{\mathrm{T}}\boldsymbol{C}_{\mathrm{II}}\left.\frac{\partial \boldsymbol{T}_{\mathrm{II}}}{\partial s_i}\right|_{t=t_{\mathrm{f}}}. \end{aligned} \tag{3.21}$$

By grouping the implicit term $\partial \boldsymbol{T}/\partial s_i$ and $\partial \boldsymbol{F}_{\mathrm{II}}/\partial s_i$ for each material Ω_{I} and Ω_{II}, it can be rearranged as follows

$$\begin{aligned}\frac{\partial \tilde{f}}{\partial s_i} &= \int_0^t \left(\boldsymbol{F}_{\mathrm{I}}^{\mathrm{T}} + \dot{\boldsymbol{\gamma}}^{\mathrm{T}}\boldsymbol{C}_{\mathrm{I}} - \boldsymbol{\gamma}^{\mathrm{T}}\boldsymbol{K}_{\mathrm{I}}\right)\frac{\partial \boldsymbol{T}_{\mathrm{I}}}{\partial s_i}\,\mathrm{d}t + \int_0^t \left(\boldsymbol{F}_{\mathrm{II}}^{\mathrm{T}} + \dot{\boldsymbol{\lambda}}^{\mathrm{T}}\boldsymbol{C}_{\mathrm{II}} - \boldsymbol{\lambda}^{\mathrm{T}}\boldsymbol{K}_{\mathrm{II}}\right)\frac{\partial \boldsymbol{T}_{\mathrm{II}}}{\partial s_i}\,\mathrm{d}t \\ &+ \int_0^t \left(\frac{\partial \boldsymbol{F}_{\mathrm{II}}^{\mathrm{T}}}{\partial s_i}\boldsymbol{T}_{\mathrm{II}} + \boldsymbol{\lambda}^{\mathrm{T}}\frac{\partial \boldsymbol{F}_{\mathrm{II}}}{\partial s_i}\right)\,\mathrm{d}t + \int_0^t -\boldsymbol{\gamma}^{\mathrm{T}}\left(\frac{\partial \boldsymbol{C}_{\mathrm{I}}}{\partial s_i}\dot{\boldsymbol{T}}_{\mathrm{I}} + \frac{\partial \boldsymbol{K}_{\mathrm{I}}}{\partial s_i}\boldsymbol{T}_{\mathrm{I}}\right)\,\mathrm{d}t \\ &+ \int_0^t -\boldsymbol{\lambda}^{\mathrm{T}}\left(\frac{\partial \boldsymbol{C}_{\mathrm{II}}}{\partial s_i}\dot{\boldsymbol{T}}_{\mathrm{II}} + \frac{\partial \boldsymbol{K}_{\mathrm{II}}}{\partial s_i}\boldsymbol{T}_{\mathrm{II}}\right)\,\mathrm{d}t - \boldsymbol{\gamma}^T\boldsymbol{C}_{\mathrm{I}}\left.\frac{\partial \boldsymbol{T}_{\mathrm{I}}}{\partial s_i}\right|_{t=t_{\mathrm{f}}} - \boldsymbol{\lambda}^{\mathrm{T}}\boldsymbol{C}_{\mathrm{II}}\left.\frac{\partial \boldsymbol{T}_{\mathrm{II}}}{\partial s_i}\right|_{t=t_{\mathrm{f}}}. \end{aligned} \tag{3.22}$$

The implicit term $\boldsymbol{F}_{\mathrm{II}}$ and its derivative $\partial \boldsymbol{F}_{\mathrm{II}}/\partial s_i$ can be written as

$$\boldsymbol{F}_{\mathrm{II}} = \boldsymbol{K}_{\mathrm{t}}\boldsymbol{T}_{\mathrm{I}}, \tag{3.23}$$

$$\frac{\partial \boldsymbol{F}_{\mathrm{II}}}{\partial s_i} = \frac{\partial \boldsymbol{K}_{\mathrm{t}}}{\partial s_i}\boldsymbol{T}_{\mathrm{I}} + \boldsymbol{K}_{\mathrm{t}}\frac{\partial \boldsymbol{T}_{\mathrm{I}}}{\partial s_i}, \tag{3.24}$$

where

$$\boldsymbol{K}_{\mathrm{t}} = \int_\Omega \boldsymbol{N}^{\mathrm{T}} k_{\mathrm{t}}^{\mathrm{H}} \boldsymbol{N}\,\mathrm{d}\Omega. \tag{3.25}$$

Substitute Eqs. (3.23) and (3.24) into Eq. (3.22) using the symmetry of $\boldsymbol{K}_{\mathrm{t}}$ and combining the implicit term, finally, it can be expressed as

$$\begin{aligned}\frac{\partial \tilde{f}}{\partial s_i} &= \int_0^t (\boldsymbol{F}_{\mathrm{I}}^{\mathrm{T}} + \boldsymbol{\lambda}^{\mathrm{T}}\boldsymbol{K}_{\mathrm{t}} + \boldsymbol{T}_{\mathrm{II}}^{\mathrm{T}}\boldsymbol{K}_{\mathrm{t}} + \dot{\boldsymbol{\gamma}}^{\mathrm{T}}\boldsymbol{C}_{\mathrm{I}} - \boldsymbol{\gamma}^{\mathrm{T}}\boldsymbol{K}_{\mathrm{I}})\frac{\partial \boldsymbol{T}_{\mathrm{I}}}{\partial s_i}\,\mathrm{d}t \\ &+ \int_0^t \left(\boldsymbol{T}_{\mathrm{I}}^{\mathrm{T}}\boldsymbol{K}_{\mathrm{t}} + \dot{\boldsymbol{\lambda}}^{\mathrm{T}}\boldsymbol{C}_{\mathrm{II}} - \boldsymbol{\lambda}^{\mathrm{T}}\boldsymbol{K}_{\mathrm{II}}\right)\frac{\partial \boldsymbol{T}_{\mathrm{II}}}{\partial s_i}\,\mathrm{d}t + \int_0^t \left(\boldsymbol{T}_{\mathrm{I}}^{\mathrm{T}}\frac{\partial \boldsymbol{K}_{\mathrm{t}}}{\partial s_i}\boldsymbol{T}_{\mathrm{II}} + \boldsymbol{\lambda}^{\mathrm{T}}\frac{\partial \boldsymbol{K}_{\mathrm{t}}}{\partial s_i}\boldsymbol{T}_{\mathrm{I}}\right)\,\mathrm{d}t \end{aligned}$$

$$+\int_0^t -\boldsymbol{\gamma}^{\mathrm{T}}\left(\frac{\partial \boldsymbol{C}_{\mathrm{I}}}{\partial s_i}\dot{\boldsymbol{T}}_{\mathrm{I}}+\frac{\partial \boldsymbol{K}_{\mathrm{I}}}{\partial s_i}\boldsymbol{T}_{\mathrm{I}}\right)\,\mathrm{d}t+\int_0^t -\boldsymbol{\lambda}^{\mathrm{T}}\left(\frac{\partial \boldsymbol{C}_{\mathrm{II}}}{\partial s_i}\dot{\boldsymbol{T}}_{\mathrm{II}}+\frac{\partial \boldsymbol{K}_{\mathrm{II}}}{\partial s_i}\boldsymbol{T}_{\mathrm{II}}\right)\,\mathrm{d}t$$

$$-\boldsymbol{\gamma}^{T}\boldsymbol{C}_{\mathrm{I}}\left.\frac{\partial \boldsymbol{T}_{\mathrm{I}}}{\partial s_i}\right|_{t=t_{\mathrm{f}}}-\boldsymbol{\lambda}^{\mathrm{T}}\boldsymbol{C}_{\mathrm{II}}\left.\frac{\partial \boldsymbol{T}_{\ \mathrm{II}}}{\partial s_i}\right|_{t=t_{\mathrm{f}}}. \tag{3.26}$$

Here, by the mean of the adjoint variable method, the arbitrariness of admissible $\boldsymbol{\gamma}$ and $\boldsymbol{\lambda}$ is applied to eliminate implicit terms of $\partial \boldsymbol{T}_{\mathrm{I}}/\partial s_i$ and $\partial \boldsymbol{T}_{\mathrm{II}}/\partial s_i$ by solving adjoint equations along with the boundary conditions shown in the last line of Eq. (3.26). Then manipulating the terms and eliminating the implicit terms $\partial \boldsymbol{T}/\partial s_i$ by arbitrarily selecting an admissible adjoint variable, we obtain the final expression of the transient sensitivity analysis as

$$\frac{\partial \tilde{f}}{\partial s_i}=\int_0^t -\boldsymbol{\lambda}^{\mathrm{T}}(\frac{\partial \boldsymbol{C}_{\mathrm{II}}}{\partial s_i}\dot{\boldsymbol{T}}_{\mathrm{II}}+\frac{\partial \boldsymbol{K}_{\mathrm{II}}}{\partial s_i}\boldsymbol{T}_{\mathrm{II}})\,\mathrm{d}t+\int_0^t -\boldsymbol{\gamma}^{\mathrm{T}}(\frac{\partial \boldsymbol{C}_{\mathrm{I}}}{\partial s_i}\dot{\boldsymbol{T}}_{\mathrm{I}}+\frac{\partial \boldsymbol{K}_{\mathrm{I}}}{\partial s_i}\boldsymbol{T}_{\mathrm{I}})\,\mathrm{d}t$$

$$+\int_0^t (\boldsymbol{T}_{\mathrm{I}}^{\mathrm{T}}\frac{\partial \boldsymbol{K}_{\mathrm{t}}}{\partial s_i}\boldsymbol{T}_{\mathrm{II}}+\boldsymbol{\lambda}^{\mathrm{T}}\frac{\partial \boldsymbol{K}_{\mathrm{t}}}{\partial s_i}\boldsymbol{T}_{\mathrm{I}})\,\mathrm{d}t, \tag{3.27}$$

where $\boldsymbol{K}_{\mathrm{t}}$ is the heat transfer matrix that has been defined as the second terms on the right-hand side of Eqs. (2.12) and (2.13). In addition, the coupling adjoint variable equation for determining $\boldsymbol{\gamma}$ and $\boldsymbol{\lambda}$ corresponding to materials Ω_{I} and Ω_{II} at each time step can be expressed as follows:

$$\boldsymbol{F}_{\mathrm{I}}^{\mathrm{T}}+\dot{\boldsymbol{\gamma}}^{\mathrm{T}}\boldsymbol{C}_{\mathrm{I}}-\boldsymbol{\gamma}^{\mathrm{T}}\boldsymbol{K}_{\mathrm{I}}+(\boldsymbol{T}_{\mathrm{II}}^{\mathrm{T}}+\boldsymbol{\lambda}^{\mathrm{T}})\boldsymbol{K}_{\mathrm{t}}=0\ \text{ in }\Omega_{\mathrm{I}}, \tag{3.28}$$

$$\dot{\boldsymbol{\lambda}}^{\mathrm{T}}\boldsymbol{C}_{\mathrm{II}}-\boldsymbol{\lambda}^{\mathrm{T}}\boldsymbol{K}_{\mathrm{II}}+\boldsymbol{T}_{\mathrm{I}}^{\mathrm{T}}\boldsymbol{K}_{\mathrm{t}}=0\ \text{ in }\Omega_{\mathrm{II}}, \tag{3.29}$$

with

$$\boldsymbol{\lambda}(t_{\mathrm{f}})=0\text{ and }\boldsymbol{\gamma}(t_{\mathrm{f}})=0, \tag{3.30}$$

where t_{f} denotes the final time step. Here, the adjoint variable $\boldsymbol{\lambda}$ in Eq. (3.29) is solved first and then substituted in Eq. (3.28) for computing $\boldsymbol{\gamma}$ as a one-way coupling problem similar to the governing equation in Eqs. (2.8) and (2.9). However, these adjoint equations are solved backward, namely from the final to initial time steps as the process of incremental formulation of the sensitivity analysis.

3.2.2 Derivative of homogenized coefficients

In this section, the derivatives of the homogenized coefficient terms in Eq. (3.27) with respect to the design variable are derived. Firstly, the derivative of the heat

capacity and heat transfer terms are given as

$$\frac{\partial \boldsymbol{C}}{\partial s_i} = \int_\Omega \boldsymbol{N}^{\mathrm{T}} \frac{\partial C^{\mathrm{H}}}{\partial s_i} \boldsymbol{N} \, \mathrm{d}\Omega, \tag{3.31}$$

$$\frac{\partial \boldsymbol{K}_{\mathrm{t}}}{\partial s_i} = \int_\Omega \boldsymbol{N}^{\mathrm{T}} \frac{\partial k_{\mathrm{t}}^{\mathrm{H}}}{\partial s_i} \boldsymbol{N} \, \mathrm{d}\Omega. \tag{3.32}$$

The derivative of these homogenized coefficients can be obtained in the following straightforward manner:

$$\frac{\partial C^{\mathrm{H}}}{\partial s_i} = \frac{1}{|Y|} \int_Y 2 \, \eta {s_i}^{2\eta-1} c \, \rho \, \mathrm{d}y, \tag{3.33}$$

$$\frac{\partial k_{\mathrm{t}}^{\mathrm{H}}}{\partial s_i} = \frac{1}{|Y|} \int_{\partial Y} \frac{\partial \Theta(s_i, s_J)}{\partial s_i} k_{\mathrm{t}} \, \mathrm{d}S, \tag{3.34}$$

with

$$\frac{\partial \Theta(s_i, s_J)}{\partial s_i} = \begin{cases} -1 & \text{if } s_i < s_J \\ 1 & \text{if } s_i > s_J \end{cases}. \tag{3.35}$$

Next, the derivative of the heat conduction $\boldsymbol{K}_{\mathrm{c}}$ contained in the stiffness matrices $\boldsymbol{K}_{\mathrm{I}}$ and $\boldsymbol{K}_{\mathrm{II}}$ can be obtained from the first term of Eqs. (2.12) and (2.13) as

$$\frac{\partial \boldsymbol{K}_{\mathrm{c}}}{\partial s_i} = \int_\Omega \boldsymbol{B}^{\mathrm{T}} \frac{\partial \boldsymbol{k}_{\mathrm{c}}^{\mathrm{H}}}{\partial s_i} \boldsymbol{B} \, \mathrm{d}\Omega. \tag{3.36}$$

However, the analytical expression of Eq. (3.36) is more difficult to derive due to the implicit term of $\partial \boldsymbol{\xi} / \partial s_i$. To overcome this difficulty, we adopt the derived strategy using the adjoint method, similar to the work by Zhou and Li (2008). After some manipulations, we have

$$\frac{\partial \boldsymbol{k}_{\mathrm{c}}^{\mathrm{H}}}{\partial s_i} = \frac{1}{|Y|} \int_Y (\boldsymbol{I} - \nabla \boldsymbol{\xi}) \, \eta \, {s_i}^{\eta-1} k_{\mathrm{c}} (\boldsymbol{I} - \nabla \boldsymbol{\xi}) \, \mathrm{d}y. \tag{3.37}$$

3.2.3 Verification of analytical sensitivity formulation

Here, a sensitivity analysis is conducted to verify the proposed formulation, and the results are compared with those of the numerical analysis by the finite difference method. The geometries and boundary conditions of the two macrostructures, A and B, with a given unit cell, are shown in Fig. 3.5, and the material properties used in this verification are shown in Table 4.1. The unit cell is discretized by $5 \times 5 \times 5$

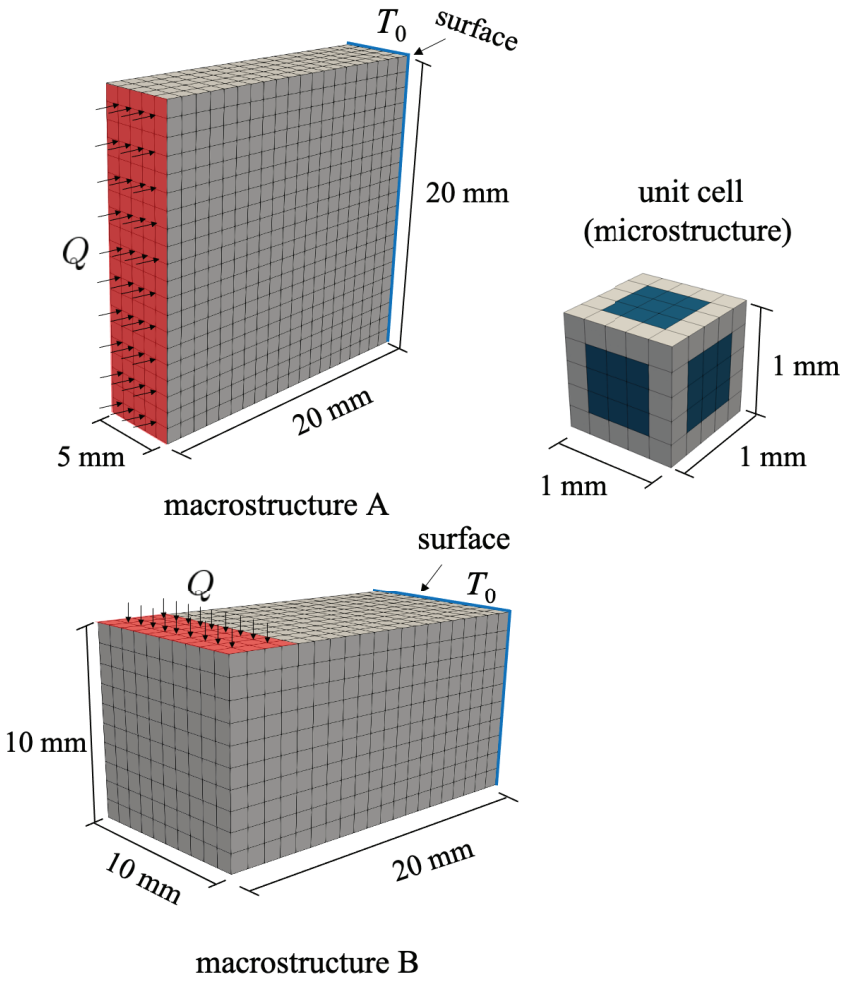

Figure 3.5: Model for sensitivity verification

eight-noded hexahedral elements and the design variable is set to 0.6 (in blue) and 0.4 (in gray) for model A, 0.8 (in blue) and 0.2 (in gray) for model B with the time 0.4 s. As shown in Fig. 3.6, the sensitivities of the two cases obtained from the proposed formulation and finite difference method are in good agreement, with an error of less than 1%. The results are evidence of the reliability and accuracy of the derived sensitivity.

3.3 Numerical examples

In this section, the numerical examples are presented to demonstrate the capability of the proposed topology optimization scheme. In addition, the transient effect and the influence of the size of the designed microstructures are investigated in each example.

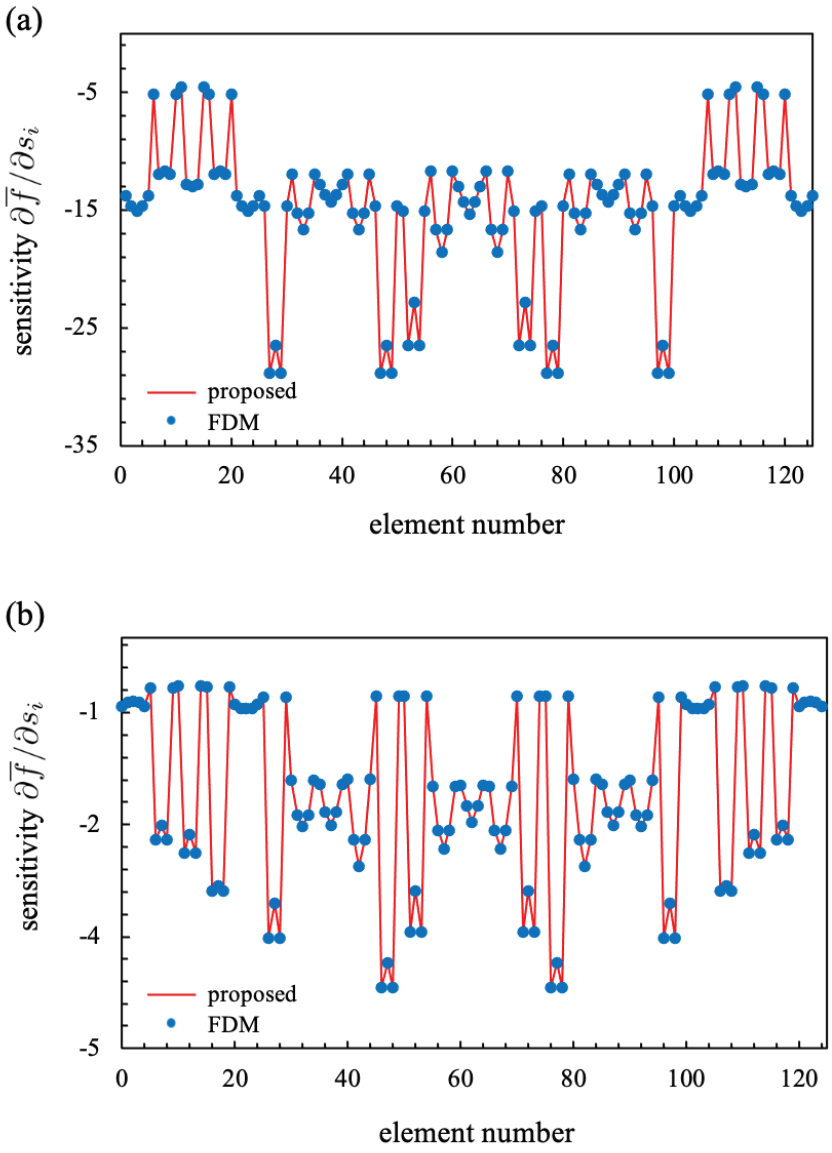

Figure 3.6: Sensitivity of (a) macrostructure A and (b) macrostructure B using the proposed analytical formulation and finite difference method (FDM)

Table 3.1: Material properties of fluid (Ω_{I}) and solid phases (Ω_{II})

	fluid (Ω_{I})	solid (Ω_{II})
specific heat, c [J/(kg・K)]	40	10
density, ρ [kg/m^3]	1000	2000
heat conduction, k_{c} [W/(mm・K)]	0.04	0.001
heat transfer, k_{t} [W/(mm^2・K)]	-	0.000001

3.3.1 Calculation conditions

We consider a three-dimensional heat-conductive porous medium consisting of two materials at the microscopic level. For the sake of simplicity, we apply our proposed design framework to a porous material composed of fluid (high conductivity) and solid (low conductivity) materials, Ω_{I} and Ω_{II}, respectively, similar to those utilized in the study by Terada et al. (2010). In addition, we assume that the fluid in the pores is under the steady-state condition and that the fluid does not flow inside the porous media. Although it is possible that these assumptions introduced by Terada et al. (2010) do not represent the actual situation, we simply follow their lines. The material properties used in this study are shown in Table 1, and three macrostructures are used for the numerical analyses. The macro-and microstructures are discretized by eight-noded hexahedral elements for all the examples, but the number of total elements is varied depending on the problem. The material volume of a unit cell is constrained. The initial volume fraction is set for each numerical example. Of course, different fractions may lead to a different optimization result as the underlying characteristics of gradient-based optimization. To avoid numerical instability during the optimization process, such as checkerboard and mesh-dependent problems, we utilize the sensitivity filtering formulation (Bensøe and Sigmund 2003) as

$$\frac{\partial \overline{f}}{\partial s_i} = \frac{1}{s_i \sum_{j=1}^{N} H_j} \sum_{j=1}^{N} H_j s_j \frac{\partial \tilde{f}}{\partial s_i}, \tag{3.38}$$

where $H_j = r_{\min} - \bar{x}(i,j)$ and $r_{\min}$ is the radius of the filter. Here, $\bar{x}(i,j)$ is the distance between two considered i and j elements. In this study, the filter radius is set to 4 times the element size of the microstructure. Note that grayscale elements on the interface between different materials (or phases) at the final topology may not be vanished just by using a constant filter radius. They may be avoided by changing the filter radius during optimization or by using an alternative filtering scheme, such as a projection scheme (e.g., Kawamoto et al. 2011; Wang et al. 2011), which is a potential method to enforce the sharp interface. However, it has not been employed in this study in order to avoid perturbation on the actual behavior of our final topology. As the initial design conditions, all design variables in the unit cell are set to the same value of volume constraint, except for the center position, where we set the larger value of 0.1 than the others to excitation and stability, as suggested by Kato et al. 2018a. Furthermore, it should be noted that the time step and element size in the transient analysis should be carefully chosen to avoid a spurious oscillation. It has been reported that this type of oscillation occurs as a result of an abrupt change of temperature in the transition region (Gresho and Lee 1981;

Pizzolato et al. 2017). To deal with this problem in a different way, many stabilized finite element techniques have been proposed (e.g., Ilinca and Hetu 2002; Bochev et al. 2004). However, in order to avoid further complexity in the mathematical formulations, those specific stabilization schemes are not implemented in this study.

3.3.2 Numerical example 1

In the first example, we consider the macrostructure subjected to three different loading conditions with heat flux $Q = 0.05$ W/mm^2 and temperature constraint $T_0 = 0$ K. Details of the boundary condition are shown in Fig. 3.7. These configurations are set to be simple enough that the obtained optimal microstructure can be easily

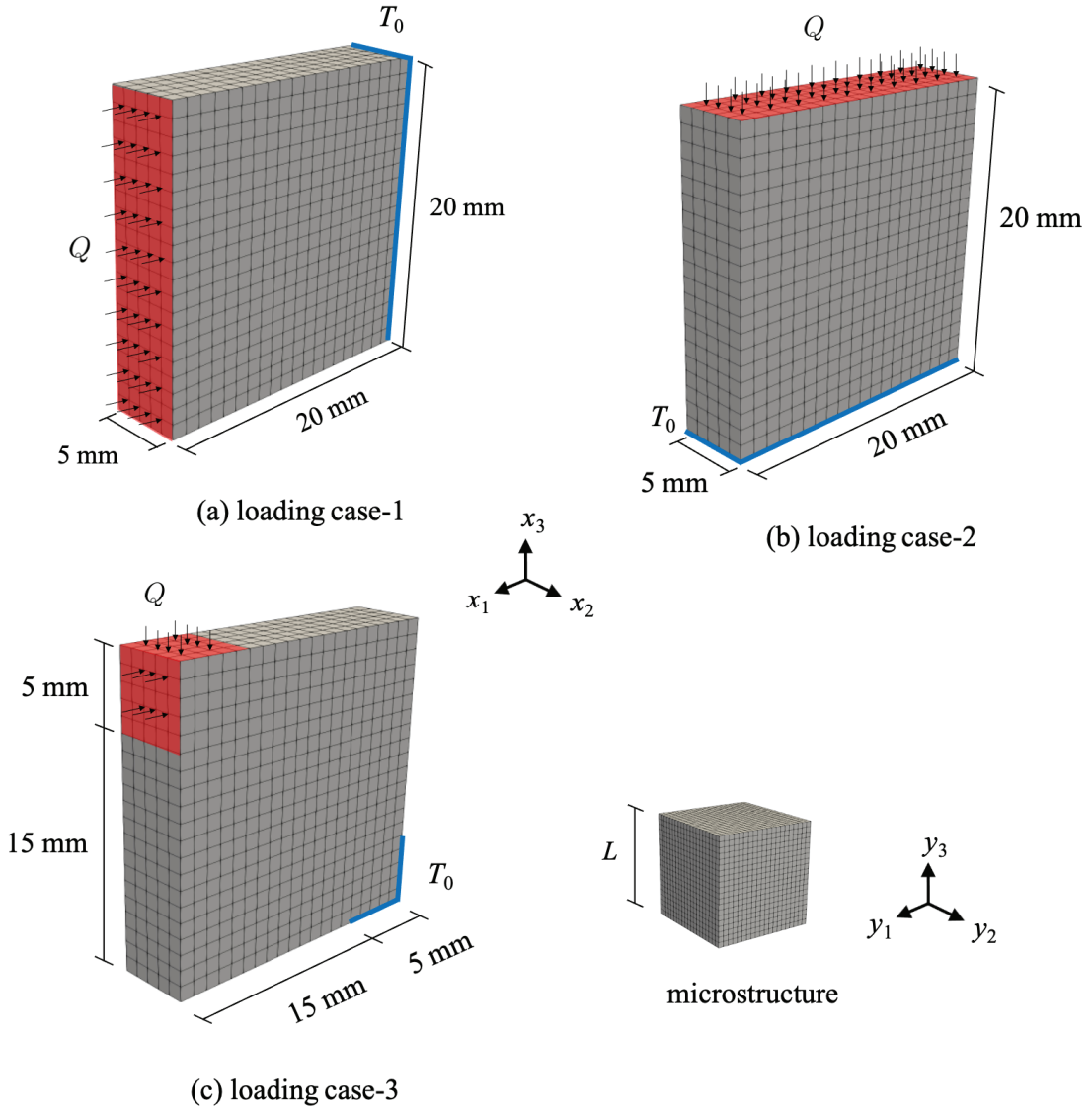

Figure 3.7: The rectangular macrostructure subjected to three loading conditions with temperature constraint, and its microstructure design

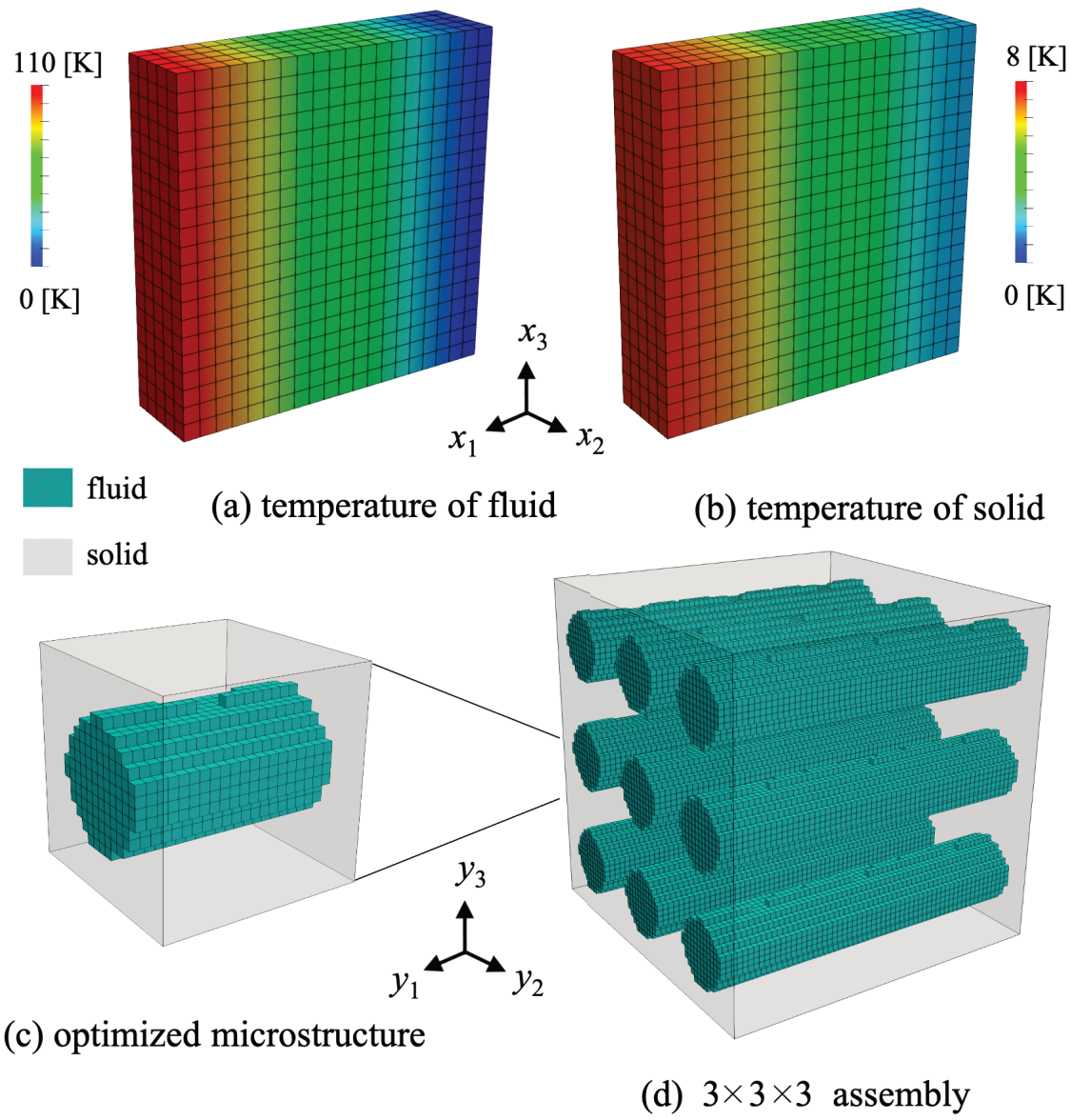

Figure 3.8: Optimization results under loading case-1

understood and to allow for preliminary verification. The macroscopic structure is discretized by eight-noded hexahedral elements and the total number of elements is $20 \times 20 \times 5$ elements. In this example, the objective is to determine the optimal layout in a microstructure which is periodically distributed throughout the entire macrostructure. In other words, the macroscopic heat dissipative performance is maximized by designing its microstructure layout. The constraint of the microscopic material volume is assumed to be less than 30 % of the fluid. The microstructure is discretized by $20 \times 20 \times 20$ elements and the size of the microstructure is set at 1 mm. In this investigation, we set the target period of time at 0.5 s with a total number of 100 time steps.

Figure 3.8 illustrates the optimization results for loading case-1. Also, the tem-

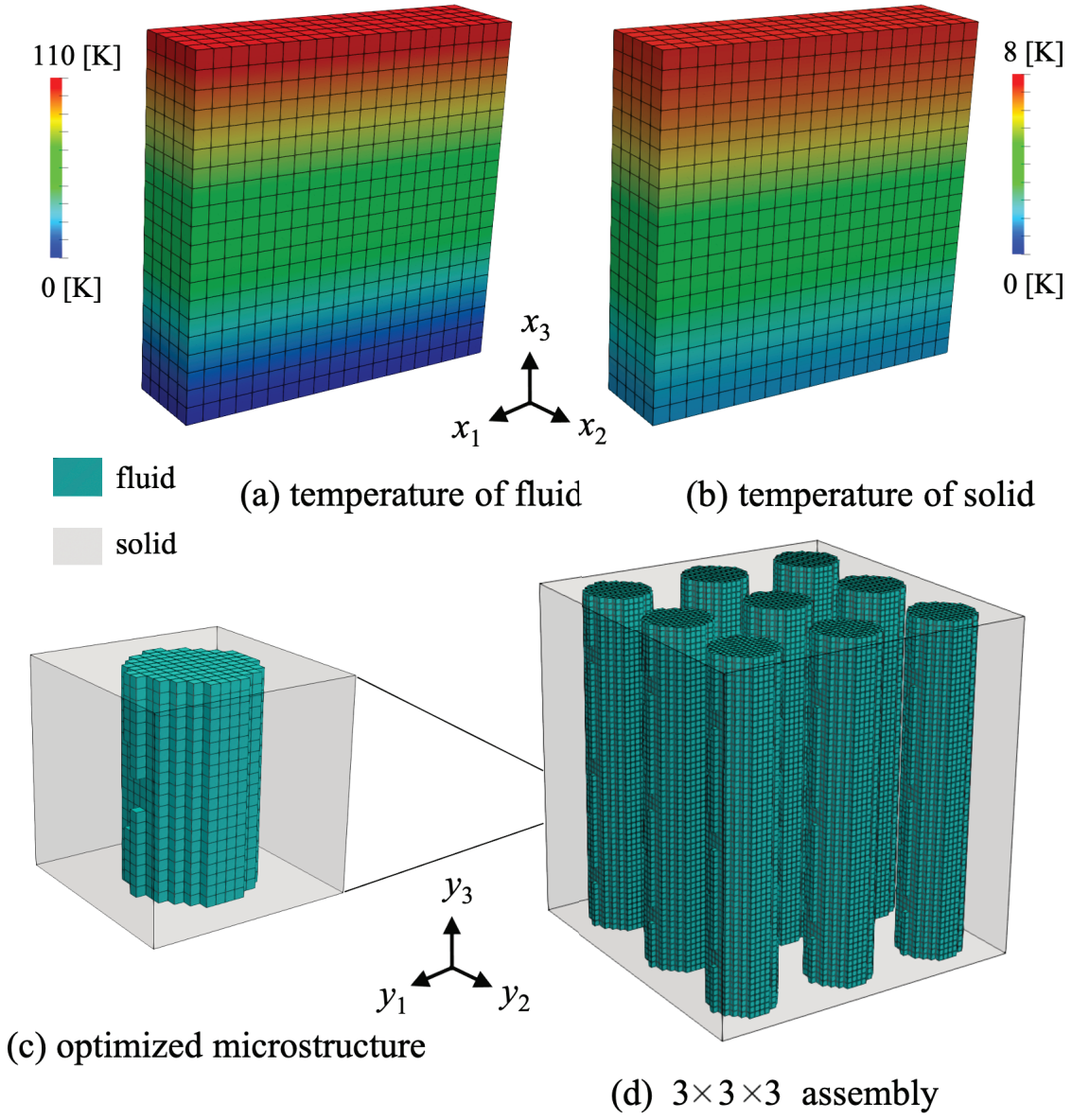

Figure 3.9: Optimization results under loading case-2

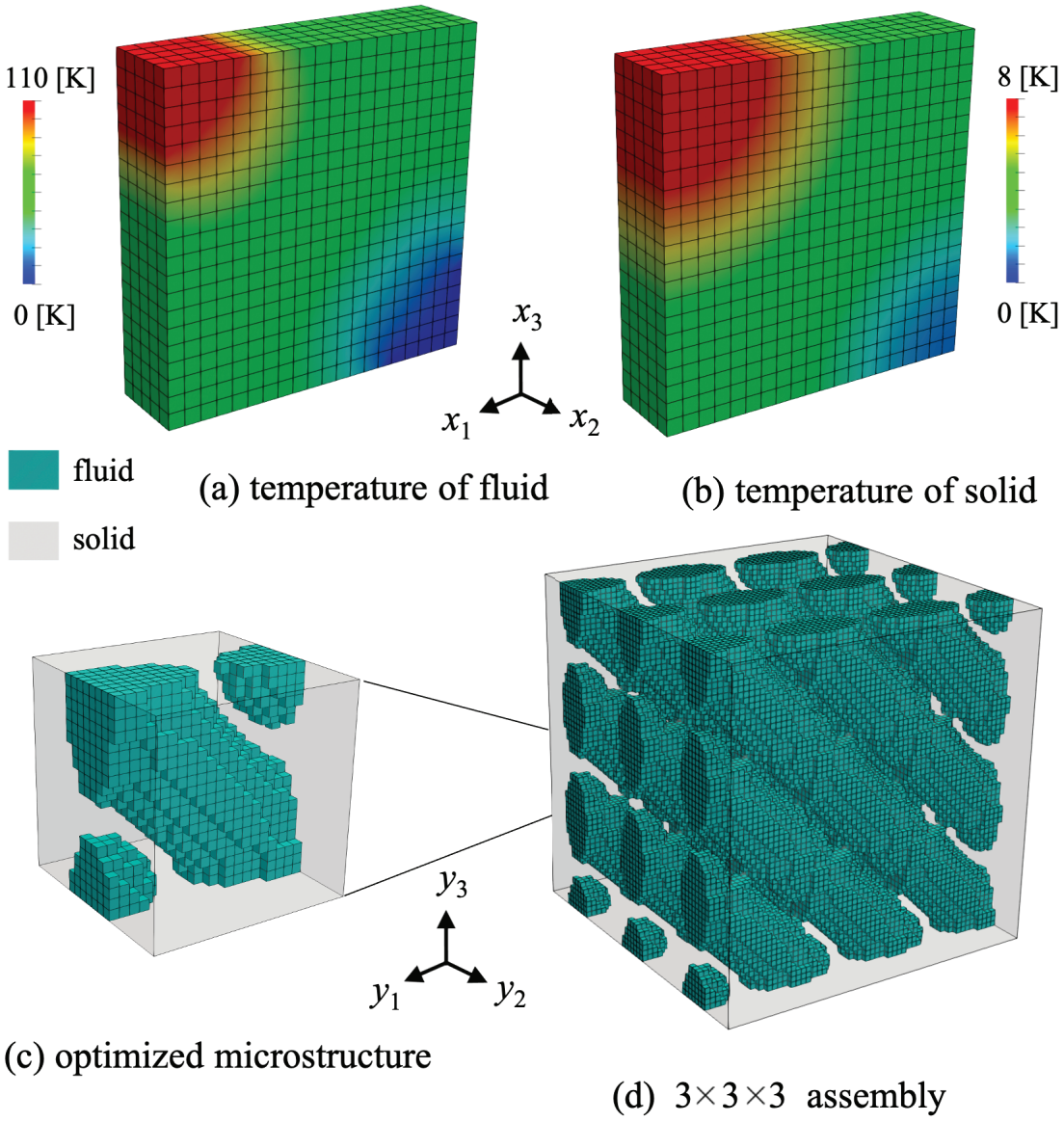

Figure 3.10: Optimization results under loading case-3

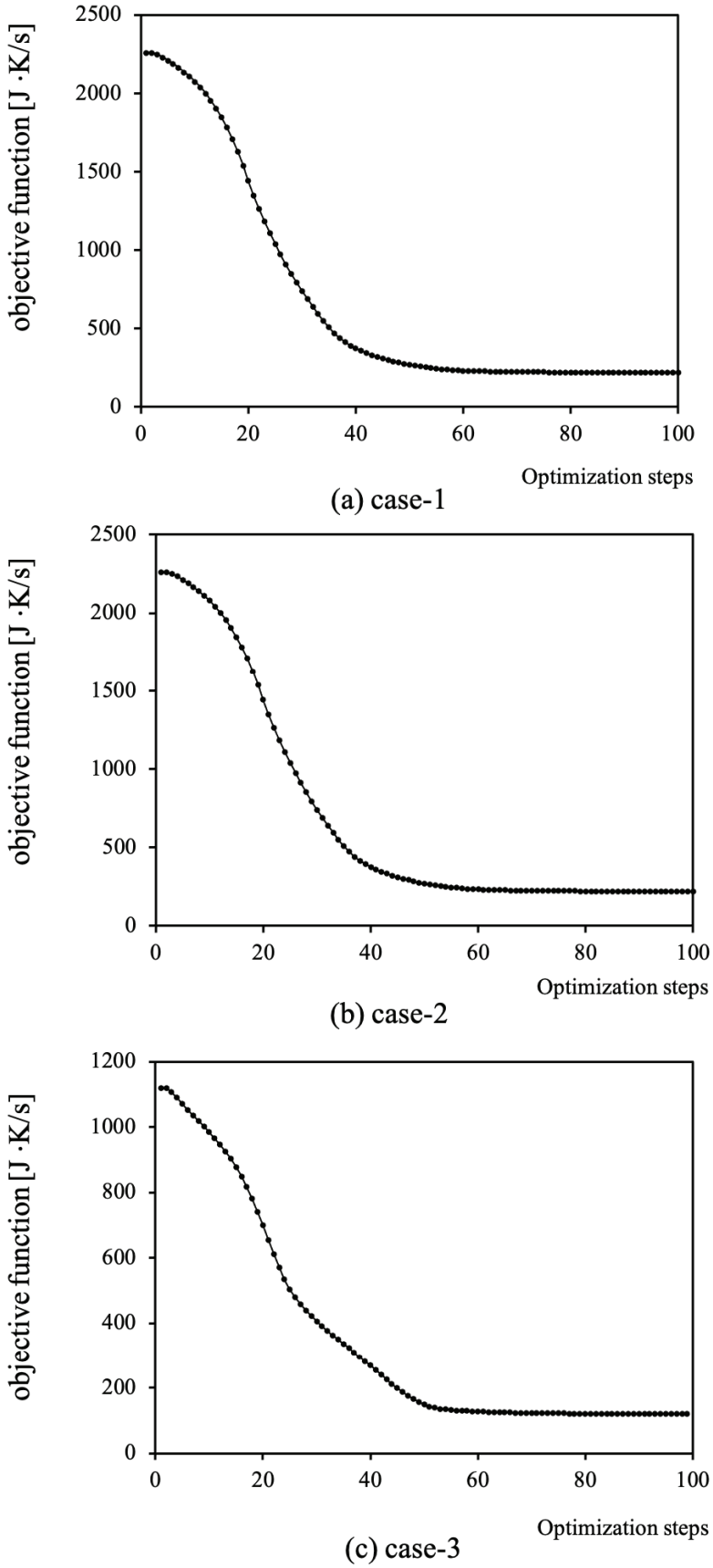

Figure 3.11: History of objective function value during optimization

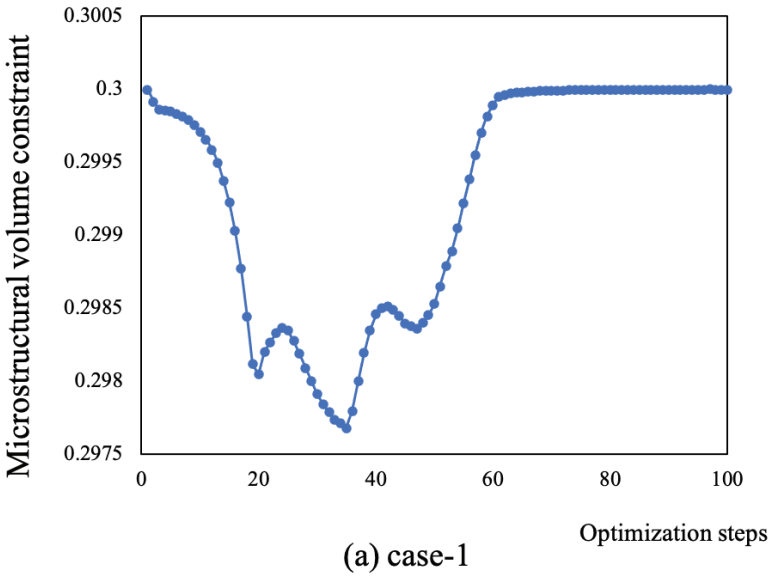

(a) case-1

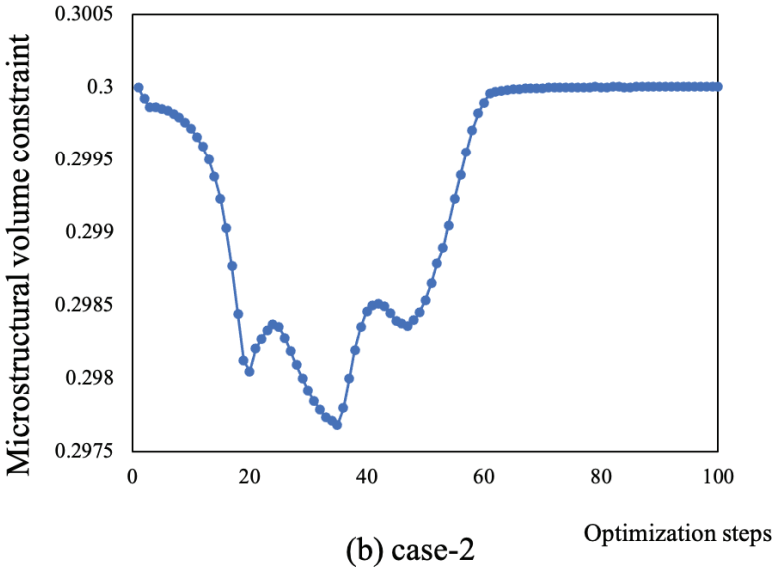

(b) case-2

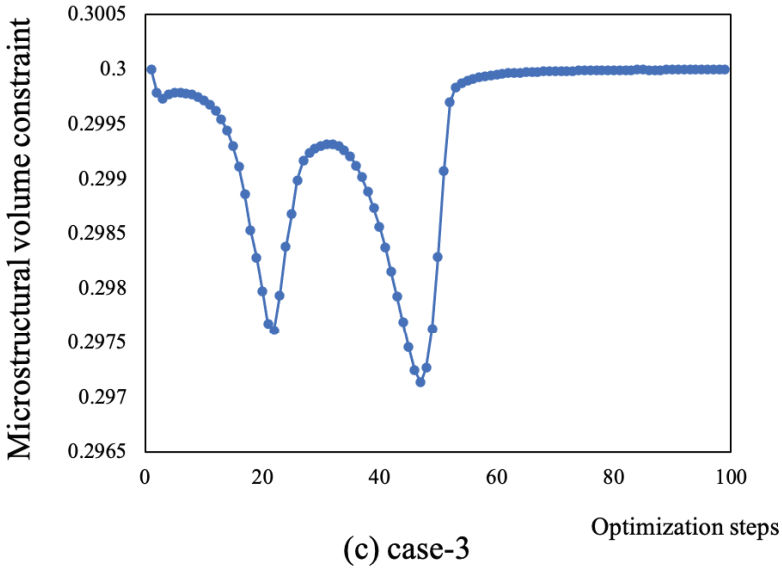

(c) case-3

Figure 3.12: History of microstructural volume constraint

perature distributions on the solid and fluid materials are shown in Figs. 3.8(a) and (b) and the optimized microstructure and its assembly are shown in Figs. 3.8(c) and (d), respectively. It can be seen that the fluid (high thermal conductivity material) appears in the direction of the temperature distribution path, which mainly occurs along the x_1-axis. This implies that the high thermal conductivity material in the microstructure plays a major role in the thermal dissipation of the macrostructure. This tendency can be found in many works of topology optimization for the heat conduction problem (e.g., Kato et al. 2018; Pizzolato et al. 2019; Seo et al. 2020). The results under loading case-2 are shown in Fig. 3.9. The results are similar to those of the previous loading case with the only change being that the loading direction becomes the x_3-axis. The same topology, except for the direction, can be clearly seen in Figs. 3.9(c) and (d). This confirms that there is a strong relationship between the optimized microstructure, especially in the case of the high thermal conductivity material, and the pattern of temperature distribution in the macrostructure.

Figure 3.10 shows the optimization results for loading case-3. Obviously, this is a simple diagonal loading pattern, as shown in the temperature distribution of Figs. 3.10(a) and (b). The optimized microstructure is presented in Figs. 3.10(d) and (e). As we can see, the fluid is diagonally formed in the y_1y_3-plane to dissipate temperature following the temperature path in the macrostructure (in the x_1x_3-plane). Again, these results are in good agreement with the tendency discussed earlier.

Figure 3.11 and Figure 3.12 indicate the history of the objective function and microstructural volume constraint during the optimization process for the three loading cases. It can be clearly seen that all cases show good convergence trends to the optimal results within 100 steps.

These results indicate that the proposed two-scale optimization framework provides a reasonable optimized microstructure based on the mechanism of heat dissipation in the macrostructure under consideration.

3.3.3 Numerical example 2

Next, we focus on the plate-like macrostructure subjected to a heat flux $Q = 0.05$ W/mm^2 at the center of the top surface and the temperature constraint $T_0 = 0$ K at the four edge lines. The dimension and boundary condition are shown in Fig. 3.13. The number of elements is $20 \times 20 \times 5$ for the macrostructure and $20 \times 20 \times 20$ for the microstructure. The volume constraint of the fluid is set at less than 50 %. In the first investigation, we use the microstructure with a side length of L= 0.5 mm and set the target periods of time at 0.05 s and 0.5 s, representing short and long periods, to determine the influence of time on the optimal microstructure.

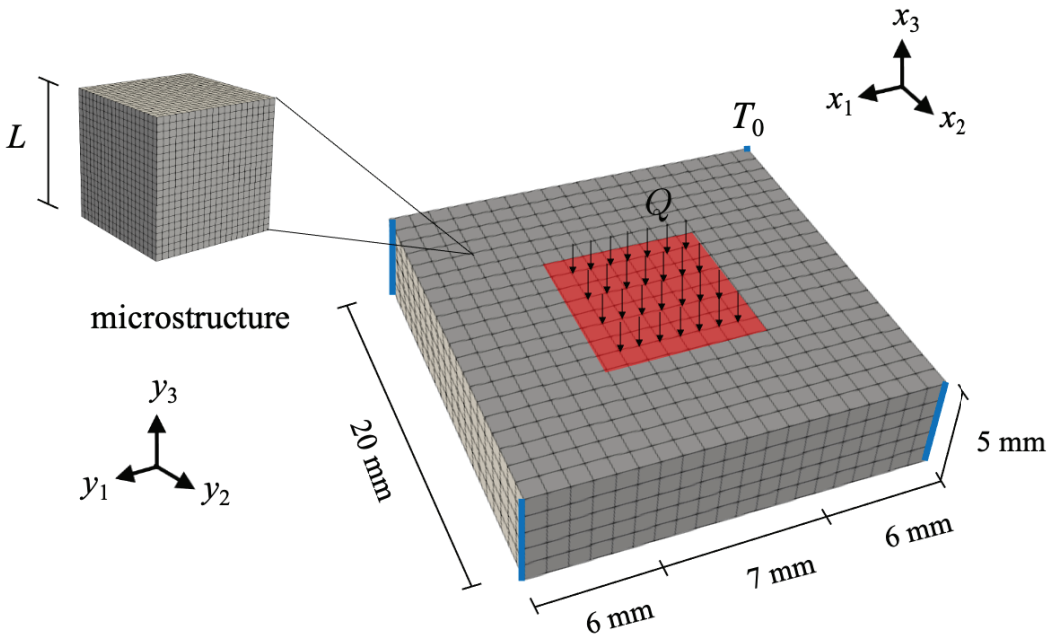

Figure 3.13: Plate-like macrostructure subject to heat flux at center and its microstructure

Figure 3.14 shows the optimization results for the 0.05 s period of time. Fig. 3.14(a) explains the temperature distribution in the macrostructure, and Fig. 3.14b displays the topologies of the fluid regions at several optimization steps. It can be seen that the fluid is first formed near the center of the unit cell and then continuously extends in the y_1-, y_2- and y_3 axial directions. The layout of this high thermal conductivity material corresponds well with the temperature distribution in the macrostructure.

Next, Fig. 3.15 shows the optimization results for the 0.5 s period of time. As a longer time period, the temperature is distributed over the entire macrostructure, as shown in Fig. 3.15(a). From the investigation of each time step, we observe that the temperature distribution is dominant in the x_1x_2-plane in the macrostructure and in the x_3-direction, respectively. This behavior affects the optimized microstructure during optimization, as shown in Fig. 3.15(b). In addition, the microstructural volume constraint is plotted in Fig. 3.16.

To validate the optimized microstructure obtained above, a heat analysis was conducted for the two optimized microstructures shown in Fig. 3.14(c) and Fig. 3.15(c), and the responses were compared at certain times. As mentioned earlier, the microstructure in Fig. 3.14(c) is designed for the 0.05 s period of time, and that in Fig. 3.15(c) is $t = 0.5$ s. Fig. 3.17 shows the results of the heat conduction analysis. The vertical axis shows the maximum temperature in the macrostructure and the horizontal axis represents time. It can be seen that, at the early stage, the maximum temperature of the optimized microstructure for 0.05 s is lower than that of

optimized microstructure for 0.5 s while at the final time step, the result for the 0.5 s period of time is lower.

Furthermore, to confirm the performance of these two topologies, the same boundary conditions were used with different target times (0.05 s and 0.5 s). The objective function values are plotted in Fig. 3.18. Obviously, for the 0.05 s period of time, the optimized topology gives a lower value, while the heat dissipative performance of the 0.5 s period of time is better. Here, these results highlight the significant effect that transient conditions can have on the layout of optimal microstructure.

Apart from this capability, another attractive feature of the proposed optimization framework is that the effect of the microstructure size (side length L of unit cell) on the homogenized heat transfer coefficient $k_{\mathrm{t}}^{\mathrm{H}}$ can be considered in the optimization process. In order to demonstrate the details of this feature, two further investigations were carried out to determine the relationship between the objective function and the heat transfer coefficient k_{t} used in Table 4.1 and the microstructure size under the same configurations adopted earlier.

Firstly, optimization is performed using four different heat transfer coefficients k_{t}. The corresponding objective function values and each optimized microstructure for the target periods of time, 0.05 s and 0.5 s, are plotted in Figs. 3.19 (top)(a)-(d) and 3.20 (top)(a)-(d), respectively. It can be seen that the objective function value decreases when the heat transfer coefficient k_{t} increases. This implies that more heat is transferred from fluid to solid through the heat transfer effect, in effect reducing the heat compliance (objective function) of the designed structure shown in Eq. (3.13). Obviously, the proposed optimization method can enhance the design of heat dissipation in a porous material by considering the macroscopic heat transfer coefficient k_{t}. Meanwhile, it can be observed that the optimized microstructure becomes asymmetric when a large value of k_{t} is used. This is caused by the flexible design of the fluid-solid interface to achieve the minimization of the objective function. These results are evidence that we successfully incorporated two crucial characteristics of a porous material, heat conduction and transfer, into the proposed optimization method.

Using similar configurations, the effect of the size of the microstructure (side length L of unit cell) is determined for the target periods of time of 0.05 s and 0.5 s, as shown in Figs. 3.19 (bottom)(a)-(d) and 3.20 (bottom)(a)-(d). The objective function value is decreased when the side length L is small. In addition, the topologies similar to those in Figs. 3.19 (top)(a)-(d) and 3.20 (top)(a)-(d) are likely due to the size-dependent term that is introduced in Eq. (3.6), which reduces the size of the microstructure (side length L of unit cell) and therefore increases the value of the homogenized heat transfer coefficient $k_{\mathrm{t}}^{\mathrm{H}}$ in a manner akin to increasing the heat

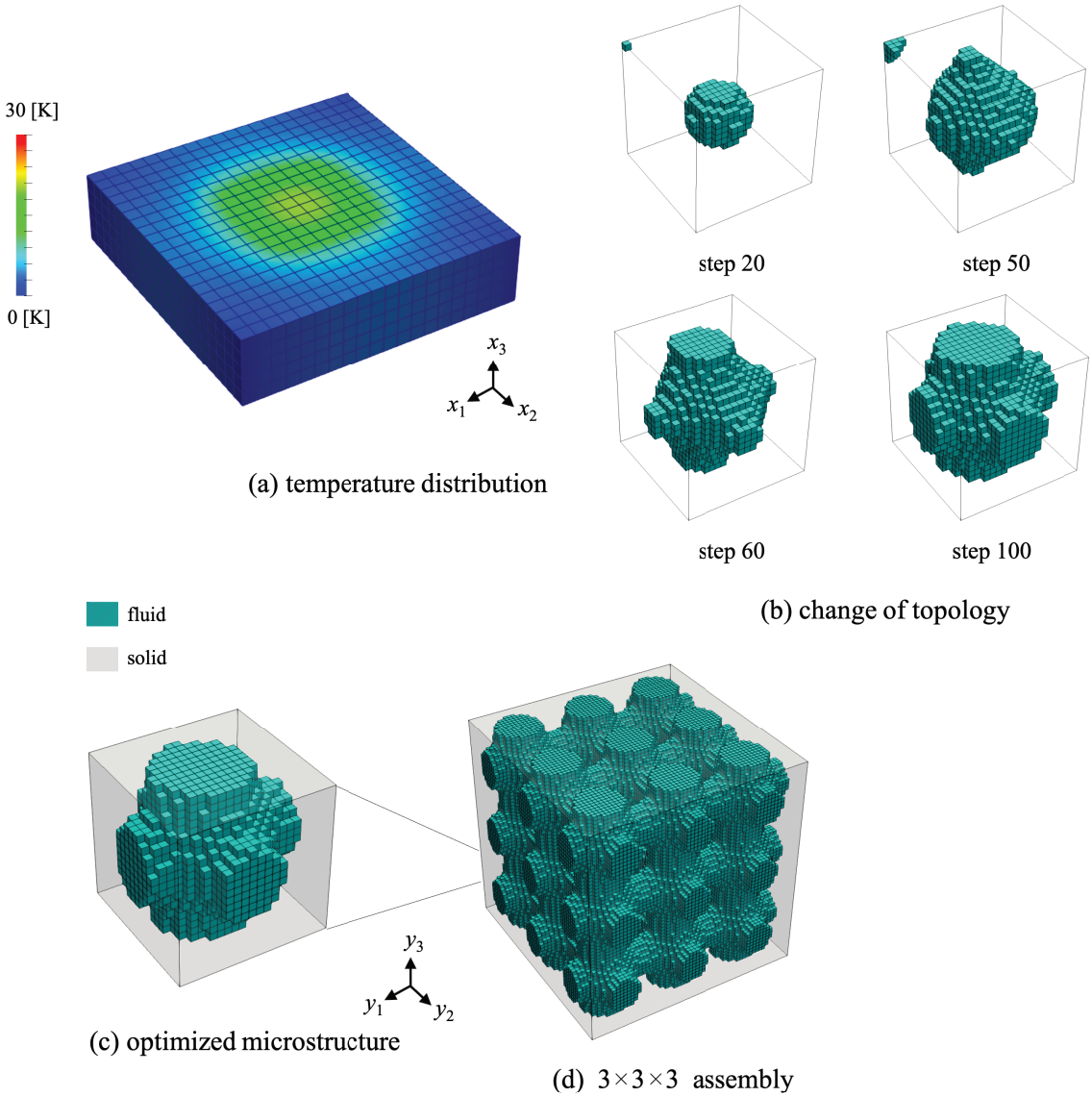

(a) temperature distribution

(b) change of topology

(c) optimized microstructure

(d) 3×3×3 assembly

(e) optimization history

Figure 3.14: Optimization results of plate-like structure for the 0.05 s period of time

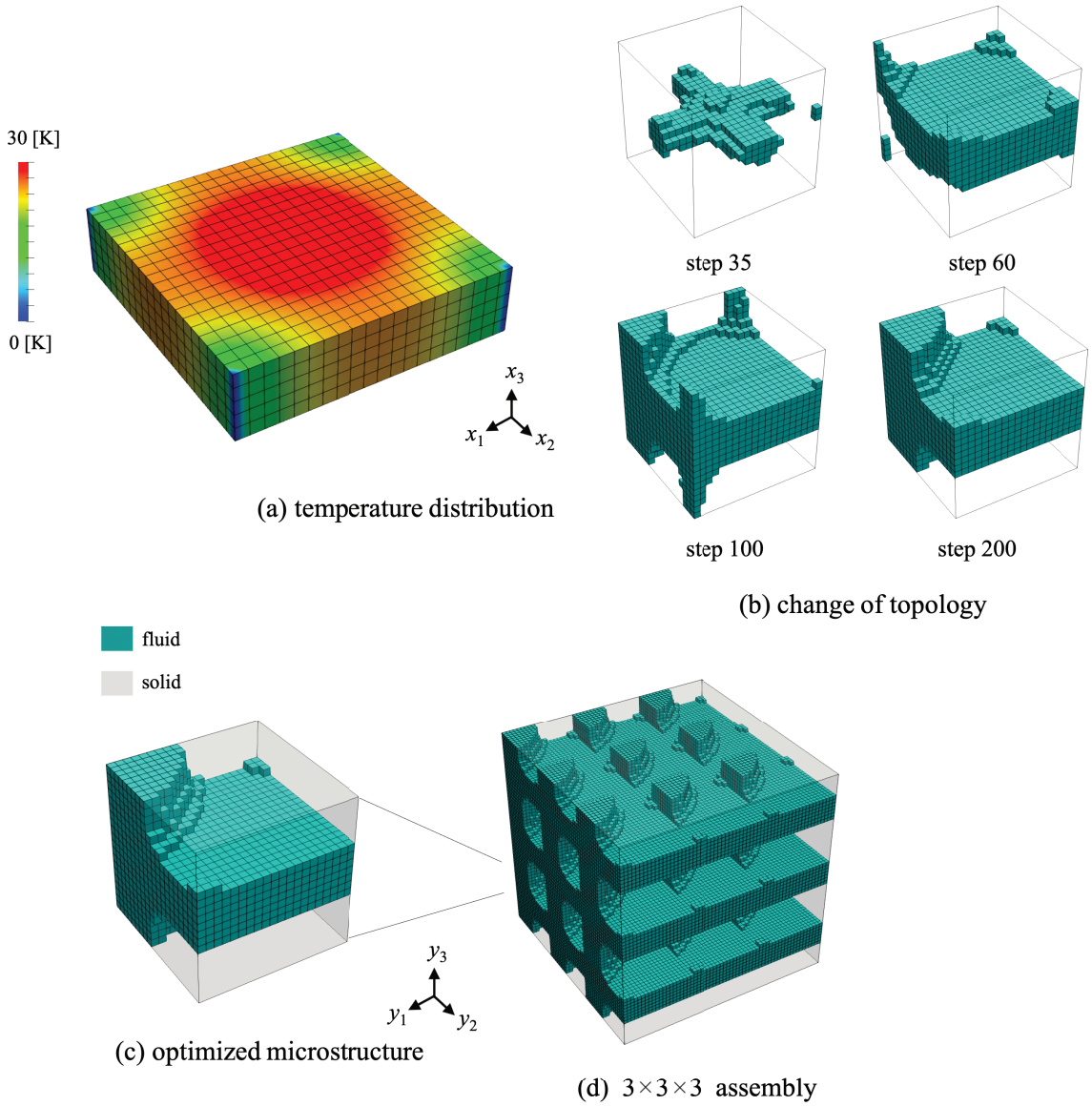

(a) temperature distribution

(b) change of topology

(c) optimized microstructure

(d) 3×3×3 assembly

(e) optimization history

Figure 3.15: Optimization results of the plate-like structure for the 0.5 s period of time

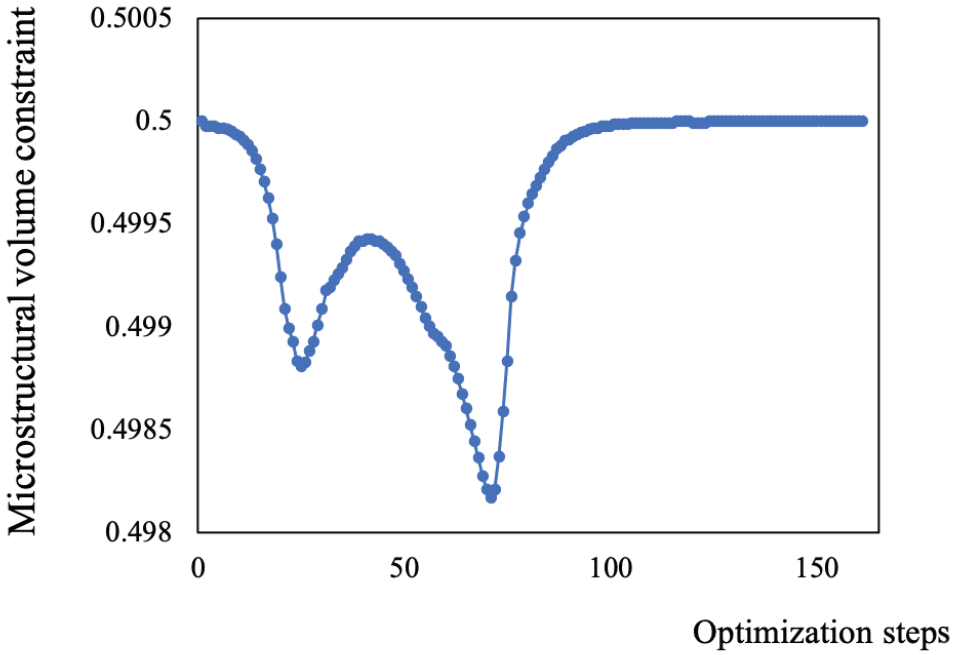

(a) Case 0.05 s

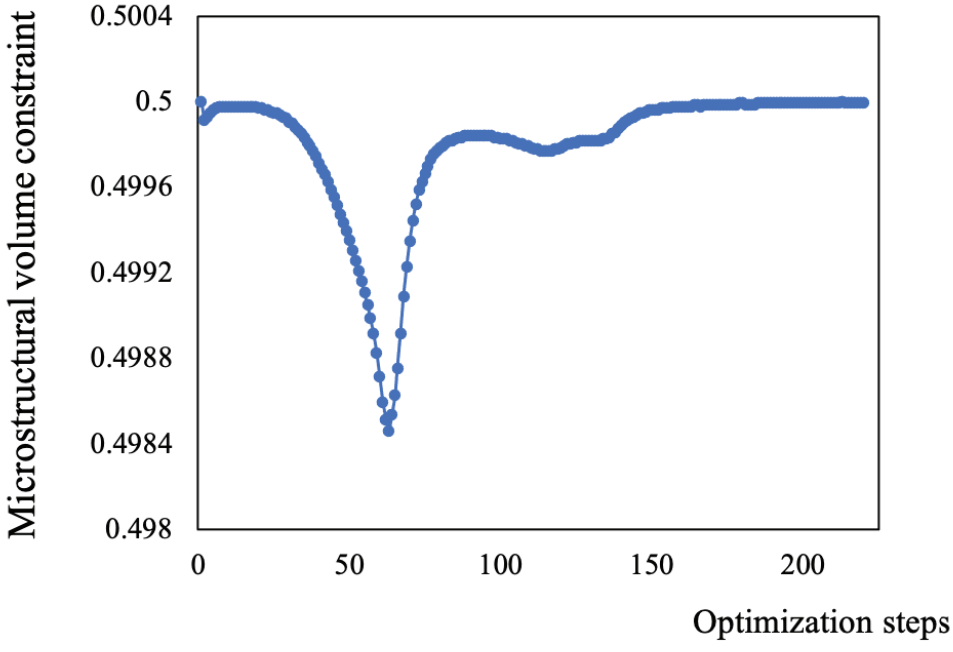

(b) Case 0.5 s

Figure 3.16: History of microstructural volume constraint

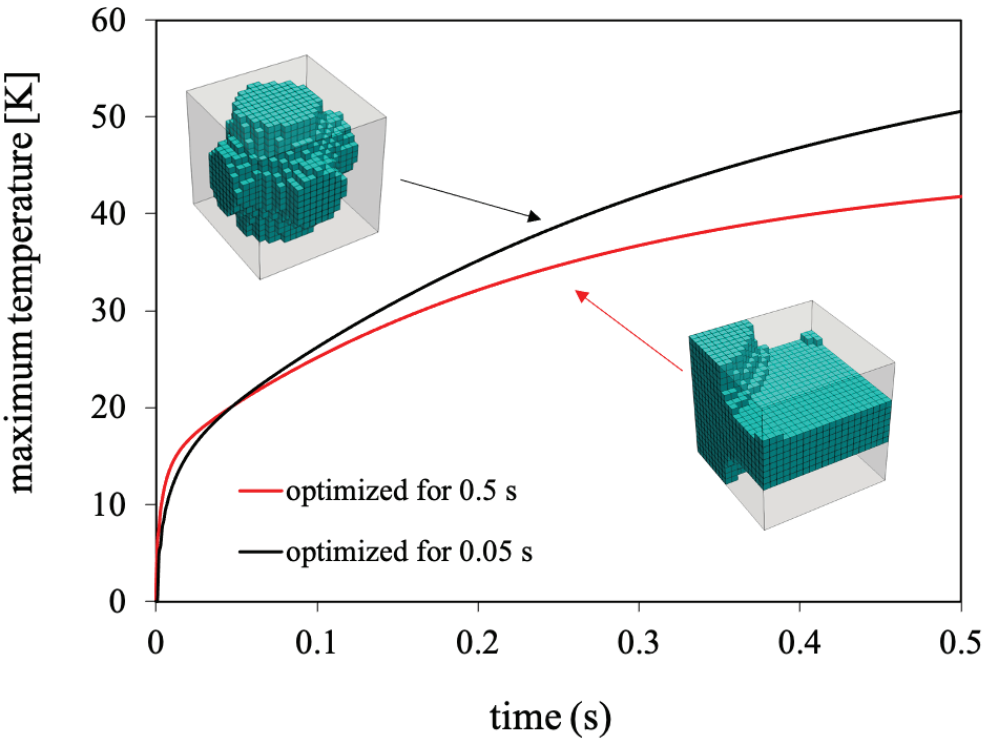

Figure 3.17: Maximum temperature on the plate-like macrostructure for the 0.5 s period of time for the two optimized microstructures

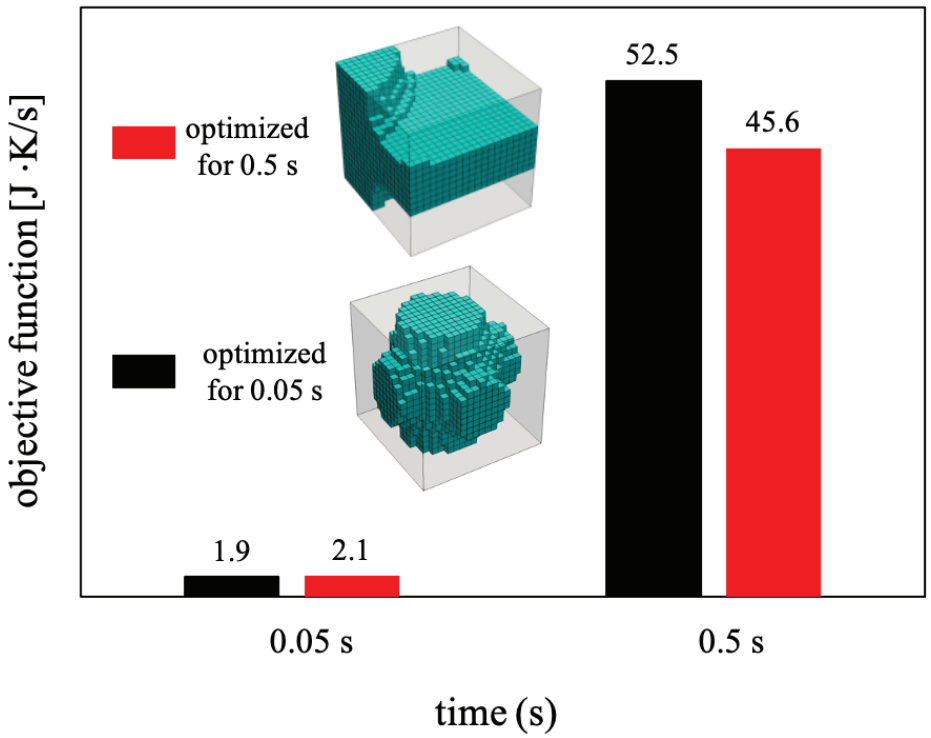

Figure 3.18: Comparison of objective function values for the case of two optimized microstructures for the 0.05 s and 0.5 s periods of time

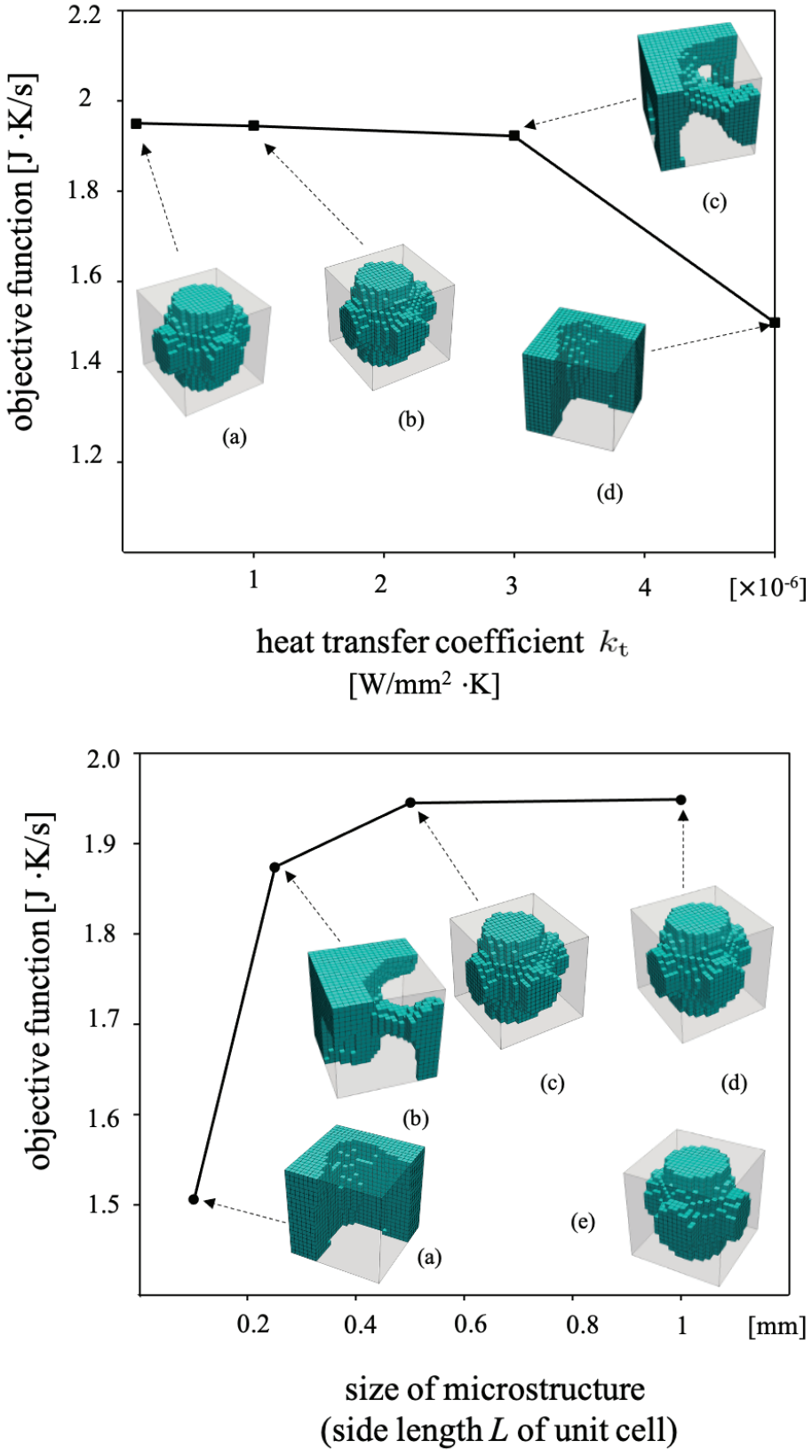

Figure 3.19: Relationship between objective function and (top) heat transfer coefficient, (bottom) size of the microstructure for the 0.05 s period of time

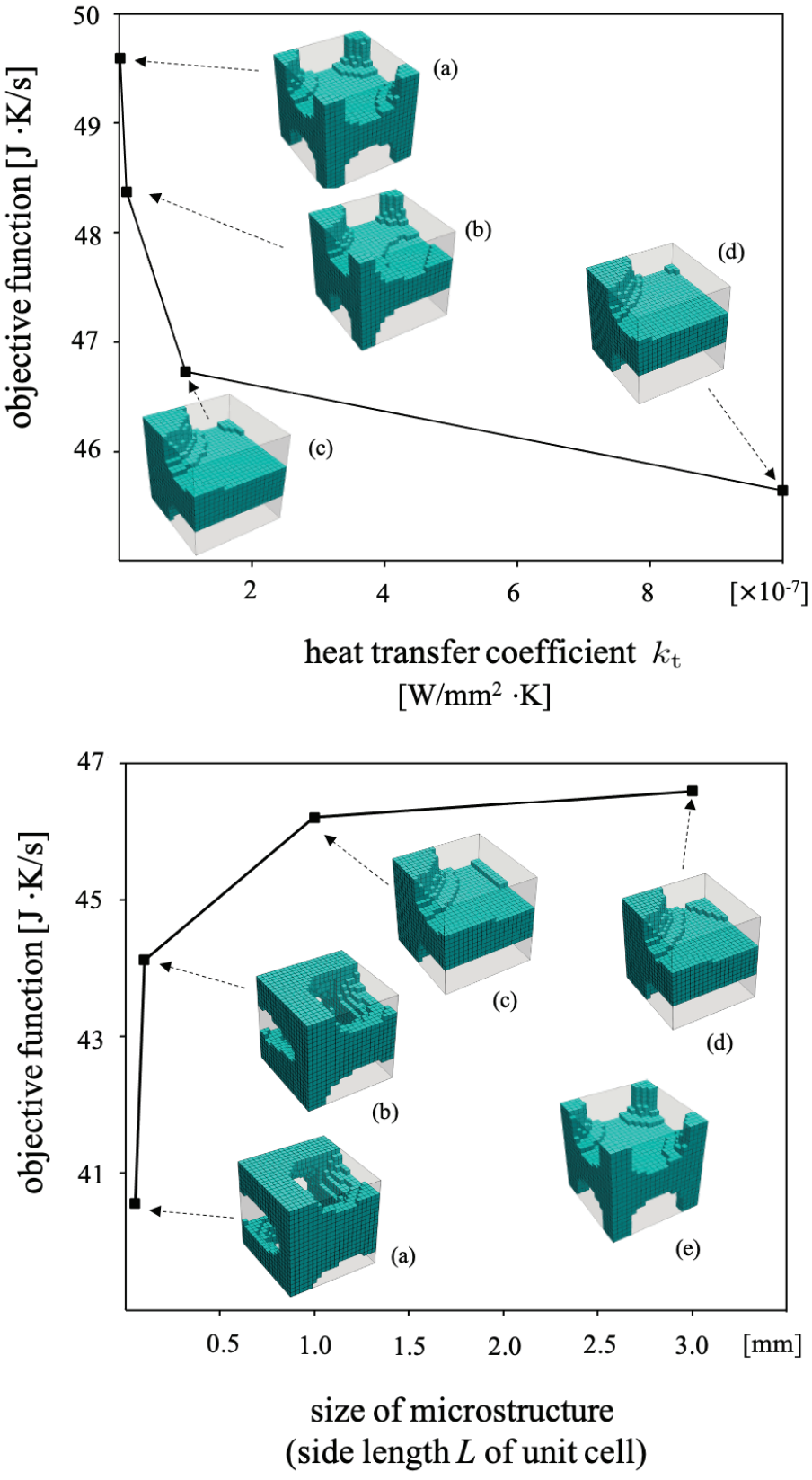

Figure 3.20: Relationship between the objective function and (top) heat transfer coefficient, (bottom) size of the microstructure for the 0.5 s period of time

transfer coefficient k_{t} directly. A detailed explanation of this relation can be found in Terada et al. (2010). Besides, to confirm the relationship between the side length L and the heat transfer coefficient k_{t}, the side length L for use in the numerical investigation is set such that it is large enough to reproduce the non-heat transfer condition. The results are shown in Figs. 3.19 (bottom)(e) and 3.20 (bottom)(e). It can be clearly seen that layout of the obtained microstructures is symmetric and that the topology is almost the same as that shown in Figs. 3.19 (top)(a) and 3.20 (top)(a).

3.3.4 Numerical example 3

The beam-like macrostructure above was subjected to heat flux $Q = 0.05$ W/mm^2 on the top surface, and the temperature constraint $T_0 = 0$ K on the surface of the other end side. Details of the geometry are shown in Fig. 3.21. $10 \times 10 \times 30$ elements are used for the macrostructure and $20 \times 20 \times 20$ elements for the microstructure. The volume constraint of the microstructure for the fluid region is set at less than 30 % and the size of the microstructure is set at 1 mm.

Firstly, Figs. 3.22 and 3.23 illustrate the obtained temperature distributions in

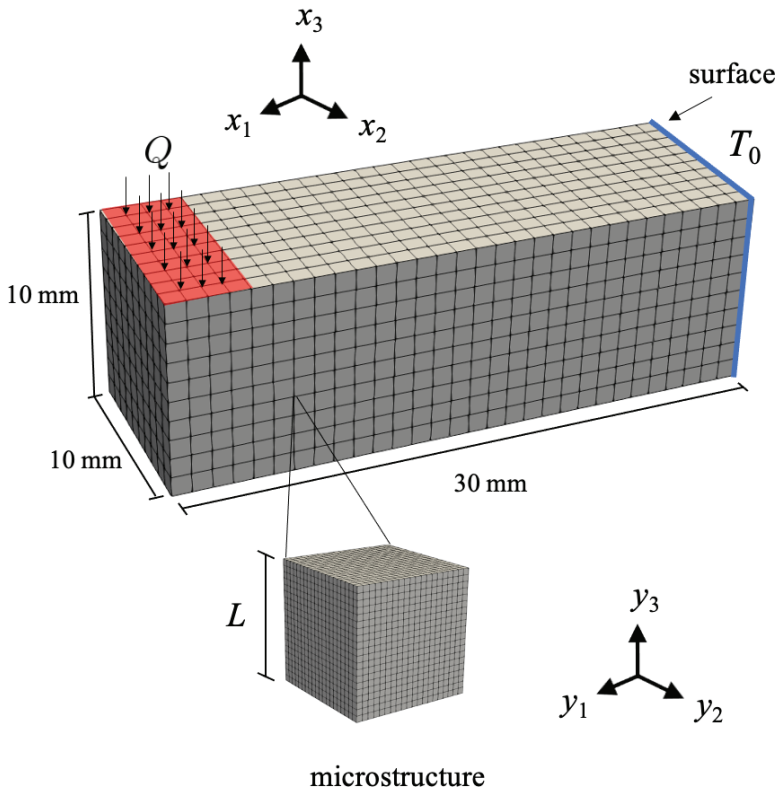

Figure 3.21: A beam-like macrostructure along with boundary condition, and its microstructure design

the fluid together with its optimized microstructure for the two sets of the target periods of time, 0.05 s and 0.5 s. The topologies of the obtained microstructures clearly differ for different temperature distributions in the macrostructure. As can be seen for the 0.05 s period of time, the temperature is mainly distributed along the diagonal direction (x_1x_3-plane) in the vicinity of the heat flux applied. Therefore, the fluid in the optimized microstructure is mainly formed in the y_1y_3-plane following the temperature distribution, as indicated in Fig. 3.22. For the 0.5 s period of time, the temperature is distributed vertically and horizontally in the vicinity of the Neumann boundary, while it is distributed horizontally for the other regions. As a result, a combined topology with both diagonal and horizontal directions appears, as shown in Fig. 3.23. Again, this is evidence that the temperature distribution in the macrostructure strongly affects the layout of high conductive material Ω_{I} in the optimized microstructure.

Next, we investigate the performance of the obtained microstructures shown above by a transient heat analysis under the same analysis conditions as the previous investigation. Both analyses are conducted for the 0.5 s period of time. In Fig. 3.24, it can be seen that the maximum temperature for the 0.05 s period of time is lower at the early stage, and thereafter the maximum temperature for the target time of 0.5 s becomes lower. In addition, we compared the objective function values for the two cases with the optimized microstructure for the 0.05 s and 0.5 s periods of time. The results are presented in Fig. 3.25. As we can see, the performance of each topology for each optimal microstructure is better for the corresponding period of time. These results clearly show that the implementation of the transient heat analysis for topology optimization enhances the performance of the optimal microstructure to that of the steady-state framework.

While enjoying the transient effect on the two-scale analysis, we notice from this example that the temperature distribution pattern differs significantly in each region of the macrostructure. Therefore, using the microstructure to design the entire macrostructure may not provide the best performance in such circumstances. To overcome this, the proposed optimization framework is extended to design multiple microstructures simultaneously. Note here that we do not consider the connectivity of each design region at this stage to simplify and direct investigate the transient and size-dependent effects in multiple design regions scheme. However, if necessary, we can adopt these proposed schemes (Sivapuram et al. 2016; Du et al. 2018; Liu et al. 2020) to connect each design region.

To investigate the performance, we optimized the topology of a microstructure under the same condition as that shown in Fig. 3.23 (for the 0.5 s period of time) by assigning three designed domains: 1, 2 and 3. Fig. 3.26 shows the optimized microstructure for each designed domain. In design domain 1, as discussed earlier,

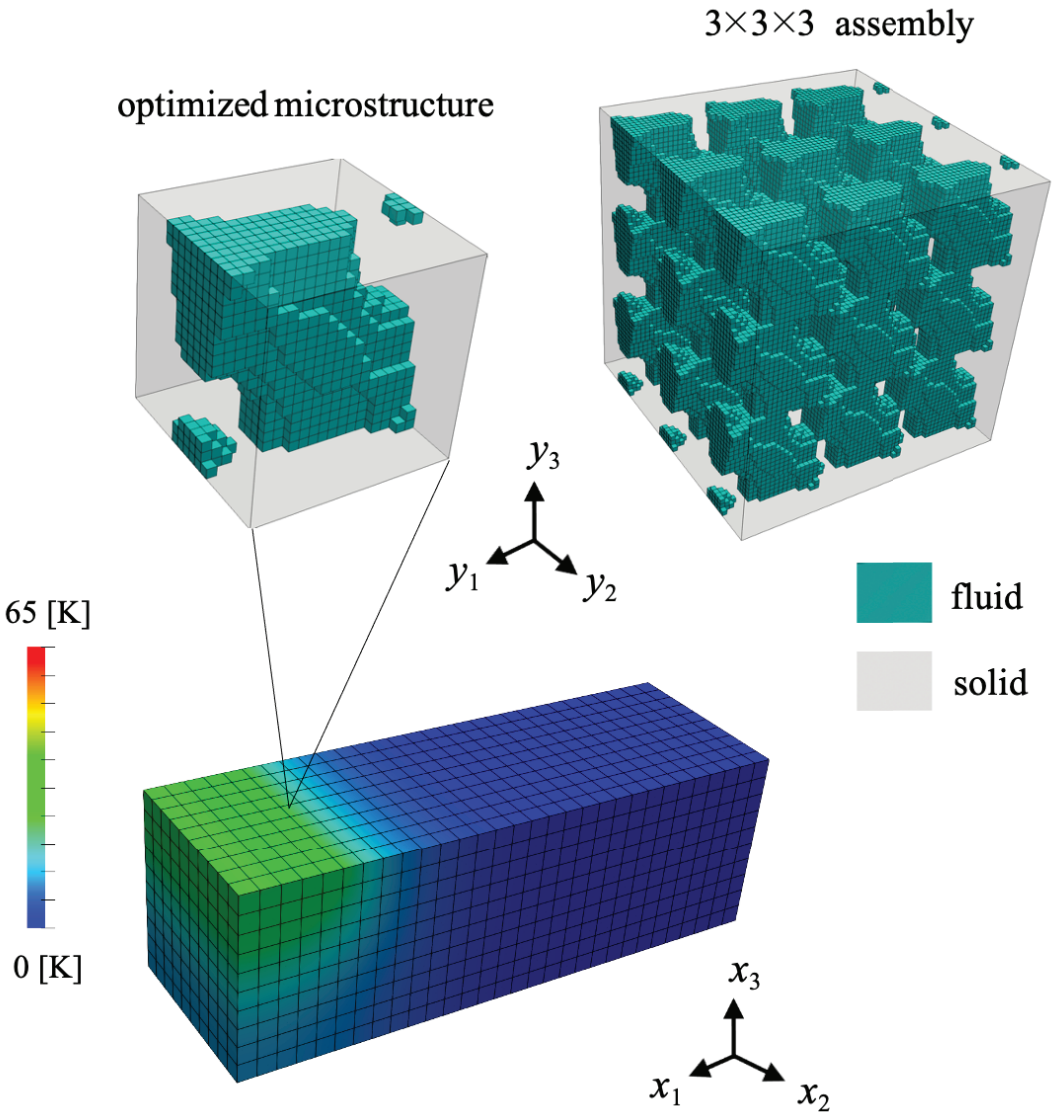

Figure 3.22: Optimization results of beam-like structure for the 0.05 s period of time

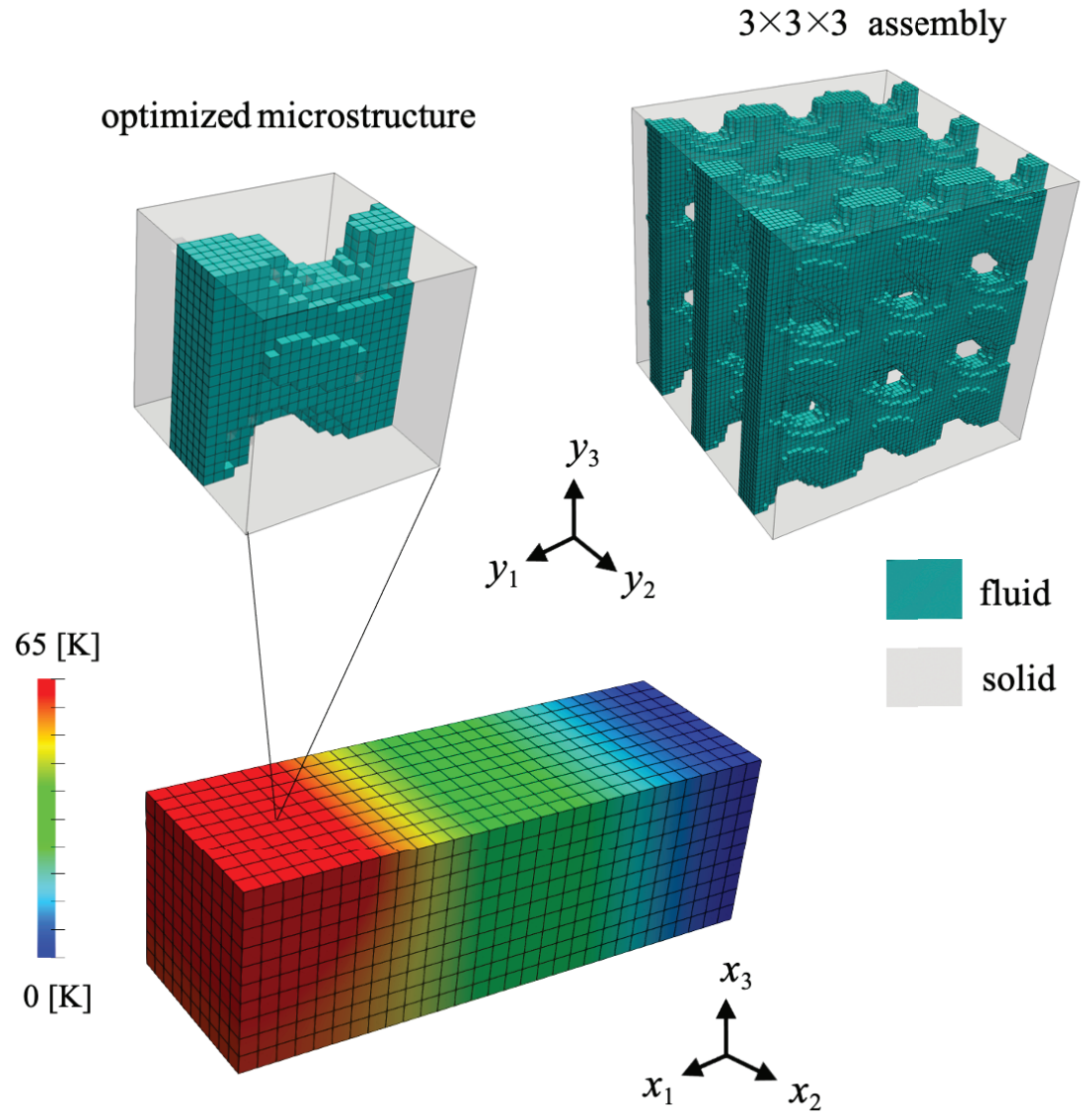

Figure 3.23: Optimization results of beam-like structure for the 0.5 s period of time

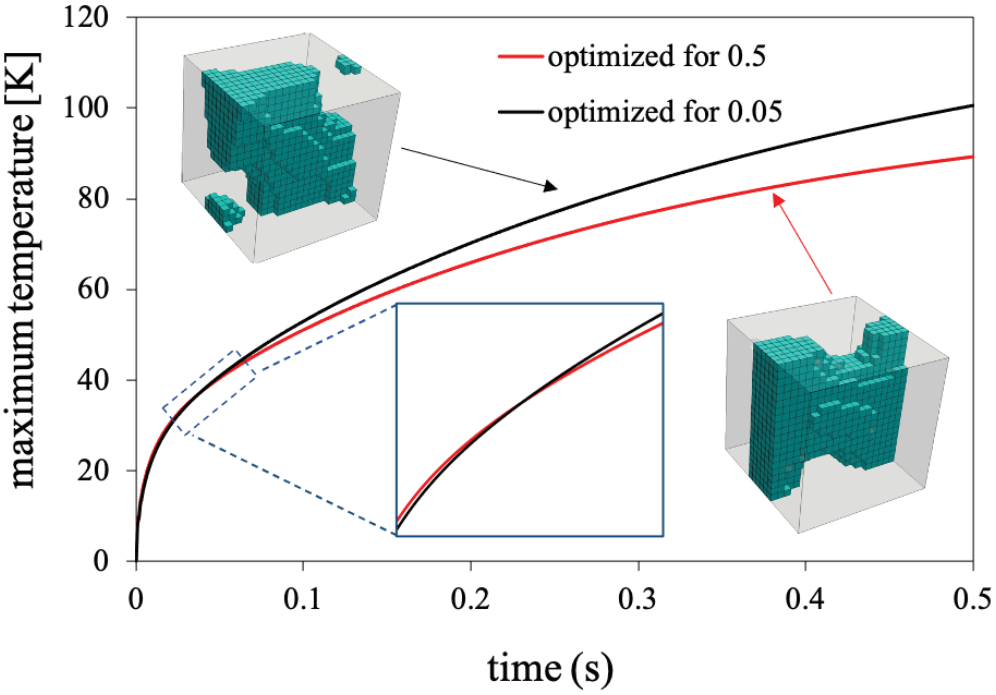

Figure 3.24: Maximum temperature on a beam-like macrostructure for the 0.5 s period of time for the two optimized microstructures

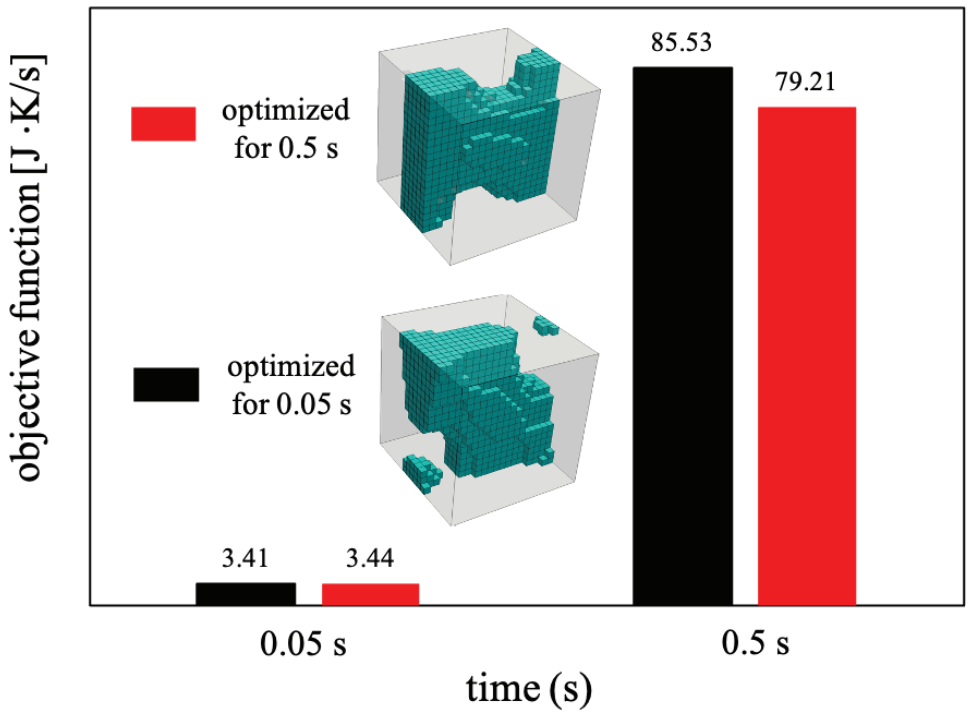

Figure 3.25: Comparison of objective function values for two optimized microstructures for the 0.05 s and 0.5 s periods of time

because the temperature is mainly distributed in the vertical and horizontal directions (x_1x_3-plane), the fluid in the microstructure is formed in accordance with the temperature distribution, similar to that shown in Fig. 3.23. For design domains 2 and 3, the temperature distribution is mainly along the x_1-axis. Thus, the fluid is mainly formed in the x_1-axis like the previous example. However, because design domain 3 is far from the Neumann boundary, the temperature gradient is relatively small. As a result, in design domain 3, the heat transfer term $k_{\mathrm{t}}^{\mathrm{H}}$ strongly affects the layout of the fluid region in the optimized microstructure: this explains the different topologies of design domains 2 and 3.

To investigate in greater detail, the same optimization problem is used with a small enough heat transfer $k_{\mathrm{t}}^{\mathrm{H}}$ that the on-heat transfer condition from fluid to solid is reproduced. Fig. 3.27 illustrates the optimized microstructures for each domain. As can be seen, the optimized microstructures for the design domains 1 and 3 are significantly different from those of Fig. 3.26. Despite the different topologies of Fig. 3.26 and Fig. 3.27, the fluid layout in the optimized microstructures is still generated according to the temperature distribution in the macrostructure in a manner consistent with that discussed earlier. To be specific, in the case of design domain 1, the fluid is mainly formed in the horizontal direction (x_1-axis), and then in the diagonal direction (x_1x_3-plane) while in design domians 2 and 3, the fluid mainly forms in the horizontal direction (x_1-axis). In addition, the design domain 3 shown in Fig. 3.26 has a larger interface area than that of Fig. 3.27 to transfer heat from fluid to solid. This highlights the influence of the heat transfer term $k_{\mathrm{t}}^{\mathrm{H}}$ on the layout of the optimization.

Table 3.2 illustrates the objective function value and maximum temperature for the above cases: (i) a unique microstructure (Fig. 3.23), (ii) 3 microstructures with the heat transfer effect $k_{\mathrm{t}}^{\mathrm{H}}$ (Fig. 3.26) and (iii) with no heat transfer effect $k_{\mathrm{t}}^{\mathrm{H}}$ (Fig. 3.27). As can be seen, case (ii) shows the best performance with the lowest objective function value and maximum temperature, and case (iii) is next, followed by case (i). This suggests that increasing the number of microstructures improves the material design for heat dissipative performance, especially when combined with the heat transfer effect.

Finally, we investigate the influence of the size of the microstructures on the objective function value again using the microstructures of cases (i) and (ii).

Figure 3.28 shows the results obtained from the transient heat analysis with various sizes of the microstructures where the same topologies as case (i) and (ii) are applied. It can be clearly seen that case (ii) exhibits a lower objective function than that of case (i). In addition, the objective function value sharply decreases as the microstructures become smaller. It can be observed that when a microstructure is sufficiently large, the value of the objective function tends to stay at a constant

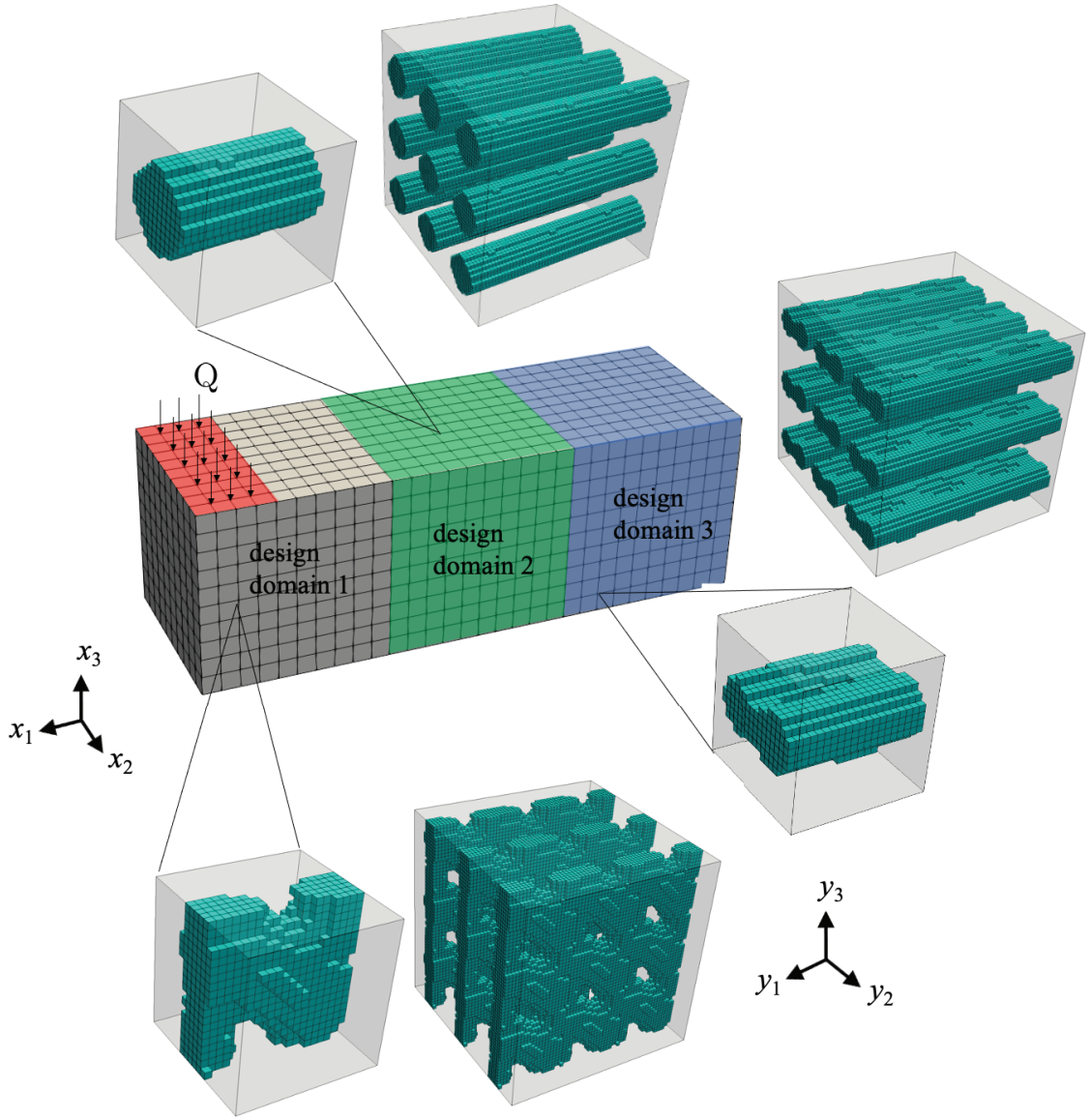

Figure 3.26: Three optimized microstructures for the 0.5 s period of time

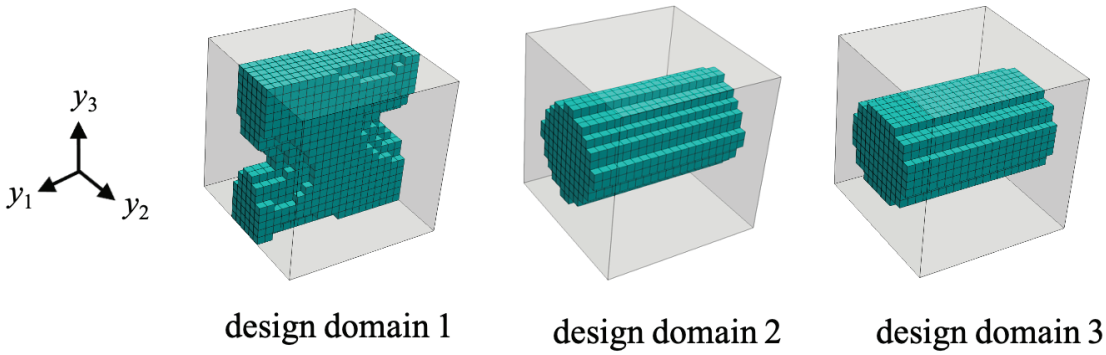

Figure 3.27: Three optimized microstructures for the 0.5 s period of time without the heat transfer effect

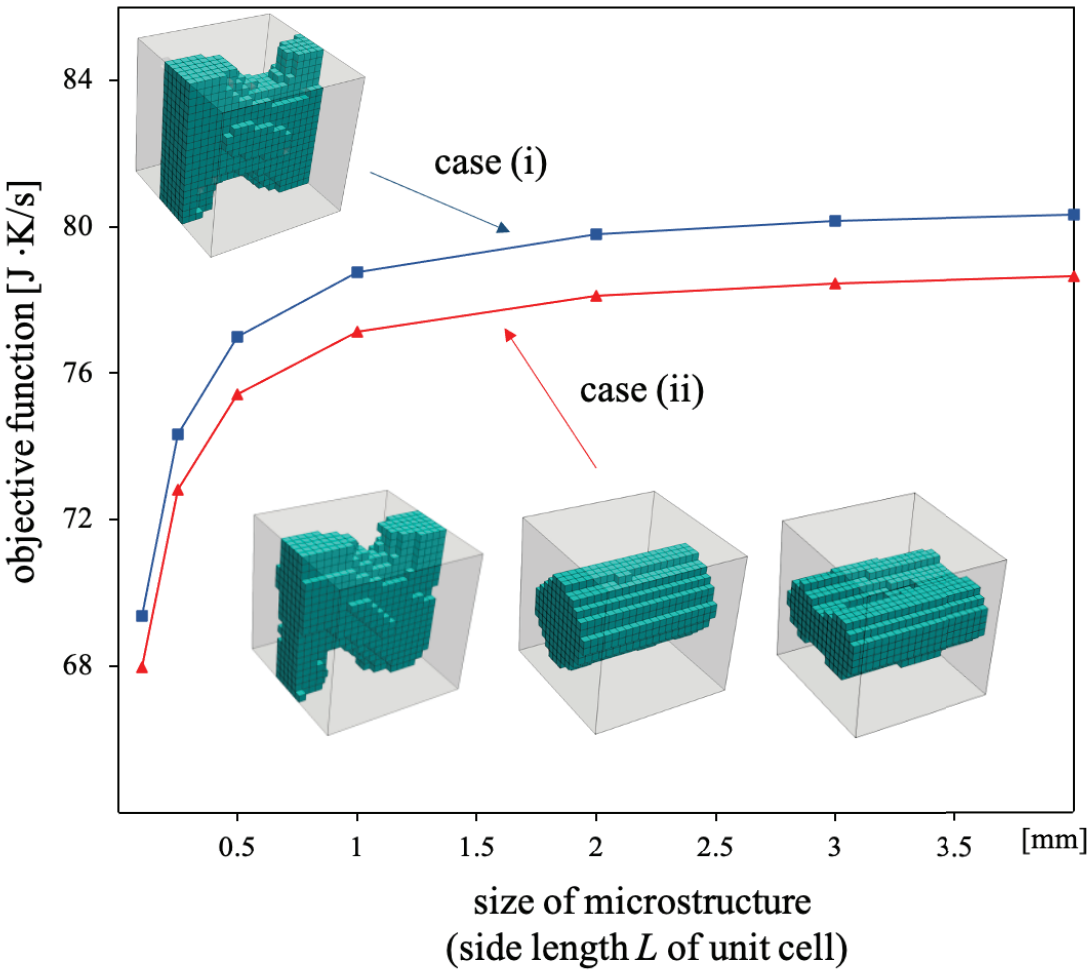

Figure 3.28: Comparison of the objective function and the size of the microstructures in cases (i) and (ii)

Table 3.2: Comparison of single and three design microstructures

	objective function [J ・K/s]	max fluid temp [K]	max solid temp [K]
(i) a unique microstructure	78.8	89.36	5.32
(ii) 3 microstructures with heat transfer effect, $k_{\mathrm{t}}^{\mathrm{H}}$	77.1	86.44	5.27
(iii) 3 microstructures without heat transfer effect, $k_{\mathrm{t}}^{\mathrm{H}}$	78.1	88.74	-

value. This can be attributed to the disappearance of the heat transfer effect from the relation in Eq. (3.6) when the ratio of the interface area to $|Y|$ is small enough. From the manufacturing perspective, this result stresses the importance of specifying the maximum size for which the heat transfer term is still active.

3.4 Summary

A two-scale topology optimization framework for a transient heat analysis in porous material has been successfully developed based on homogenization theory which is capable of considering the size effect of the micro-scale heat transfer. Heat compliance was selected to be an objective function of our framework. To efficiently achieve the optimal result, we employed the analytical adjoint variable formulation for a sensitivity analysis. The results of this analysis were compared to those obtained by the finite difference method to verify the accuracy of the method.

In the first example, a rectangular domain was subjected to three simple loading conditions to confirm the obtained results were reasonable. An excellent convergence to the optimal solution was obtained to show the efficiency and reliability of the proposed method. Then, in the second and third examples, the remarkable transient effect on the optimal microstructure was observed for each target time. Furthermore, it was found that the smaller microstructure size can improve the heat transfer capability while causing an asymmetrical shape of the microstructure. This phenomenon was explained by the size-dependent term, namely the heat transfer coefficient, which can greatly enhance the heat dissipation performance of the structure.

Finally, the proposed method was extended to demonstrate its performance by simultaneously optimizing multiple microstructures. The results showed that the concept of multiple microstructures with the size effect gives the superiority of heat dissipation performance compared to the general two-scale topology optimization with a unique microstructure.

Chapter 4

The development of topology optimization framework for designing micro-and macrostructures

In this chapter, topology optimization framework for designing micro and macrostructures recognized as concurrent topology optimization of multi-scale structures (Deng et al. 2013; Yan et al. 2014; Liu et al. 2016; Wang et al. 2018; Gao et al. 2019; Kato et al. 2018a; Al Ali and Shimoda 2022) is developed by extending the optimization framework proposed in the previous chapter. The optimization model, which consists of micro-level and macro-level optimization problems, is established with the heat compliance objective function and the analytical sensitivity formulations. Finally, two numerical examples are selected to demonstrate the performance of the proposed optimization framework.

4.1 Formulation

Before establishing the optimization framework, let us recall the governing equations (2.8) and (2.9) to redefine material parameters, which is suitable for the development in the later section. The expressions can be rewritten as follows:

$$\boldsymbol{C}_{\mathrm{I}} = \int_{\Omega_{\mathrm{I}}} \boldsymbol{N}^{\mathrm{T}} C_{\mathrm{I}}^{\mathrm{M}} \boldsymbol{N} \, \mathrm{d}\Omega, \tag{4.1}$$

$$\boldsymbol{C}_{\mathrm{II}} = \int_{\Omega_{\mathrm{II}}} \boldsymbol{N}^{\mathrm{T}} C_{\mathrm{II}}^{\mathrm{M}} \boldsymbol{N} \, \mathrm{d}\Omega, \tag{4.2}$$

$$\boldsymbol{K}_{\mathrm{I}} = \int_{\Omega_{\mathrm{I}}} \boldsymbol{B}^{\mathrm{T}} k_{\mathrm{c_I}}^{\mathrm{M}} \boldsymbol{B} \, \mathrm{d}\Omega + \int_{\Omega_{\mathrm{I}}} \boldsymbol{N}^{\mathrm{T}} k_{\mathrm{t}}^{\mathrm{M}} \boldsymbol{N} \, \mathrm{d}\Omega, \tag{4.3}$$

$$\boldsymbol{K}_{\mathrm{II}} = \int_{\Omega_{\mathrm{II}}} \boldsymbol{B}^{\mathrm{T}} k_{\mathrm{c_{II}}}^{\mathrm{M}} \boldsymbol{B} \, \mathrm{d}\Omega + \int_{\Omega_{\mathrm{II}}} \boldsymbol{N}^{\mathrm{T}} k_{\mathrm{t}}^{\mathrm{M}} \boldsymbol{N} \, \mathrm{d}\Omega, \tag{4.4}$$

$$\boldsymbol{F}_{\mathrm{I}} = \int_{\Gamma_{\mathrm{Q}}} \boldsymbol{N}^{\mathrm{T}} Q \, \mathrm{d}\Gamma, \tag{4.5}$$

$$\boldsymbol{F}_{\mathrm{I}} = \int_{\Omega_{\mathrm{II}}} \boldsymbol{N}^{\mathrm{T}} k_{\mathrm{t}}^{\mathrm{M}} \, \hat{\boldsymbol{T}}_{\mathrm{I}} \, \mathrm{d}\Omega, \tag{4.6}$$

where $\boldsymbol{k}_{\mathrm{c}}^{\mathrm{M}}$, C^{M} and $k_{\mathrm{t}}^{\mathrm{M}}$ are macroscopic coefficients of heat conduction, heat capacity and heat transfer, respectively.

4.1.1 Definition of two-scale design variables

Firstly, ϕ_{m} and ϕ_{M} are defined as the elemental continuous design variables at micro and macro levels, respectively. For simplicity, the indices, m and M, on ϕ identify micro- and macro-scale, respectively. The values 0 and 1 can be represented as follow:

$$\phi_{\mathrm{m}} = \begin{cases} 1 & \text{phase I} \\ 0 & \text{phase II} \end{cases}, \tag{4.7}$$

$$\phi_{\mathrm{M}} = \begin{cases} 1 & \text{macro-material} \\ 0 & \text{void} \end{cases}. \tag{4.8}$$

For the intermediate value $0 < \phi_{\mathrm{m}} < 1$ and $0 < \phi_{\mathrm{M}} < 1$, they represent the mixture of the above materials.

4.1.2 Material interpolation

To smoothly update each parameter during the optimization, the well-known interpolation scheme, SIMP, is applied to obtain material parameters for both scales. Firstly, for micro-scale, the effective material parameters can be expressed as

$$c_{\mathrm{I}}^{\mathrm{m}} = \phi_{\mathrm{m}}^{\eta} c_{\mathrm{I}}, \quad c_{\mathrm{II}}^{\mathrm{m}} = (1 - \phi_{\mathrm{m}})^{\eta} c_{\mathrm{II}}, \tag{4.9}$$

$$\rho_{\mathrm{I}}^{\mathrm{m}} = \phi_{\mathrm{m}}^{\eta} \rho_{\mathrm{I}}, \quad \rho_{\mathrm{II}}^{\mathrm{m}} = (1 - \phi_{\mathrm{m}})^{\eta} \rho_{\mathrm{II}}, \tag{4.10}$$

$$k_{\mathrm{c_I}}^{\mathrm{m}} = \phi_{\mathrm{m}}^{\eta} k_{\mathrm{c_I}}, \quad k_{\mathrm{c_{II}}}^{\mathrm{m}} = (1 - \phi_{\mathrm{m}})^{\eta} k_{\mathrm{c_{II}}}, \tag{4.11}$$

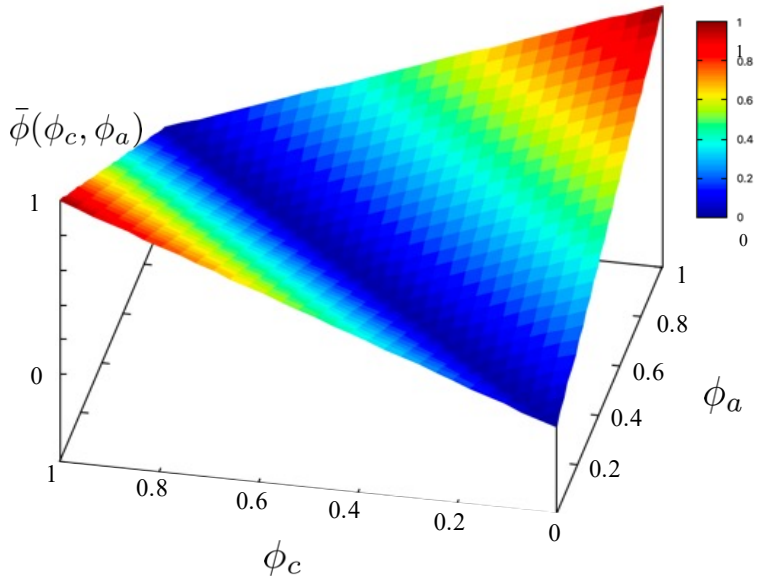

Figure 4.1: The interpolation function for heat transfer in the microstructure

$$k_{\mathrm{t}}^{\mathrm{m}} = \bar{\phi} k_{\mathrm{t}}, \tag{4.12}$$

where c, ρ, $k_{\mathrm{c_I}}$, $k_{\mathrm{c_{II}}}$, and k_{t} are the specific heat coefficient, material density, heat conduction coefficients of phases I and II, and heat transfer coefficient, respectively. η is the power factor and $\eta = 3$ is used in this study. $\bar{\phi}$ is the linear function between the considered (ϕ_c) and adjacent (ϕ_a) design variables in a unit cell as

$$\bar{\phi} = |\phi_c - \phi_a|. \tag{4.13}$$

For macro-level, the effective material parameters can be expressed as

$$C^{\mathrm{M}} = \phi_{\mathrm{M}}^{\eta} C^{\mathrm{H}}, \tag{4.14}$$

$$\boldsymbol{k}_{\mathrm{c}}^{\mathrm{M}} = \phi_{\mathrm{M}}^{\eta} \boldsymbol{k}_{\mathrm{c}}^{\mathrm{H}}, \tag{4.15}$$

$$k_{\mathrm{t}}^{\mathrm{M}} = \phi_{\mathrm{M}}^{\eta} k_{\mathrm{t}}^{\mathrm{H}}. \tag{4.16}$$

4.1.3 Homogenized material coefficients

As shown in Eqs. (4.14)-(4.16), prior to determining C^{M}, $\boldsymbol{k}_{\mathrm{c}}^{\mathrm{M}}$ and $k_{\mathrm{t}}^{\mathrm{M}}$, homogenized material coefficients C^{H}, $\boldsymbol{k}_{\mathrm{c}}^{\mathrm{H}}$ and $k_{\mathrm{t}}^{\mathrm{H}}$ need to be obtained. The formulations can be

expressed with micro-level material parameters as

$$C^{\mathrm{H}} = \frac{1}{|Y|}\int_Y c^{\mathrm{m}}\rho^{\mathrm{m}}\ \mathrm{d}y, \tag{4.17}$$

$$k_{\mathrm{t}}^{\mathrm{H}} = \frac{1}{|Y|}\int_{\partial Y} k_{\mathrm{t}}^{\mathrm{m}}\ \mathrm{d}S, \tag{4.18}$$

$$\boldsymbol{k}_{\mathrm{c}}^{\mathrm{H}} = \frac{1}{|Y|}\int_Y k_{\mathrm{c}}^{\mathrm{m}}(\boldsymbol{I} - \nabla\boldsymbol{\xi})\ \mathrm{d}y. \tag{4.19}$$

As mentioned earlier, to obtain $\boldsymbol{k}_{\mathrm{c}}^{\mathrm{H}}$ in Eq. (4.19), the microscopic response are required. Therefore, as a similar manner to Eqs. (3.8)-(3.10), the formulation which describes the relationship of the characteristic functions can be written as

$$\boldsymbol{H}\boldsymbol{\xi}^j = \boldsymbol{W}, \tag{4.20}$$

$$\boldsymbol{H} = \int_Y \boldsymbol{B}^{\mathrm{T}}\boldsymbol{k}_{\mathrm{c}}^{\mathrm{m}}\boldsymbol{B}\ \mathrm{d}y, \tag{4.21}$$

$$\boldsymbol{W} = \int_{\partial Y} \boldsymbol{B}^{\mathrm{T}}k_{\mathrm{c}}^{\mathrm{m}}\boldsymbol{i}^j\ \mathrm{d}y. \tag{4.22}$$

Referring to Eqs. (3.11) and (3.12), the periodic boundary condition is imposed to microscopic fields on the boundary ∂Y for the interpolation function $\bar{\phi}$ and the characteristic function $\boldsymbol{\xi}$, respectively. These can be written as

$$\bar{\phi}^{[k]} + \bar{\phi}^{[-k]} = 0 \quad \text{on } \partial Y, \tag{4.23}$$

$$\xi^{[k]} + \xi^{[-k]} = 0 \quad \text{on } \partial Y. \tag{4.24}$$

4.1.4 Objective function

In this study, two optimization problems regarding macro and micro design variables are established, respectively. Note that whereas both design variables are coupled in structural and sensitivities analysis, they are updated independently by optimizer. This framework can be recognized as a practical scheme, the so-called decoupling approach, to optimize micro- and macrostructures (Kato et al. 2018a). To formulate optimization problem, macroscopic heat compliance is selected to be the objective function along with the volume constraint, governing equation, and boundary conditions in time integral form as

For macro-scale:

$$\min_{\boldsymbol{\phi}_{\mathrm{M}}} \quad f(\boldsymbol{\phi}_{\mathrm{M}}, \boldsymbol{\phi}_{\mathrm{m}}, t) = \int_0^t \boldsymbol{F}_{\mathrm{I}}^{\mathrm{T}} \boldsymbol{T}_{\mathrm{I}} \, \mathrm{d}t + \int_0^t \boldsymbol{F}_{\mathrm{II}}^{\mathrm{T}} \boldsymbol{T}_{\mathrm{II}} \, \mathrm{d}t, \tag{4.25}$$

$$s.t. \quad g(\boldsymbol{\phi}_{\mathrm{M}}) = \sum_{e=1}^{N_{\mathrm{el}}} V_e(\phi_{\mathrm{M}}) - V_{\mathrm{M}} \leq 0, \tag{4.26}$$

Eqs.(2.8) and (2.9),

$$T(\boldsymbol{x}, 0) = \dot{T}(\boldsymbol{x}, 0) = T_0, \tag{4.27}$$

$$0 \leq \boldsymbol{\phi}_{\mathrm{M}} \leq 1. \tag{4.28}$$

For micro-scale:

$$\min_{\boldsymbol{\phi}_{\mathrm{m}}} \quad f(\boldsymbol{\phi}_{\mathrm{m}}, \boldsymbol{\phi}_{\mathrm{M}}, t) = \int_0^t \boldsymbol{F}_{\mathrm{I}}^{\mathrm{T}} \boldsymbol{T}_{\mathrm{I}} \, \mathrm{d}t + \int_0^t \boldsymbol{F}_{\mathrm{II}}^{\mathrm{T}} \boldsymbol{T}_{\mathrm{II}} \, \mathrm{d}t, \tag{4.29}$$

$$s.t. \quad g(\boldsymbol{\phi}_{\mathrm{m}}) = \sum_{e=1}^{n_{\mathrm{el}}} V_e(\phi_{\mathrm{m}}) - V_{\mathrm{m}} \leq 0, \tag{4.30}$$

Eqs.(2.8) and (2.9),

$$T(\boldsymbol{x}, 0) = \dot{T}(\boldsymbol{x}, 0) = T_0, \tag{4.31}$$

$$0 \leq \boldsymbol{\phi}_{\mathrm{m}} \leq 1. \tag{4.32}$$

where f is the objective function that contains solid and fluid heat compliances during the specific time, and g is a constraint function. N_{el} and n_{el} are the total number of finite elements for macro and microstructures. V_{M} and V_{m} are the volume constraints for macro and microstructures, respectively. Lastly, $\boldsymbol{\phi}_{\mathrm{M}}$ and $\boldsymbol{\phi}_{\mathrm{m}}$ are the vector of design variables for macro and micro levels.

To solve the optimization problem above, MMA optimizer is employed to seek the optimal solution using the two-scale analytical sensitivity formulations. The flow of the optimization process is illustrated in Fig. 4.2

4.1.5 Sensitivity analysis

In order to obtain analytical expression, two adjoint variables $\boldsymbol{\gamma}$ and $\boldsymbol{\lambda}$ are exploited to Eqs. (2.8) and (2.9) again as follows

$$R_{\mathrm{I}} = \int_0^t \boldsymbol{\gamma}^{\mathrm{T}} (\boldsymbol{C}_{\mathrm{I}} \dot{\boldsymbol{T}}_{\mathrm{I}} + \boldsymbol{K}_{\mathrm{I}} \boldsymbol{T}_{\mathrm{I}} - \boldsymbol{F}_{\mathrm{I}}) \, \mathrm{d}t, \tag{4.33}$$

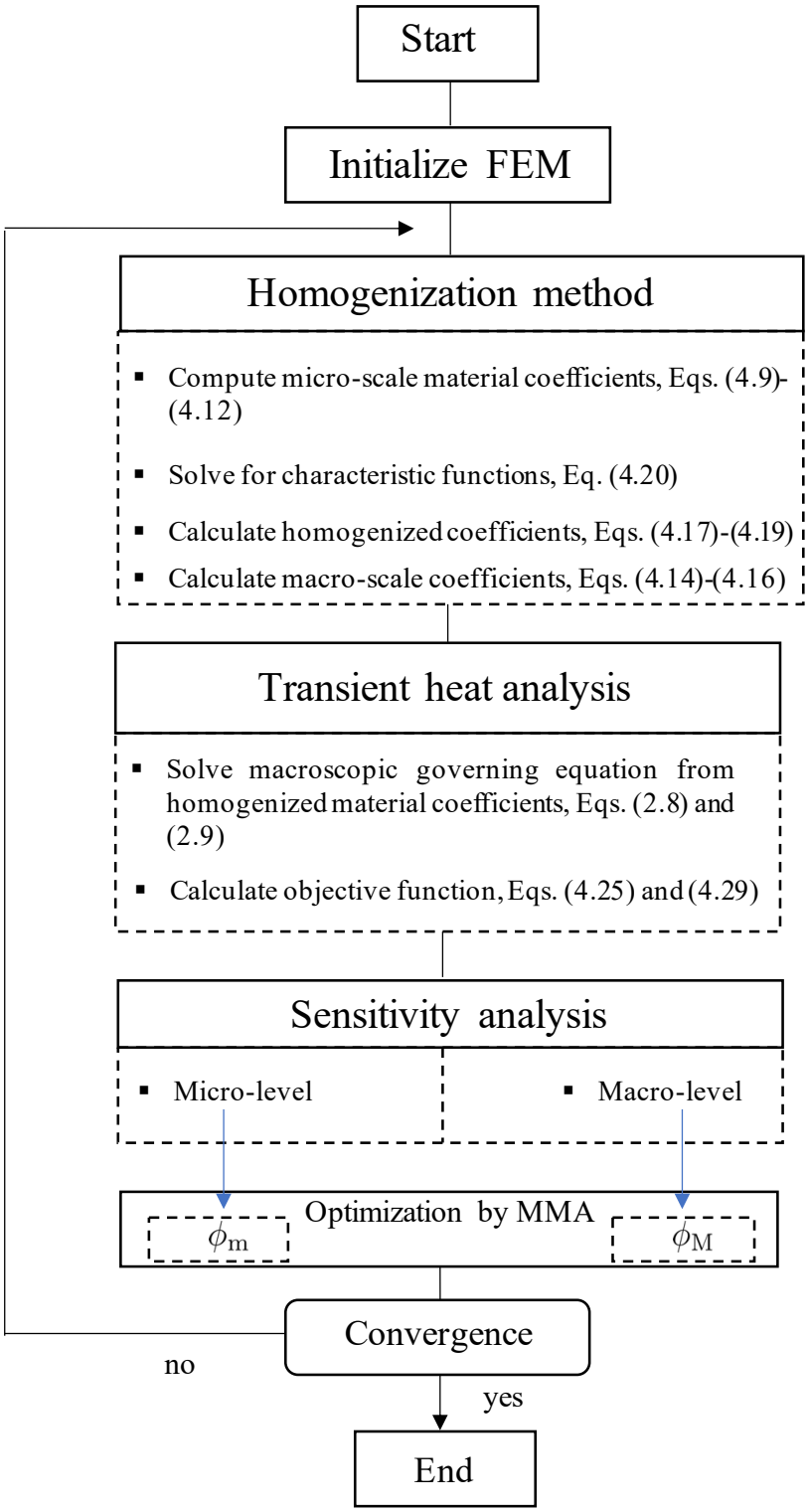

Figure 4.2: The optimization process of proposed concurrent two-scale topology optimization

$$R_{\mathrm{II}} = \int_0^t \boldsymbol{\lambda}^{\mathrm{T}}(\mathbf{C}_{\mathrm{II}}\dot{\boldsymbol{T}}_{\mathrm{II}} + \boldsymbol{K}_{\mathrm{II}}\boldsymbol{T}_{\mathrm{II}} - \boldsymbol{F}_{\mathrm{II}})\ \mathrm{d}t. \tag{4.34}$$

Also, the alternative form of objective function $\tilde{f}$ is introduced as

$$\tilde{f} = f - R_{\mathrm{I}} - R_{\mathrm{II}}. \tag{4.35}$$

Note that R_{I} and R_{II} are disappeared when Eqs. (2.8) and (2.9) are in equilibrium state, therefore, the alternative form $\tilde{f}$ is nothing but the original objective function f. Then, taking the derivative with respect to the design variable yields

$$\frac{\partial \tilde{f}}{\partial \phi_i} = \frac{\partial f}{\partial \phi_i} - \frac{\partial R_{\mathrm{I}}}{\partial \phi_i} - \frac{\partial R_{\mathrm{II}}}{\partial \phi_i}, \tag{4.36}$$

where ϕ_i is the general expression of the design variable which can be either ϕ_{M} or ϕ_{m}. However, the derivation method similar to that adopted in the previous chapter can be applied here to obtain the analytical expression. Finally, we can write the formulation as

$$\begin{aligned}\frac{\partial \tilde{f}}{\partial \phi_i} = &\int_0^t -\boldsymbol{\gamma}^{\mathrm{T}}(\frac{\partial \boldsymbol{C}_{\mathrm{I}}}{\partial \phi_i}\dot{\boldsymbol{T}}_{\mathrm{I}} + \frac{\partial \boldsymbol{K}_{\mathrm{I}}}{\partial \phi_i}\boldsymbol{T}_{\mathrm{I}})\ \mathrm{d}t + \int_0^t -\boldsymbol{\lambda}^{\mathrm{T}}(\frac{\partial \boldsymbol{C}_{\mathrm{II}}}{\partial \phi_i}\dot{\boldsymbol{T}}_{\mathrm{II}} + \frac{\partial \boldsymbol{K}_{\mathrm{II}}}{\partial \phi_i}\boldsymbol{T}_{\mathrm{II}})\ \mathrm{d}t \\ &+ \int_0^t (\boldsymbol{T}_{\mathrm{I}}^{\mathrm{T}}\frac{\partial \boldsymbol{K}_{\mathrm{t}}}{\partial \phi_i}\boldsymbol{T}_{\mathrm{II}} + \boldsymbol{\lambda}^{\mathrm{T}}\frac{\partial \boldsymbol{K}_{\mathrm{t}}}{\partial \phi_i}\boldsymbol{T}_{\mathrm{I}})\ \mathrm{d}t.\end{aligned} \tag{4.37}$$

Also, the adjoint variable equations for obtaining $\boldsymbol{\gamma}$ and $\boldsymbol{\lambda}$ can be formulated as

$$\boldsymbol{F}_{\mathrm{I}}^{\mathrm{T}} + \dot{\boldsymbol{\gamma}}^{\mathrm{T}}\boldsymbol{C}_{\mathrm{I}} - \boldsymbol{\gamma}^{\mathrm{T}}\boldsymbol{K}_{\mathrm{I}} + (\boldsymbol{T}_{\mathrm{II}}^{\mathrm{T}} + \boldsymbol{\lambda}^{\mathrm{T}})\boldsymbol{K}_{\mathrm{t}} = 0, \tag{4.38}$$

$$\dot{\boldsymbol{\lambda}}^{\mathrm{T}}\boldsymbol{C}_{\mathrm{II}} - \boldsymbol{\lambda}^{\mathrm{T}}\boldsymbol{K}_{\mathrm{II}} + \boldsymbol{T}_{\mathrm{I}}^{\mathrm{T}}\boldsymbol{K}_{\mathrm{t}} = 0. \tag{4.39}$$

$$\boldsymbol{\lambda}(t_{\mathrm{f}}) = 0 \text{ and } \boldsymbol{\gamma}(t_{\mathrm{f}}) = 0, \tag{4.40}$$

where t_{f} denotes the final time step. Note that the adjoint variable $\boldsymbol{\lambda}$ in Eq. (4.39) is solved first and then Eq. (4.38), respectively. It can be seen that the sensitivity formulation in Eq. (4.37) depends on whether ϕ_i is ϕ_{M} or ϕ_{m}; however, the derivatives with respect to ϕ_{M} or ϕ_{m} are identical because it uses a same strategy to eliminate the derivatives of implicit terms $\partial \boldsymbol{T}/\partial \phi_{\mathrm{m}}$ and $\partial \boldsymbol{T}/\partial \phi_{\mathrm{M}}$. In other words, the adjoint variables $\boldsymbol{\lambda}$ and $\boldsymbol{\gamma}$ are solved only once for implementation in micro and macro sensitivity analyses.

4.1.6 Derivative of macro-and micro- material parameters

As shown in Eq. (4.37), it requires evaluating the derivative of each stiffness matrix. Firstly, consider heat capacity term $\boldsymbol{C}$ as follows:

$$\frac{\partial \boldsymbol{C}}{\partial \phi_i} = \int_\Omega \boldsymbol{N}^{\mathrm{T}} \frac{\partial C^{\mathrm{M}}}{\partial \phi_i} \boldsymbol{N} \, \mathrm{d}\Omega, \tag{4.41}$$

Also, stiffness $\boldsymbol{K}$ can be decomposed into heat conduction $\boldsymbol{K}_{\mathrm{c}}$ and heat transfer $\boldsymbol{K}_{\mathrm{t}}$ as presented in Eq. (4.3) and Eq. (4.4), thus it can be expressed as

$$\frac{\partial \boldsymbol{K}}{\partial \phi_i} = \frac{\partial \boldsymbol{K}_{\mathrm{c}}}{\partial \phi_i} + \frac{\partial \boldsymbol{K}_{\mathrm{t}}}{\partial \phi_i}, \tag{4.42}$$

where

$$\frac{\partial \boldsymbol{K}_{\mathrm{c}}}{\partial \phi_i} = \int_\Omega \boldsymbol{B}^{\mathrm{T}} \frac{\partial \boldsymbol{k}_{\mathrm{c}}^{\mathrm{M}}}{\partial \phi_i} \boldsymbol{B} \, \mathrm{d}\Omega, \tag{4.43}$$

$$\frac{\partial \boldsymbol{K}_{\mathrm{t}}}{\partial \phi_i} = \int_{\Omega_{\mathrm{s}}} \boldsymbol{N}^{\mathrm{T}} \frac{\partial k_{\mathrm{t}}^{\mathrm{M}}}{\partial \phi_i} \boldsymbol{N} \, \mathrm{d}\Omega. \tag{4.44}$$

Next, the derivative of Eq. (4.14) and Eq. (4.16) with respect to macro-level design variable can be formulated as

$$\frac{\partial C^{\mathrm{M}}}{\partial \phi_{\mathrm{M}}} = \eta \phi_{\mathrm{M}}^{\eta-1} \, C^{\mathrm{H}}, \tag{4.45}$$

$$\frac{\partial \boldsymbol{k}_{\mathrm{c}}^{\mathrm{M}}}{\partial \phi_{\mathrm{M}}} = \eta \phi_{\mathrm{M}}^{\eta-1} \, \boldsymbol{k}_{\mathrm{c}}^{\mathrm{H}}, \tag{4.46}$$

$$\frac{\partial k_{\mathrm{t}}^{\mathrm{M}}}{\partial \phi_{\mathrm{M}}} = \eta \phi_{\mathrm{M}}^{\eta-1} \, k_{\mathrm{t}}^{\mathrm{H}}. \tag{4.47}$$

Similarly, the derivatives with respect to micro-level design variable can be taken.

$$\begin{aligned} \frac{\partial C^{\mathrm{M}}}{\partial \phi_{\mathrm{m}}} &= \phi_{\mathrm{M}}^{\eta} \, \frac{\partial C^{\mathrm{H}}}{\partial \phi_{\mathrm{m}}} \\ &= \frac{\phi_{\mathrm{M}}^{\eta}}{|Y|} \int_Y 2 \, \eta \phi_{\mathrm{m}}^{2\eta-1} c^{\mathrm{m}} \, \rho^{\mathrm{m}} \, \mathrm{d}y, \end{aligned} \tag{4.48}$$

$$\begin{aligned} \frac{\partial k_{\mathrm{t}}^{\mathrm{M}}}{\partial \phi_{\mathrm{m}}} &= \phi_{\mathrm{M}}^{\eta} \, \frac{\partial k_{\mathrm{t}}^{\mathrm{H}}}{\partial \phi_{\mathrm{m}}} \\ &= \frac{\phi_{\mathrm{M}}^{\eta}}{|Y|} \int_{\partial \Omega_{\mathrm{int}}} \frac{\partial \bar{\phi}}{\partial \phi_{\mathrm{m}}} k_{\mathrm{t}}^{\mathrm{m}} \, \mathrm{d}S, \end{aligned} \tag{4.49}$$

Table 4.1: Material properties

	Air (fluid)	Aluminum Alloy (solid)
specific heat [J/(kg K)], c	1006.43	900
density [kg/m^3], ρ	1.226	2700
heat conduction [W/(m K)], k_c	0.026	200
heat transfer [W/(mm^2 K)], k_t	-	1×10^{-6}

where

$$\frac{\partial\bar{\phi}}{\partial\phi_\mathrm{m}} = \begin{cases} -1 & \text{if } \phi_c < \phi_a \\ 0 & \text{if } \phi_c = \phi_a \\ 1 & \text{if } \phi_c > \phi_a \end{cases}.$$

In contrast to Eqs. (4.48) and (4.49), it is not straightforward to obtain the derivative formulation for heat conduction $\partial\boldsymbol{k}_\mathrm{c}^\mathrm{M}/\partial\phi_\mathrm{m}$ because it includes the implicit derivative term $\partial\boldsymbol{\xi}/\partial\phi_\mathrm{m}$. Therefore, the adjoint method is adopted to eliminate this term, similar to that presented in Zhou and Li (2008). Finally, the formulation can be written as

$$\begin{aligned}\frac{\partial\boldsymbol{k}_\mathrm{c}^\mathrm{M}}{\partial\phi_\mathrm{m}} &= \phi_\mathrm{M}^\eta\,\frac{\partial\boldsymbol{k}_\mathrm{c}^\mathrm{H}}{\partial\phi_\mathrm{m}} \\ &= \frac{\phi_\mathrm{M}^\eta}{|Y|}\int_Y (\boldsymbol{I}-\nabla\boldsymbol{\xi})\;\eta\;\phi_\mathrm{m}^{\eta-1}k_\mathrm{c}^\mathrm{m}(\boldsymbol{I}-\nabla\boldsymbol{\xi})\;\mathrm{d}y. \end{aligned} \tag{4.50}$$

To avoid numerical instability, we use the same sensitivity filtering as Eq. (3.38). The filter radius is set to 4 times the element size of the microstructure as well as the previous chapter. However, the optimized macrostructure shows excellent convergent in our study; thus, we do not apply the filter to the macrostructure at this stage to investigate actual behaviors.

4.2 Numerical Results

In this section, the developed design framework is applied to the porous material, consisting of a solid phase as the higher conductivity (phase I) and a fluid phase as the lower one (phase II). Remark that it is different from the previous chapter to show the broad application of the developed optimization framework. In fact, the material properties used in these numerical examples are adopted from the practices available for additive manufacturing. The details of material properties used in this study (Takarazawa et al. 2022) are presented in Table 4.1. In addition, the initial condition of all design variables for the macrostructure is setting the same value in

the entire domain, and for the microstructure is the same as in the previous chapter by using excitation.

4.2.1 Example 1: a plate-like structure subject to heat flux at center

In the first example, the rectangular macrostructure is adopted as illustrated in Fig. 4.3, where heat flux $Q = 0.5$ W/mm^2 is applied at the center of top surface along with the temperature constraint $T = 0$ K at the four edges. Also, the macrostructure is discretized with $20 \times 20 \times 4$ eight-node hexahedral elements, and the macroscopic volume is constrained to be less than 40% of total volume.

For the microstructure, the size L is set to 0.1 mm along with the discretization of $20 \times 20 \times 20$ eight-node hexahedral elements. The microscopic solid volume is set to less than 50% in proportion to the microstructure volume.

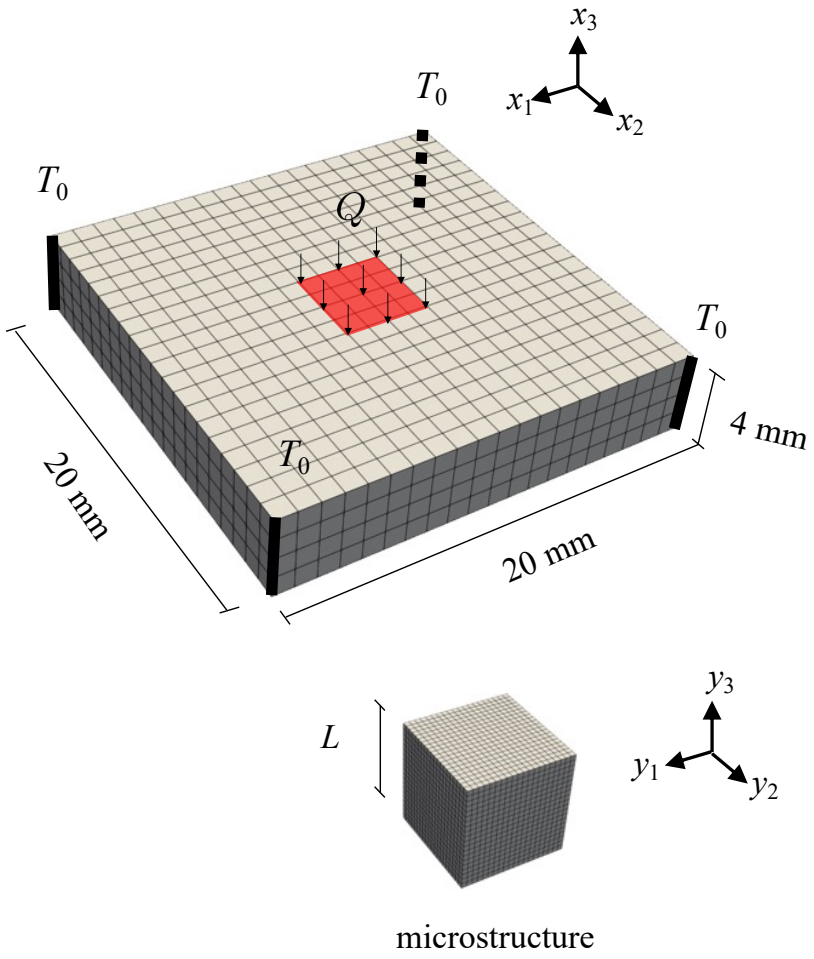

Figure 4.3: A plate-like macrostructure under single heat flux and its microstructure

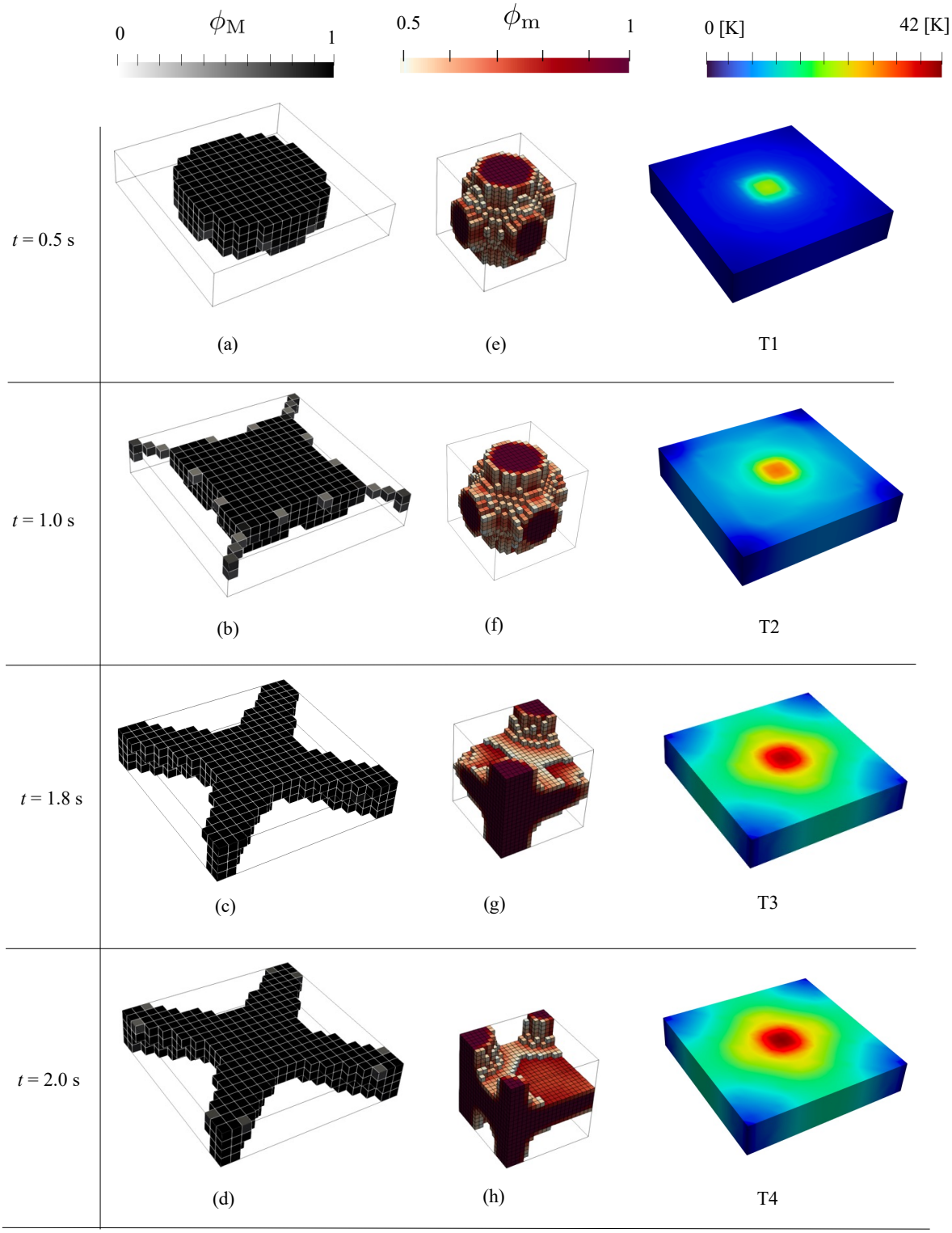

Figure 4.4: The optimization results at each target time of plate-like macrostructures under single heat flux

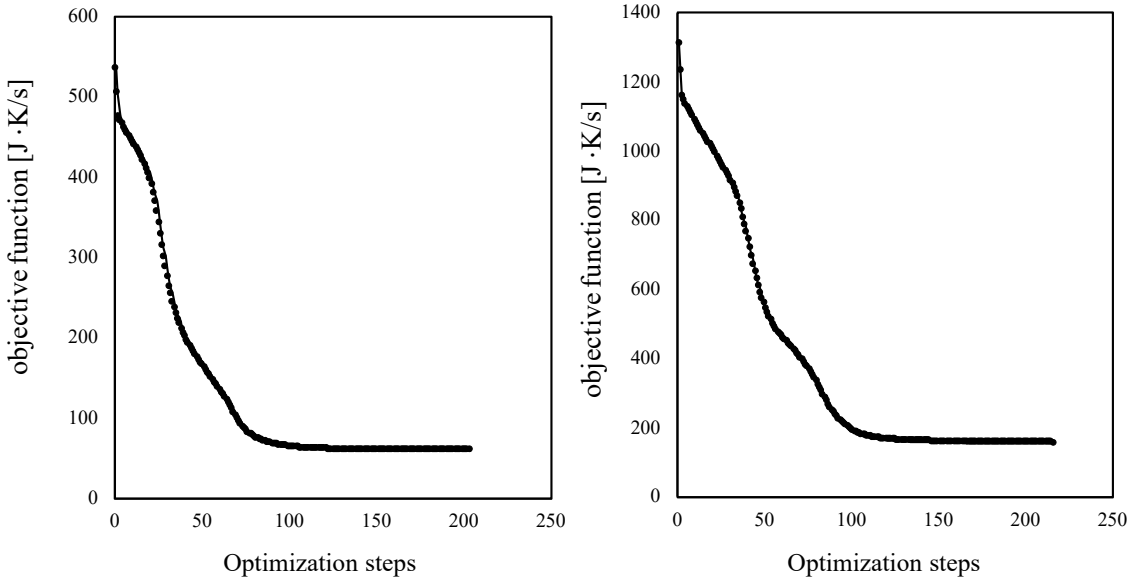

(a) $t = 0.5$ s

(b) $t = 1.0$ s

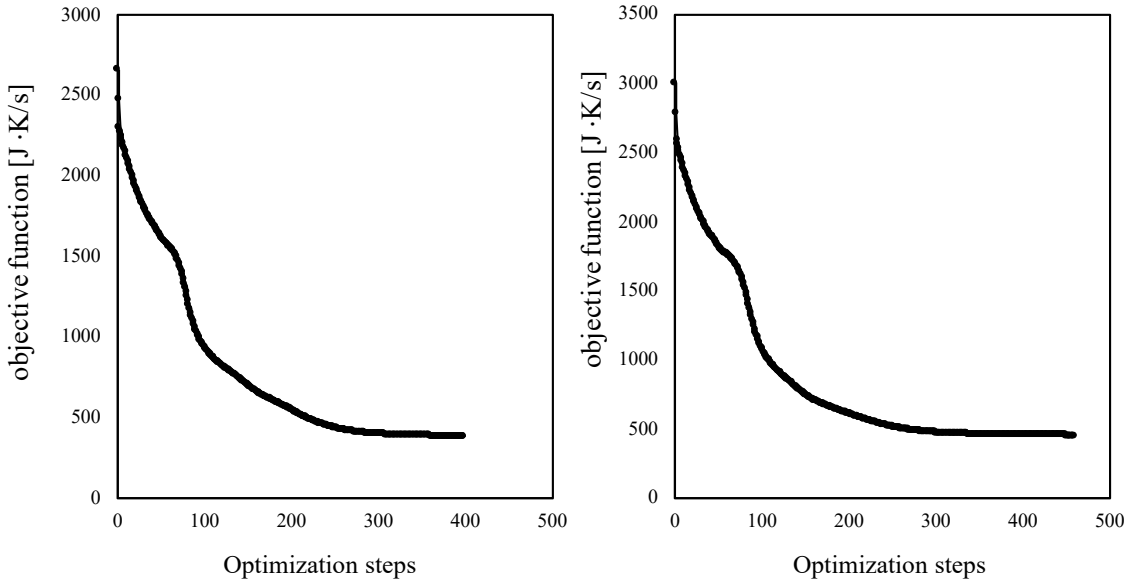

(c) $t = 1.8$ s

(d) $t = 2.0$ s

Figure 4.5: History of objective function values at different target times

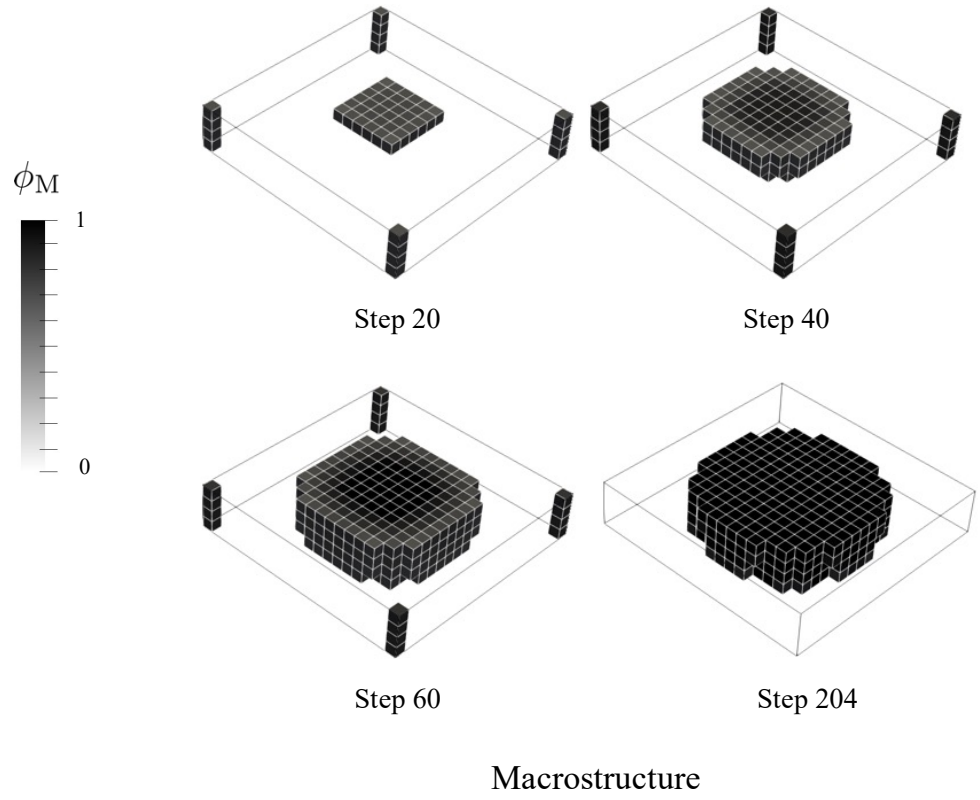

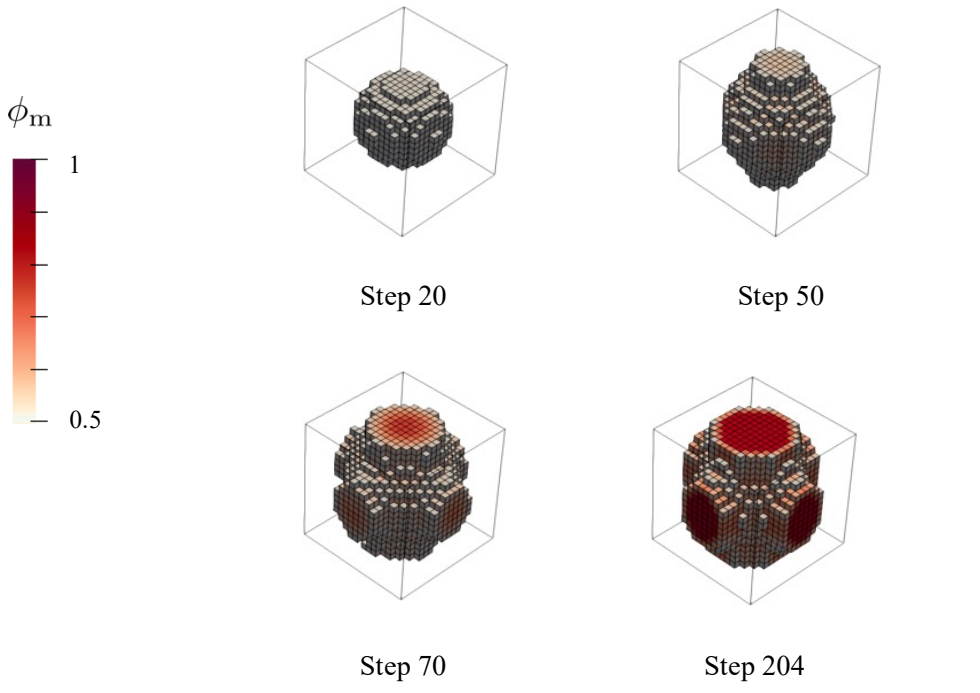

Figure 4.6: History of optimal topologies for macro-and microstructures at $t = 0.5$ s

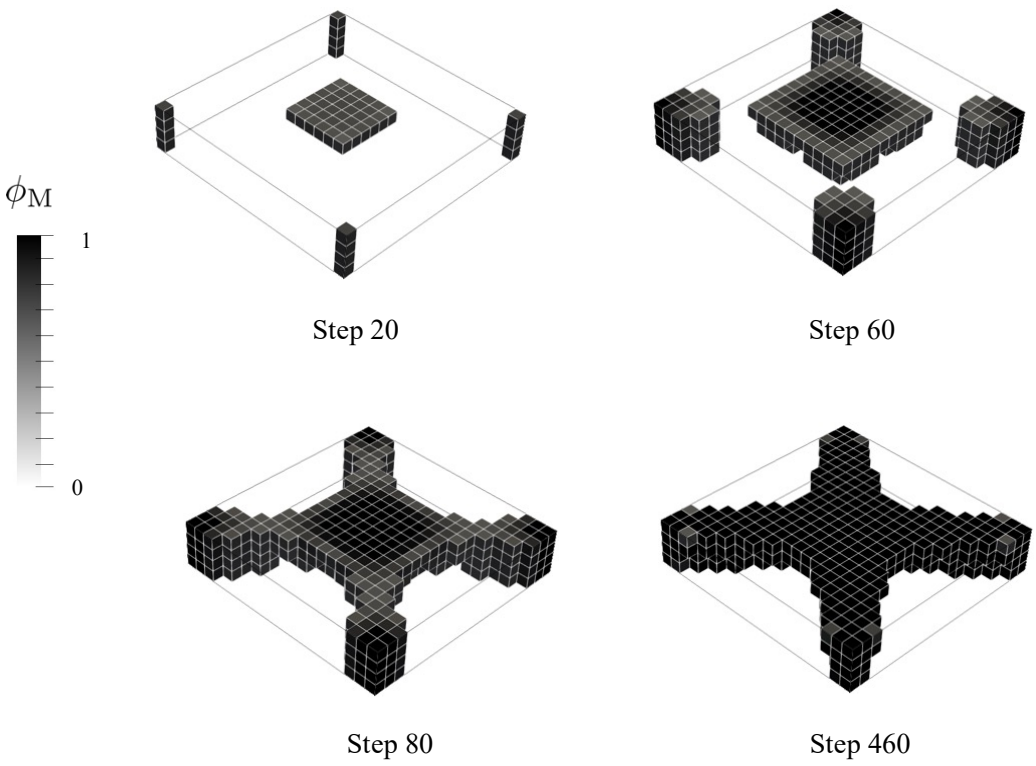

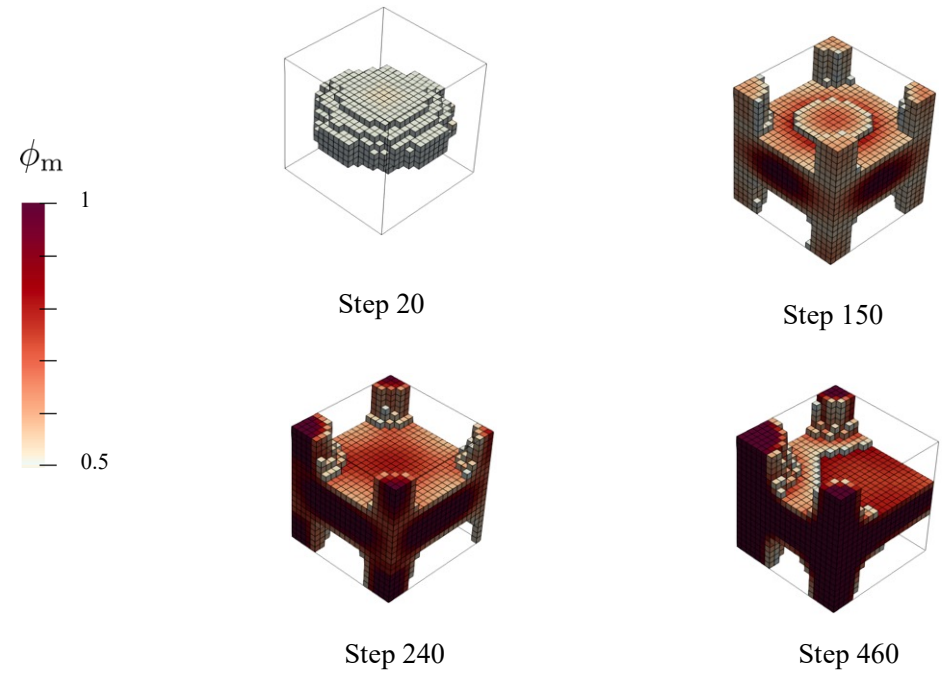

Figure 4.7: History of optimal topologies for macro-and microstructures at $t = 2.0$ s

Firstly, to investigate the transient effect, we carry out the two-scale optimization with different values of the target time: $t = 0.5$ s, 1.0 s, 1.8 s, and 2.0 s considering the situation from unsteady to steady-state conditions. The optimized macro- and microstructures, together with the temperature distribution of solid phase, are shown in Fig. 4.4. Note that the temperature in the fluid phase is relatively small, so we omit to show it in this example. As shown in Figs. 4.4(a)-(d), the optimized macrostructures are significantly different depending on the considered target time. In more detail, when the target time $t = 0.5$ s, the optimal macrostructure is initially placed at the center of the top surface, and then a topology is formed similar to a rectangular structure from top to bottom (see Fig. 4.4(a)). It can be understood that the temperature distribution is dominant along x_3-axis. Therefore, the distribution path directly from top to bottom (along x_3-axis) is efficient for dissipating the temperature. Next, when the longer target time is applied, the temperature can now be distributed to the boundary in x_1x_2-plane as shown in Figs. 4.4(b)-(d). Regarding this conducting path, the optimal macrostructures are formed and expanded to the boundary constraints at four edges. This tendency is well-known as the X-type high conductivity path reported in topology optimization for steady-state heat conduction (Wu et al. 2021; Zhao et al. 2021). Meanwhile, the time condition also affects the optimized microstructures. Firstly, Fig. 4.4(h) shows the optimized microstructure for the steady-state condition ($t = 2.0$ s). It can be seen that the optimized topology of the solid phase is mainly formed in y_1y_2-plane along with the reinforcement placed in y_3-axis as shown in Fig. 4.4(h). Then, when the target time is reduced, the y_3 component becomes stronger and the solid phase is increasingly formed along the vertical axis. When the target time is set to the unsteady-state, the optimal solid phase structure is generated (Fig. 4.4(e)) parallel to the principal axis (y_1, y_2, and y_3). Fig. 4.5 shows the objective function histories for $t = 0.5$ s and $t = 2.0$ s, respectively. As can be seen, the results are monotonically converged to the optimal local values and can be confirmed the reliability of the proposed scheme. In addition, Figs. 4.6 and 4.7 illustrate the history of optimized topologies for both macro-and microstructures at $t = 0.5$ s and $t = 2.0$ s, respectively. Here, it can be seen that the temperature distribution in the macrostructure also relates to the optimal microstructure. Thus, the temperature distribution path at each specific target time significantly affects the optimization results. In other words, it can be said that the transient effect is essential for the design problem of heat conduction for both macro-and microstructures.

In addition, we notice that topologies of the optimized microstructures in a long period of target time are asymmetric (see Fig. 4.4(h)). This is the cause of introducing the microscopic heat transfer effect as the size-dependent term presented in Eq. (4.18). To investigate more in detail, we carry out the additional analysis with

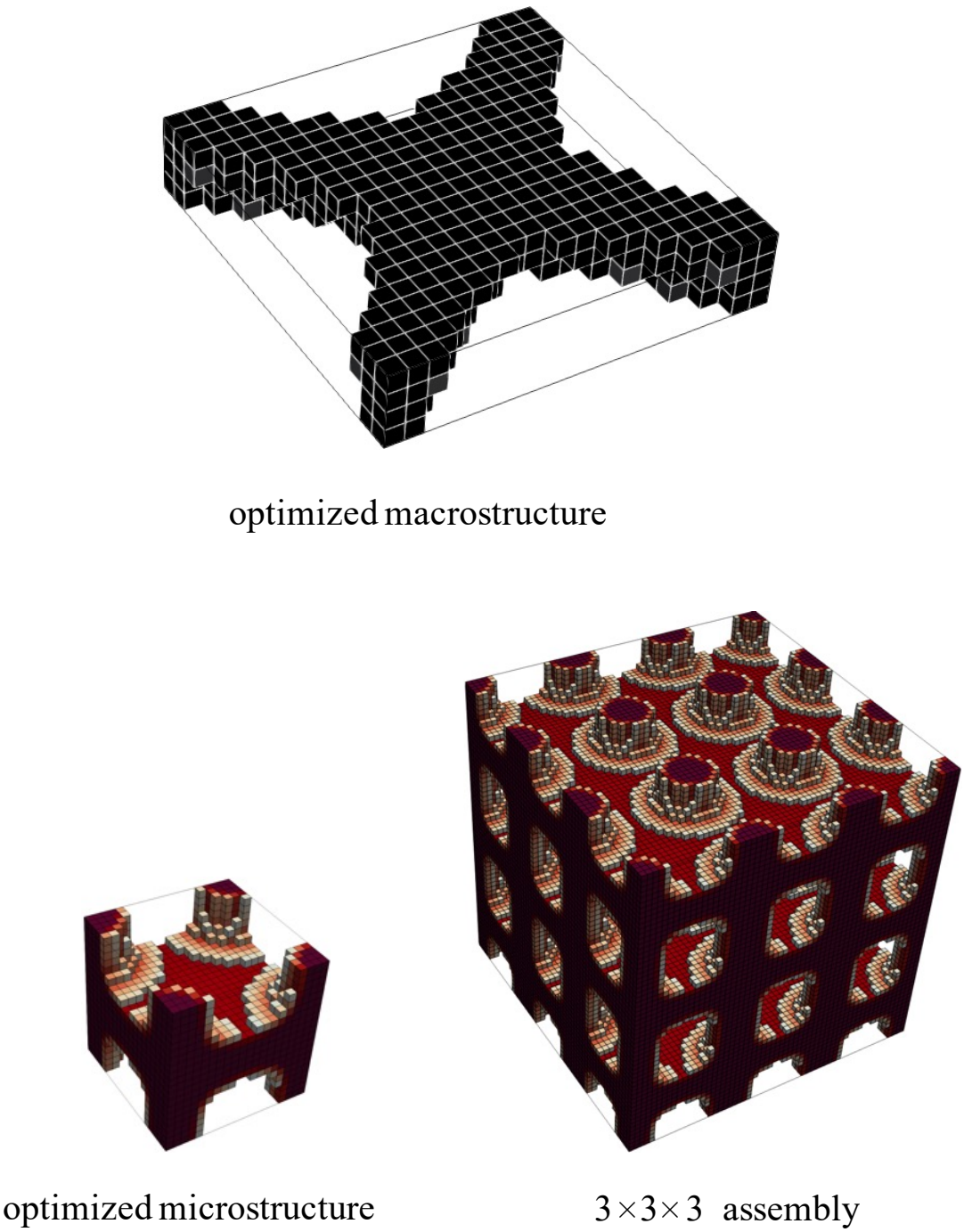

Figure 4.8: The result of optimization with an artificially large microstructure to eliminate the effect of microscopic heat transfer: a symmetric microstructure is obtained

the same conditions as Fig. 4.4(h) except for the microstructure size L (200mm). This size is, of course, extremely large for microstructure, but is chosen to artificially eliminate the effect of microscopic heat transfer. As can be seen in Fig. 4.8, the obtained result shows the symmetric microstructure. This tendency can often be seen when we consider only heat conduction in multi-scale topology optimization (Zhou and Li, 2008; Jia et al. 2018). This investigation led us to understand that, by introducing the microscopic heat transfer effect, the surface area between solid

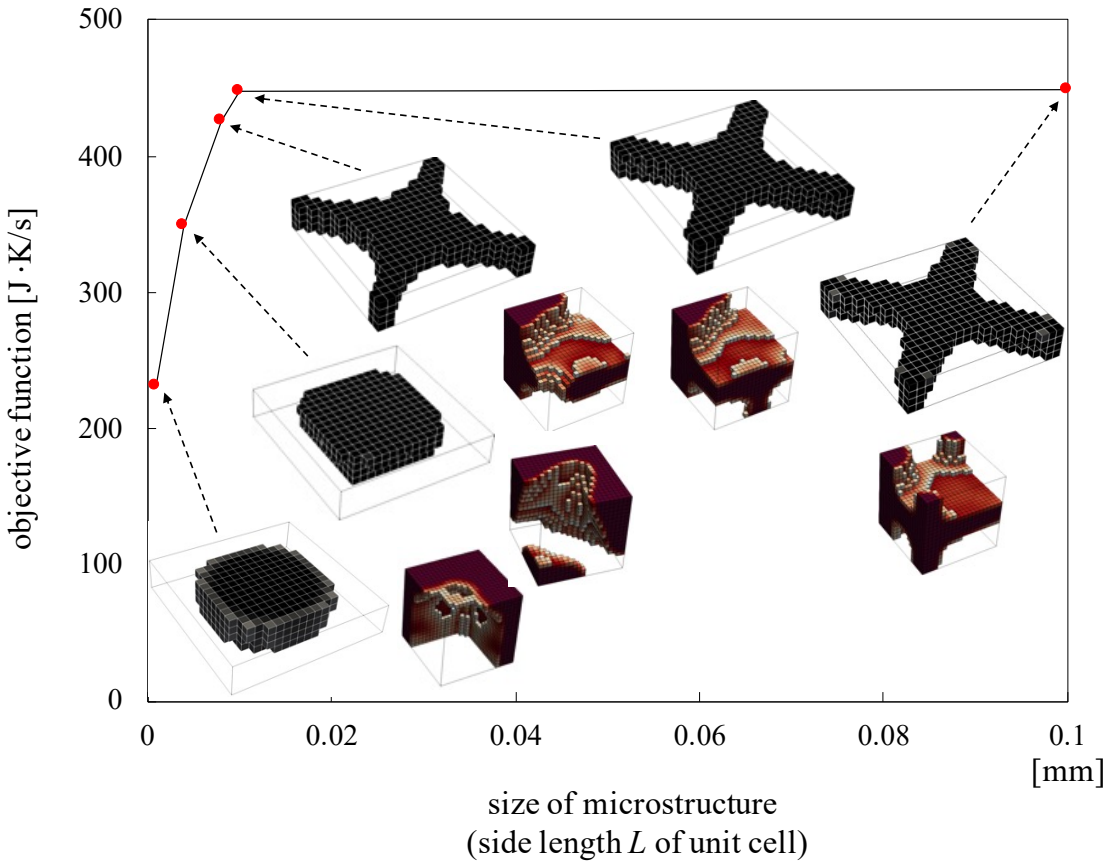

Figure 4.9: Investigation of microstructure size on optimization results of Figs. 4(d) and (h)

and fluid is also included to maximize heat dissipation as presented in Eq. (4.18). When the microstructure size is reduced until the microscopic heat transfer effect is more dominant than heat conduction, the complicated topology with a high surface area can be obtained. This is evident to emphasize the influence on asymmetric shape due to the size-dependent effect.

Furthermore, with the same analysis conditions, we conduct a parametric study on the size of microstructure. The objective function is plotted against the side length of microstructure (L) as shown in Fig. 4.9. As we can see, the objective function decreases when the side length L becomes small. This tendency seems reasonable according to the expression in Eq. (4.18): the heat transfer effect is stronger when microstructure size is reduced (Terada et al. 2010). Consequently, the cumulative heat in the structure can be more dissipated to reduce the objective function value. In addition, it can be seen that the optimized microstructure topologies become asymmetric and complicated when the microstructure size is small. This is because the surface area is also one of the design parameters that appear in Eq. (4.18) and is indirectly designed during the optimization. Finally, we pay attention to the

optimized macrostructure topologies. It can be seen that reduced side length L gradually changes the X-type structure to a central block-shape structure which is similar topology as the unsteady-state problem shown in Fig. 4.4(a). This is understandable regarding the reason that when the microstructure size is small, heat transfer performance is increased so that the heat condition of designed structure does not reach the steady state. This finding is highlighted for the size-dependent feature.

4.2.2 Example 2: a plate-like structure subject to four heat fluxes

Next, let us consider a plate-like structure similar to the previous example but has four heat fluxes applied as shown in Fig. 4.10. In addition, the macroscopic volume is set not to exceed 30%, and the microscopic solid volume is supposed to be less than 80%.

It can be seen that the optimal topologies of macrostructure at $t = 1.0$ s are

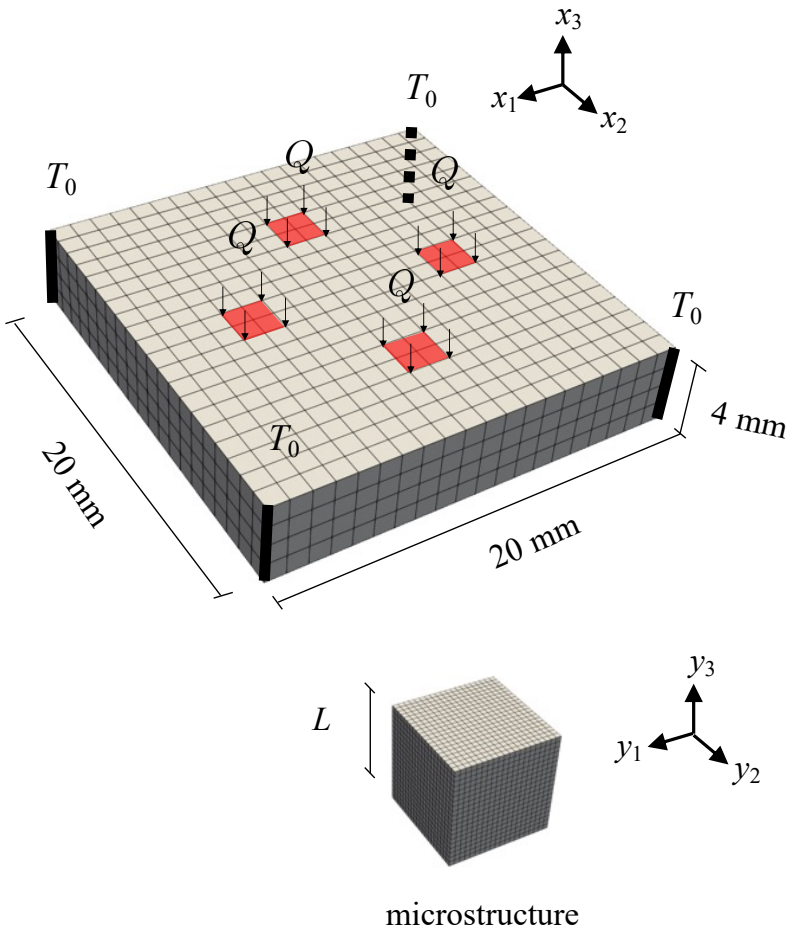

Figure 4.10: A plate-like macrostructure under four heat fluxes and its microstructure

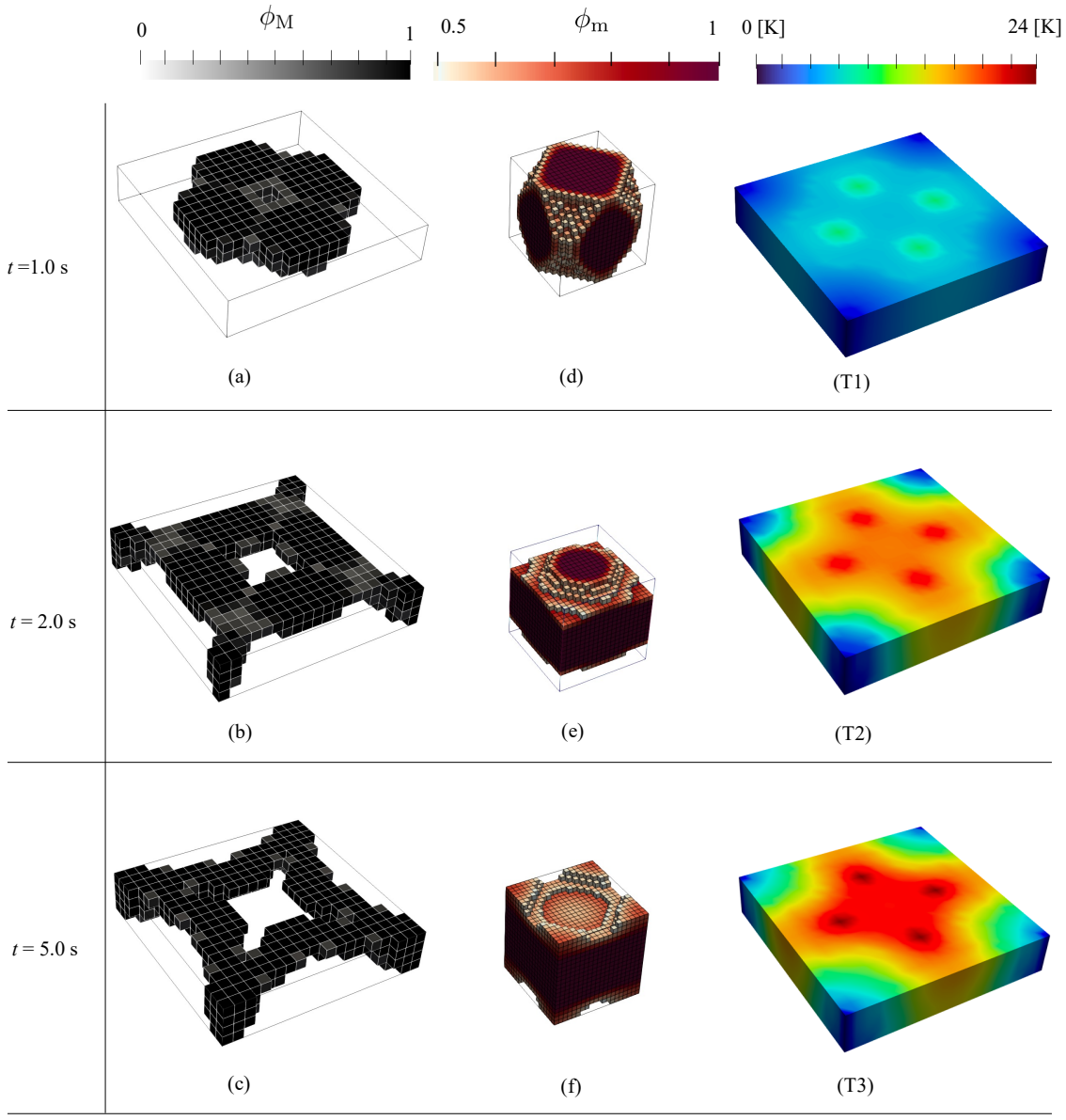

Figure 4.11: The optimization results at each target time of plate-like macrostructures under four heat fluxes

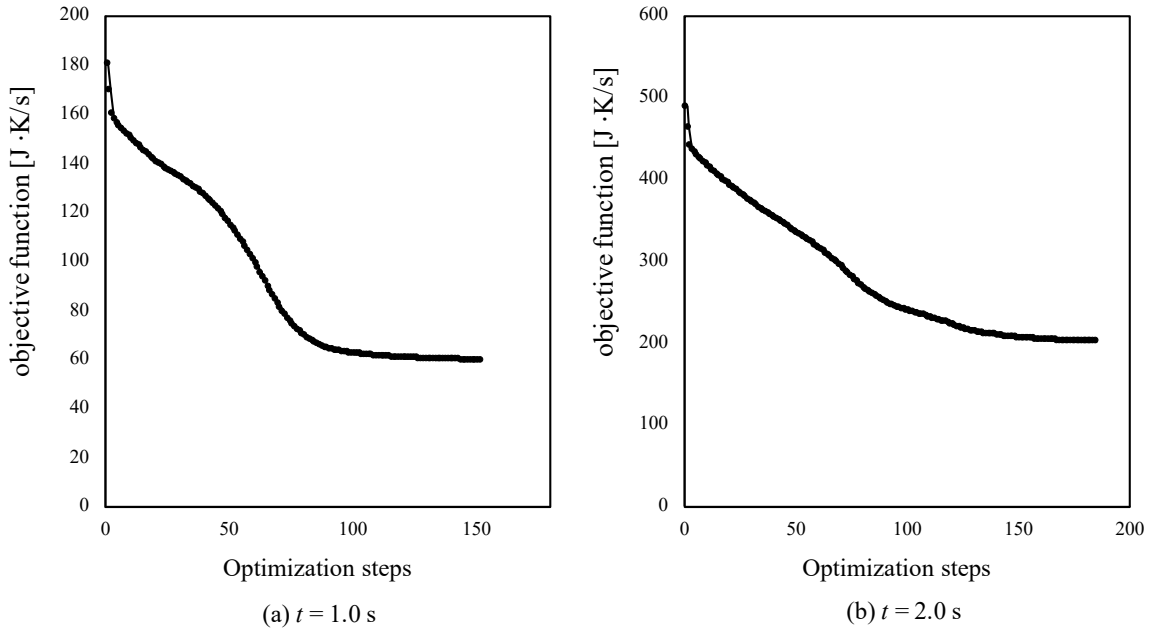

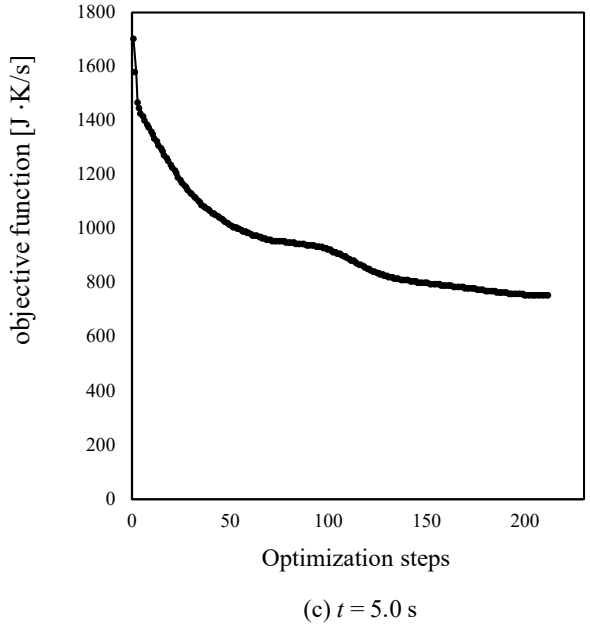

Figure 4.12: History of objective function values at different target times

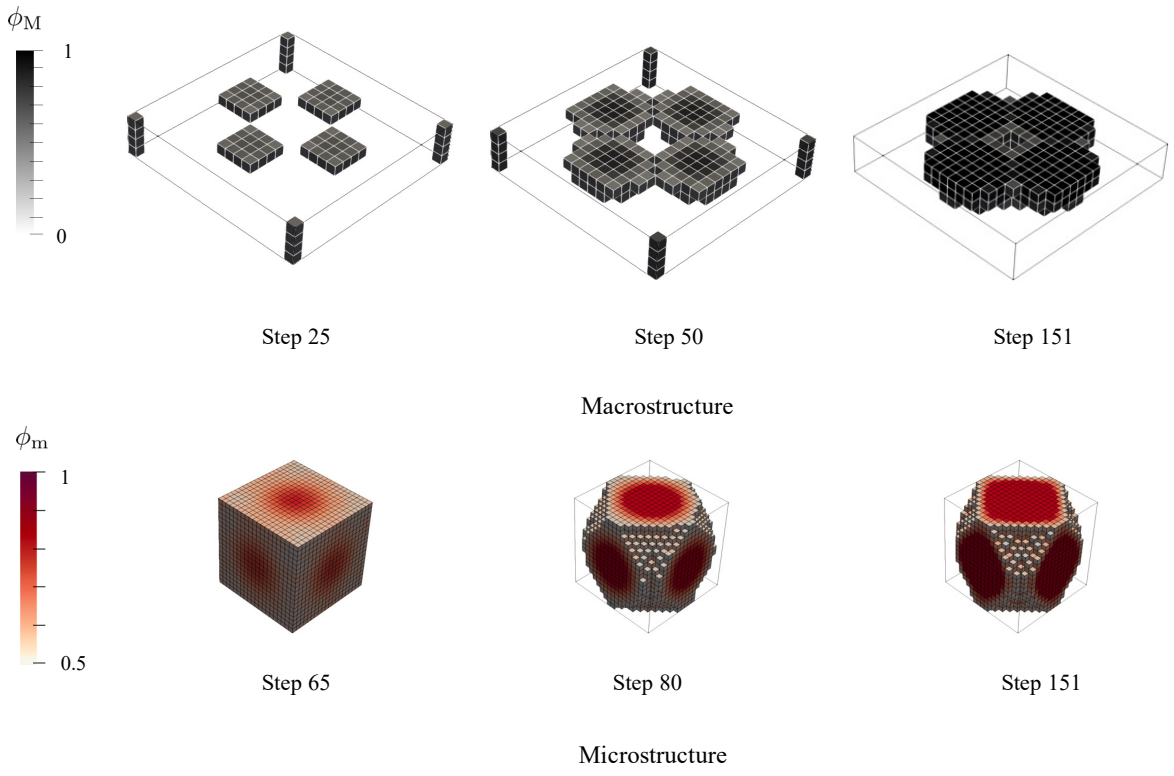

Figure 4.13: History of optimal topologies for macro-and microstructures at $t = 1.0$ s

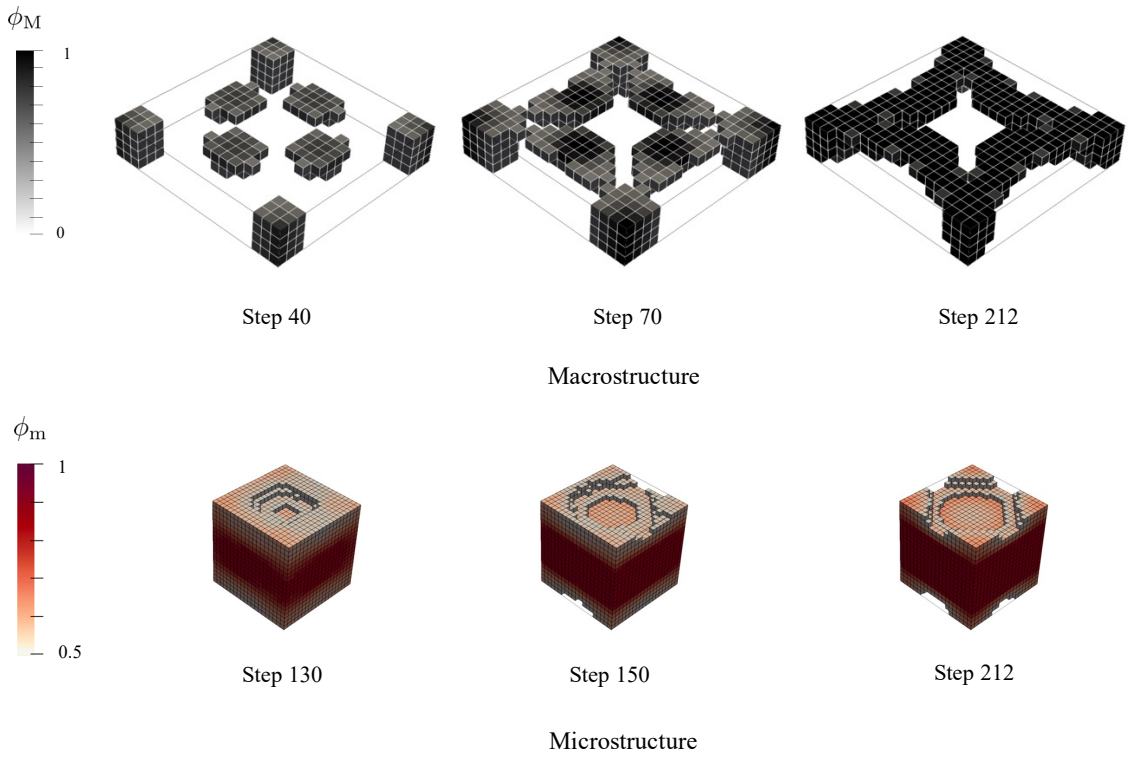

Figure 4.14: History of optimal topologies for macro-and microstructures at $t = 5.0$ s

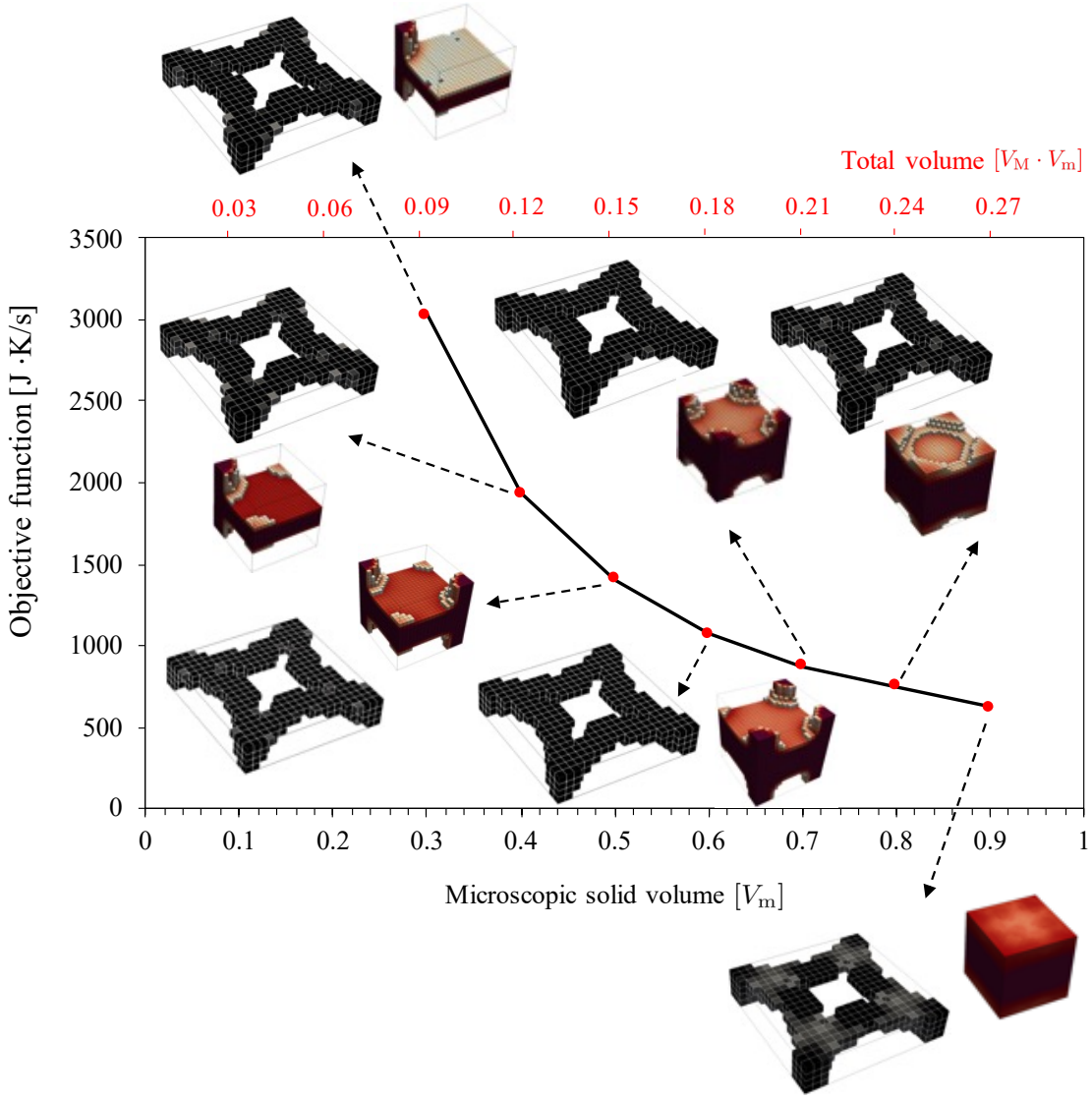

Figure 4.15: The investigation of microscopic volume constraint values of the solid phase

formed surrounding the location of applied heat fluxes (see Fig. 4.11(a)). Then, when the longer periods are applied at $t = 2.0$ s and 5.0 s, the solid phase is located expanding toward four edge corners with temperature constraints as shown in Fig. 4.11(b). This macrostructure pattern agrees with those presented in Xia et al. (2018) and Zhao et al. (2021): this implies the reliability of the proposed method. For the optimized microstructure, the solid phase is mainly formed along the principal axis (y_1, y_2, y_3) at unsteady-state $t = 1.0$ s, and distributes more in y_1y_2- plane when it approaches to steady-state at $t = 2.0$ s and 5.0 s. Besides, Fig. 4.12 confirms the robustness of the developed optimization framework, which

is smoothly converged to the optimal design. Also, Figs. 4.13 and 4.14 present the history of optimized topologies of optimal macro-and microstructures at $t = 1.0$ s and 5.0 s, respectively. It is also observed that the microstructure results show a similar trend to the previous example. This evidence verifies the high reproducibility of the transient effect of the proposed concurrent two-scale topology optimization. Note that the intermediate value of design variables is still remained in case of Figs. 4.11(c) and (f) due to the setting of volume constraint. Thus, to observe the influence of microscopic volume constraint, we conduct the optimization with the same conditions as Figs. 4.11(c) and (f), but vary the volume constraint values of the solid phase in the microstructure. Fig. 4.15 shows that the objective function value decreases as the volume constraint of the solid phase increases. This is reasonable because the total volume of design material ($V_{\mathrm{M}} \cdot V_{\mathrm{m}}$) increases to maximize heat dissipative performance. However, it can be seen that the volume constraint of the solid phase should be carefully set in order to avoid struggling with intermediate value in the optimized structures.

4.3 Summary

Two-scale porous structures were simultaneously designed by the proposed design framework based on concurrent topology optimization for micro- and macrostructures subject to transient heat transfer analysis. The homogenization method incorporated with the size-dependent term was employed to govern the two-scale heat conduction in the porous material. The density-based interpolation scheme, SIMP approach, and the design-dependent linear function were adopted to transit the design topology to the optimum smoothly. The analytical sensitivity formulation was derived using the adjoint variable method and then implemented in the gradient-based optimization problem.

The two numerical examples of the plate-like macrostructure under the single and multiple heat fluxes were conducted, respectively. The results showed that the time condition was the remarkable parameter that affected the optimized macro- and microstructures as the transient effect. Then, the size-dependent effect was investigated through the first example. It was revealed that the smaller microstructure size can reduce the objective function: this implies that the cumulative heat effect that remains in the structure decreases. Furthermore, the small size was also the cause of an asymmetrical topology of the microstructure. This is because the surface area was included in the optimization indirectly through the size-dependent term. Next, the influence of the microscopic volume constraint was presented in the second example. A large number of intermediate values remain if the inappropriate microscopic volume constraint is employed.

Chapter 5

Conclusion

In this dissertation, multi-scale topology optimization for three-dimensional transient heat transfer analysis including the size-dependent effect of microstructure from the porous material has been successfully developed. The robust and attractive performance of the proposed scheme was demonstrated through the design of various macro-and microstructures under transient heat analysis. The contents and achievements were listed as follows:

- In Chapter 1, the research background, motivation, and literature review were presented to highlight the contribution of the current work. It can be seen that topology optimization under transient heat transfer analysis has not been extensively explored, especially for the multi-scale analysis, which is widely applied for a porous material.

- In Chapter 2, the two-scale transient heat transfer analysis for porous solid material was summarized and presented in a general framework that can be applied for high and low thermal conductivity materials. Homogenization and the highlight of this work, the size-dependent term, were introduced to deal with the heterogeneous material and reflex the characteristic of porous material.

- In Chapter 3, we developed a two-scale topology optimization framework for designing the optimal microstructure in a porous material based on the analysis model introduced in Chapter 2. The optimization model, which can consider the surface area directly from microstructure topology as the size-dependent term, was introduced to enhance the heat transfer performance. A well-known material interpolation referred to as the SIMP approach and the linear function were adopted for smoothly interpolating intermediate material properties. The minimal transient heat compliance was established as an objective function, and it was used to derive transient sensitivity formulation by a coupled-adjoint

variable method. The results show that the proposed topology optimization model performs better when considering the transient condition. Also, the size-dependent effect of the microstructure shows a robust feature, which can enhance the heat dissipation performance.

- In Chapter 4, we extended the design framework from Chapter 3 to be capable of the concurrent two-scale topology optimization in which both macro-and microstructures were simultaneously optimized under macroscopic transient heat conditions. Two design variables as the continuous function for both scales were introduced to obtain optimal structures smoothly. The optimization problems were established for macro-and microstructures, which were solved sequentially to monotonically converged to optimal design. The analytical sensitivity formulations for gradient-based optimization algorithms were derived with the same strategy in Chapter 3. As a result, the design results demonstrated powerful performance. Furthermore, the optimized macrostructures show good agreement with the benchmark from the existing works, while the optimized microstructure was a similar trend to the design results obtained from Chapter 3. Remarkably, the design results also emphasize the significance of transient and size-dependent effects on both macro and microstructures.

Consequently, the developed design framework has the attractive feature which can be used for designing macro-microstructures along with size-dependent effects. As can be seen from the result, it shows the advantages compared to the conventional design framework. According to positive features, topology optimization for multi-scale analysis considering the size-dependent effect of microstructure should be extended to design the structure under multidisciplinary physics such as thermal-fluid, thermal-mechanical-fluid, thermal-chemo-mechanical, etc.

Bibliography

[1] Al Ali M, Shimoda M (2022) Investigation of concurrent multiscale topology optimization for designing lightweight macrostructure with high thermal conductivity. Int J Therm Sci 179:107653

[2] Baloyo JM (2017) Open-cell porous metals for thermal management applications:fluid flow and heat transfer. Mater Sci Technol 33(3):265-276

[3] Bejan A, Dincer I, Lorente S, Miguel A, Reis H (2004) Porous and complex flow structures in modern technologies. Springer, New York

[4] Bendsøe MP, Kikuchi N (1988) Generating optimal topologies in structural design using a homogenization method. Comput Methods Appl Mech Eng 71(2):197-224

[5] Bensoussan A, Lions JL, Papanicolaou G (2011) Asymptotic analysis for periodic structures. American Mathematical Soc Vol. 374

[6] Bendsøe MP, Sigmund O (2003) Topology optimization:theory, methods, and applications. Springer, New York

[7] Bilen K, Gok S, Olcay AB, Solmus I (2017) Investigation of the effect of aluminum porous fins on heat transfer. Energy 138:1187-1198

[8] Bochev PB, Gunzburger MD, Shadid JN (2004) Stability of the SUPG finite element method for transient advection-diffusion problems. Comput Methods Appl Mech Eng 193:2301-2323

[9] Bruns TE (2007) Topology optimization of convection-dominated, steady-state heat transfer problems. Int J Heat Mass Transf 50(15-16):2859-2873

[10] Buehler M J, Bettig B, Parker GG (2004) Topology optimization of smart structures using a homogenization approach. J Intell Mater Syst Struct 15(8):655-667

[11] Cheng L, Liang X, Belski E, Wang X, Sietins JM, Ludwick S, To AC (2018) Natural frequency optimization of variable-density additive manufactured lattice structure:theory and experimental validation. J Manuf Sci Eng 140(10)

[12] Cheng L, Liu J, To AC (2018) Concurrent lattice infill with feature evolution optimization for additive manufactured heat conduction design. Struct Multidisc Optim 58(2):511-535

[13] Cheng, L, Bai, J, To AC (2019) Functionally graded lattice structure topology optimization for the design of additive manufactured components with stress constraints. Comput Methods Appl Mech Eng 344:334-359

[14] Clyne TW, Golosnoy IO, Tan JC, Markaki AE (2006) Porous materials for thermal management under extreme conditions. Philos Trans Royal Soc A 364(1838):125-146

[15] Das S, Sutradhar A (2020) Multi-physics topology optimization of functionally graded controllable porous structures: Application to heat dissipating problems. Mater Des 193:108775

[16] Dbouk T (2017) A review about the engineering design of optimal heat transfer systems using topology optimization. Appl Therm Eng 112:841-854

[17] Deng J, Yan J, Cheng G (2013) Multi-objective concurrent topology optimization of thermoelastic structures composed of homogeneous porous material. Struct Multidisc Optim 47(4):583-597

[18] Diaaz AR, Kikuchi N (1992) Solutions to shape and topology eigenvalue optimization problems using a homogenization method. Int J Numer Methods Eng 35(7):1487-1502

[19] Du Z, Zhou XY, Picelli R, Kim HA (2018) Connecting microstructures for multiscale topology optimization with connectivity index constraints. J Mech Design 140(11):111417

[20] Elkholy A, Kempers R (2020) Enhancement of pool boiling heat transfer using 3D-printed polymer fixtures. Exp Therm Fluid Sci 114:110056

[21] Fan Z, Yan J, Wallin M, Ristinmaa M, Niu B, Zhao G (2020) Multiscale eigenfrequency optimization of multimaterial lattice structures based on the asymptotic homogenization method. Struct Multidisc Optim 61(3):983-998

[22] Fawaz A, Hua Y, Le Corre S, Fan Y, Luo L (2022) Topology optimization of heat exchangers: A review. Energy:124053

[23] Feng S, Li F, Zhang F, Lu TJ (2018) Natural convection in metal foam heat sinks with open slots. Exp Therm Fluid Sci 91:354-362

[24] Forooghi P, Abkar M, Saffar-Avval M (2011) Steady and unsteady heat transfer in a channel partially filled with porous media under thermal non-equilibrium condition. Transp Porous Media 86:177-198

[25] Fugmann H, Di Lauro P, Sawant A, Schnabel L (2018) Development of Heat Transfer Surface Area Enhancements: A Test Facility for New Heat Exchanger Designs. Energies 11(5):1332

[26] Gan N, Wang Q (2021) Topology optimization design related to size effect using the modified couple stress theory. Eng Optim:1-19

[27] Gan N, Wang Q (2022) Topology optimization design for buckling analysis related to the size effect. Math Mech Solids 27(7):1301-1318

[28] Gao T, Zhang WH, Zhu JH, Xu YJ, Bassir DH (2008) Topology optimization of heat conduction problem involving design-dependent heat load effect. Finite Elem Anal Des 44(14):805-813

[29] Gao J, Luo Z, Xia L, Gao L (2019) Concurrent topology optimization of multiscale composite structures in Matlab. Struct Multidisc Optim 60(6):2621-2651

[30] Gersborg-Hansen A, Bendsøe MP, Sigmund O (2006) Topology optimization of heat conduction problems using the finite volume method. Struct Multidisc Optim 31(4):251-259

[31] Gresho PM, Lee RL (1981) Don't suppress the wiggles-they're telling you something!. Comput Fluids 9(2):223-253

[32] Hassani B, Hinton E (1998) A review of homogenization and topology optimization I–homogenization theory for media with periodic structure. Comput Struct 69(6):707-717

[33] Hostos AJC, Fachinotti VD, Peralta I,Tourn BA (2019) Computational design of metadevices for heat flux manipulation considering the transient regime. Numer Heat Transf; A: Appl 76(8):648-663

[34] Hyun J, Kim HA (2021) Level-set topology optimization for effective control of transient conductive heat response using eigenvalue. Int J Heat Mass Transf 176:121374

[35] Ilinca F, Hetu JF (2002) Galerkin gradient least-squares formulations for transient conduction heat transfer. Comput Methods Appl Mech Eng 191(27-28):3073-3097

[36] Jia J, Cheng W, Long K (2018) Two-scale topology optimization of macrostructure and porous microstructure composed of multiphase materials with distinct Poisson's ratios. Lat Am J Solids Struct 15 (11)

[37] Jiaqiang E, Luo B, Han D, Chen J, Liao G, Zhang F, Ding J (2022) A comprehensive review on performance improvement of micro energy mechanical system: Heat transfer, micro combustion and energy conversion. Energy 239:122509

[38] Jung T, Lee J, Nomura T, Dede EM (2022) Inverse design of three-dimensional fiber reinforced composites with spatially-varying fiber size and orientation using multiscale topology optimization. Compos Struct 279:114768

[39] Kawamoto A, Matsumori T, Yamasaki S, Nomura T, Kondoh T, Nishiwaki S (2011) Heaviside projection-based topology optimization by a PDE-filtered scalar function. Struct Multidisc Optim 44(1):19-24

[40] Kato J, Ogawa S, Ichibangase T, Takaki T (2018a) Multi-phase field topology optimization of polycrystalline microstructure for maximizing heat conductivity. Struct Multidisc Optim 57(5):1937-1954

[41] Kato J, Yachi D, Kyoya T, Terada K, (2018b) Micro - macro concurrent topology optimization for nonlinear solids with a decoupling multiscale analysis, Int J Numer Meth Eng 113(8):1189-1213

[42] Kaviany M (1999) Principles of heat transfer in porous media. Springer, New York

[43] Khatir S, Boutchicha D, Le Thanh C, Tran-Ngoc H, Nguyen T N, Abdel-Wahab M (2020) Improved ANN technique combined with Jaya algorithm for crack identification in plates using XIGA and experimental analysis. Theor Appl Fract Mech 107:102554

[44] Khatir S, Tiachacht S, Le Thanh C, Ghandourah E, Mirjalili S, Abdel-Wahab M (2021) An improved Artificial Neural Network using Arithmetic Optimization Algorithm for damage assessment in FGM composite plates. Compos Struct 273:114287

[45] Lafdi K, Mesalhy O, Shaikh S (2007) Experimental study on the influence of foam porosity and pore size on the melting of phase change materials. J Appl Phys 102(8):083549

[46] Lange F, Hein C, Li G, Emmelmann C (2018) Numerical optimization of active heat sinks considering restrictions of selective laser melting. In COMSOL Conference 2018

[47] Lee SC, Cunnington GR (2000) Conduction and radiation heat transfer in high-porosity fiber thermal insulation. J Thermophys Heat Trans 14(2):121-136

[48] Li B, Hong J, Liu G, Ge L (2018) On identifying optimal heat conduction topologies from heat transfer paths analysis. Int Commun Heat Mass Transf 90:93-102

[49] Li Q, Steven GP, Xie YM, Querin OM (2004) Evolutionary topology optimization for temperature reduction of heat conducting fields. Int J Heat Mass Transf 47(23):5071-5083

[50] Li Y, Gong L, Xu M, Joshi Y (2021) A review of thermo-hydraulic performance of metal foam and its application as heat sinks for electronics cooling. J Electron Packag 143(3)

[51] Li L, Khandelwal K (2015) Topology optimization of structures with length-scale effects using elasticity with microstructure theory. Comput Struct 157:165-177

[52] Liu S, Su W (2010) Topology optimization of couple-stress material structures. Struct Multidisc Optim 40(1):319-327

[53] Liu C, Du Z, Zhang W, Zhang X, Mei Y, Guo X (2021) Design of optimized architected structures with exact size and connectivity via an enhanced multidomain topology optimization strategy. Comput Mech 67(3):743-762

[54] Liu J, Gaynor AT, Chen S, Kang Z, Suresh K, Takezawa A, Li L, Kato J, Tang J, Wang CC, Cheng L (2018) Current and future trends in topology optimization for additive manufacturing. Struct Multidisc Optim 57(6):2457-2483

[55] Liu Q, Chan R, Huang X (2016) Concurrent topology optimization of macrostructures and material microstructures for natural frequency. Mater Des 106:380-390

[56] Liu P, Kang Z, Luo Y (2020) Two-scale concurrent topology optimization of lattice structures with connectable microstructures. Addit. Manuf. 36:101427

[57] Lohan DJ, Dede EM, Allison JT (2017) Topology optimization for heat conduction using generative design algorithms. Struct Multidisc Optim 55(3):1063-1077

[58] Long K, Wang X, Gu X (2018) Multi-material topology optimization for the transient heat conduction problem using a sequential quadratic programming algorithm. Eng Optim 50(12):2091-2107

[59] Manuel MC, Lin PT (2017) Design explorations of heat conductive pathways. Int J Heat Mass Transf 104:835-851

[60] Michna GJ, Browne EA, Peles Y, Jensen MK (2011) The effect of area ratio on microjet array heat transfer. Int J Heat Mass Transf 54(9-10):1782-1790

[61] Mohamad AA (2003) Heat transfer enhancements in heat exchangers fitted with porous media Part I: constant wall temperature. Int J Therm Sci 42(4):385-395

[62] Nakshatrala PB, Tortorelli DA, Nakshatrala K (2013) Nonlinear structural design using multiscale topology optimization. Part I: Static formulation. Comput Methods Appl Mech Eng 261:167-176

[63] Ouyang XL, Vafai K, Jiang, PX (2013) Analysis of thermally developing flow in porous media under local thermal non-equilibrium conditions. Int J Heat Mass Transf 67:768-775

[64] Ozguc S, Pan L, Weibel JA (2021) Topology optimization of microchannel heat sinks using a homogenization approach. Int J Heat Mass Transf 169:120896

[65] Pizzolato A, Sharma A, Maute K, Sciacovelli A, Verda V (2017) Design of effective fins for fast PCM melting and solidification in shell-and-tube latent heat thermal energy storage through topology optimization. Appl Energy 208:210-227

[66] Pizzolato A, Sharma A, Maute K, Sciacovelli A, Verda V (2019) Multi-scale topology optimization of multi-material structures with controllable geometric complexity-Applications to heat transfer problems. Comput Methods Appl Mech Eng 357:112552

[67] Rashidi S, Kashefi M H, Kim KC, Samimi-Abianeh O (2019) Potentials of porous materials for energy management in heat exchangers–A comprehensive review. Appl. Energy 243:206-232

[68] Seo M, Park H, Min S (2020) Heat flux manipulation by using a single-variable formulated multi-scale topology optimization method. Int Commun Heat Mass Transf 118:104873

[69] Sertkaya AA, Altinisik K, Dincer K. (2012). Experimental investigation of thermal performance of aluminum finned heat exchangers and open-cell aluminum foam heat exchangers. Exp Therm Fluid Sci 36:86-92

[70] Sigmund O, Petersson, J (1998) Numerical instabilities in topology optimization: a survey on procedures dealing with checkerboards, mesh-dependencies and local minima. Struct Optim 16(1):68-75

[71] Singh C, Tathgir RG, Muralidhar K (2009) Energy storage in fluid saturated porous media subjected to oscillatory flow. Heat Mass Transf 45(4):427-441

[72] Sivapuram R, Dunning PD, Kim HA (2016) Simultaneous material and structural optimization by multiscale topology optimization. Struct Multidisc Optim 54(5):1267-1281

[73] Sopian K, Daud WRW, Othman MY, Yatim B (1999) Thermal performance of the double-pass solar collector with and without porous media. Renew Energy18(4):557-564

[74] Subramaniam V, Dbouk T, Harion JL (2018) Topology optimization of conductive heat transfer devices: an experimental investigation. Appl Therm Eng 131: 390-411

[75] Suzuki K, Kikuchi N (1991) A homogenization method for shape and topology optimization. Comput Methods Appl Mech Eng 93(3):291-318

[76] Svanberg K (1987) The method of moving asymptotes - a new method for structural optimization. Int J Numer Meth Eng 24(2):359-373

[77] Takarazawa S, Ushijima K, Fleischhauer R, Kato J, Terada K, Cantwell WJ, Kaliske M, Kagaya S, Hasumoto S (2022) Heat-transfer and pressure drop characteristics of micro-lattice materials fabricated by selective laser metal melting technology. Heat Mass Transf 58(1):125-141

[78] Takezawa A, Kobashi M (2017) Design methodology for porous composites with tunable thermal expansion produced by multi-material topology optimization and additive manufacturing. Compos B Eng 13:21-29

[79] Terada K, Hori M, Kyoya T, Kikuchi, N (2000) Simulation of the multi-scale convergence in computational homogenization approaches. Int J Solids Struct 37(16):2285-2311

[80] Terada K, Kurumatani M, Ushida T, Kikuchi N (2010) A method of two-scale thermo-mechanical analysis for porous solids with micro-scale heat transfer. Comput Mech 46(2):269-285

[81] Tortorelli DA, Haber RB (1989) First-order design sensitivities for transient conduction problems by an adjoint method. Int J Numer Methods Eng 28(4):733-752

[82] Tran-Ngoc H, Khatir S, Ho-Khac H, De Roeck G, Bui-Tien T, Abdel-Wahab M (2021) Efficient Artificial neural networks based on a hybrid metaheuristic optimization algorithm for damage detection in laminated composite structures. Compos Struct 262:113339

[83] Woodside W, Messmer JH (1961) Thermal conductivity of porous media. I. Unconsolidated sands. J Appl Phys 32(9):1688-1699

[84] Wang F, Lazarov BS, Sigmund O (2011) On projection methods, convergence and robust formulations in topology optimization. Struct Multidisc Optim 43(6):767-784

[85] Wang C, Zhu JH, Zhang WH, Li SY, Kong J (2018) Concurrent topology optimization design of structures and non-uniform parameterized lattice microstructures. Struct Multidisc Optim 58(1):35-50

[86] Wang L, Zhao X, Liu D (2022) Size-controlled cross-scale robust topology optimization based on adaptive subinterval dimension-wise method considering interval uncertainties. Eng Comput:1-18

[87] Wu S, Zhang Y, Liu S (2019) Topology optimization for minimizing the maximum temperature of transient heat conduction structure. Struct Multidisc Optim 60(1):69-82

[88] Wu S, Zhang Y, Liu S (2021a) Transient thermal dissipation efficiency based method for topology optimization of transient heat conduction structures. Int J Heat Mass Transf 170:121004

[89] Wu J, Sigmund O, Groen JP (2021b) Topology optimization of multi-scale structures: a review. Struct Multidisc Optim 63:1455-1480

[90] Xia L, Breitkopf P (2017) Recent advances on topology optimization of multiscale nonlinear structures. Arch Comput Methods Eng 24(2):227-249

[91] Xia Q, Shi T, Xia L (2018) Topology optimization for heat conduction by combining level set method and BESO method. Int J Heat Mass Transf 127:200-209

[92] Yan X, Huang X, Zha Y, Xie YM (2014) Concurrent topology optimization of structures and their composite microstructures. Comput Struct 133:103-110

[93] Yoon GH, Dede EM, Nomura T, Schmalenberg, P (2020) Topology optimization of time-transient heat conduction for thermo-optic silicon modulators. Int J Heat Mass Transf 157:119862

[94] Yoon GH (2022) Transient sensitivity analysis and topology optimization of particle suspended in transient laminar fluid. Comput Methods Appl Mech Eng 393:114696

[95] Zhang W, Sun S (2006) Scale-related topology optimization of cellular materials and structures. Int J Numer Methods Eng 68(9):993-1011

[96] Zhang Y, Liu, S (2008) Design of conducting paths based on topology optimization. Heat Mass Transf 44(10):1217-1227

[97] Zhao Q, Zhang H, Wang F, Zhang T, Li X (2021) Topology optimization of non-Fourier heat conduction problems considering global thermal dissipation energy minimization. Struct Multidisc Optim (64):1385-1399

[98] Zhou S, Li Q (2008) Computational design of multi-phase microstructural materials for extremal conductivity. Comput Mater Sci 43(3):549-564

[99] Zhuang C, Xiong Z (2014) A global heat compliance measure based topology optimization for the transient heat conduction problem. Numer Heat Transfer, Part B 65(5):445-471

[100] Zhuang C, Xiong Z (2015) Temperature-constrained topology optimization of transient heat conduction problems. Numer Heat Transfer, Part B 68(4):366-385

[101] Zhuang C, Xiong Z, Ding H (2007) A level set method for topology optimization of heat conduction problem under multiple load cases. Comput Methods Appl Mech Eng 196(4-6):1074-1084

[102] Zhuang C, Xiong Z, Ding H (2020) Topology optimization of transient nonlinear heat conduction using an adaptive parameterized level-set method. Eng Optim:1-23